ABSTRACT

Title of Document:	Cytoskeletal Mechanics and Mobility in the Axons of Sensory Neurons
	Joshua Michael Chetta, Ph.D. 2011
Directed By:	Assistant Professor Sameer Shah, Fischell Department of Bioengineering

The axon is a long specialized signaling projection of neurons, whose cytoskeleton is composed of networks of microtubules and actin filaments. The dynamic nature of these networks and the action of their associated motor and cross-linking proteins drives axonal growth. Understanding the mechanisms that control these processes is vitally important to neuroregenerative medicine and in this dissertation, evidence will be presented to support a model of interconnectivity between actin and microtubules in the axons of rat sensory neurons. First, the movement of GFP-actin was evaluated during unimpeded axonal outgrowth and a novel transport mechanism was discovered. Most other cargoes in the axon are actively moved by kinesin and dynein motor proteins along stationary microtubules, or are moved along actin filaments by myosin motor proteins. Actin, however, appears to be collected into short-lived bundles that are either actively carried as cargoes along other actin filaments, or are moved as

passive cargoes on short mobile microtubules. Additionally, in response to an applied stretch, the axon does not behave as a uniform visco-elastic solid but rather exhibits local heterogeneity, both in the instantaneous response to stretch and in the remodeling which follows. After stretch, heterogeneity was observed in both the realized strain and long term reorganization along the length of the axon suggesting local variation in the distribution and connectivity of the cytoskeleton. This supports a model of stretch response in which sliding filaments dynamically break and reform connections within and between the actin and microtubule networks. Taken together, these two studies provide evidence for the mechanical and functional connectivity between actin and microtubules in the axonal cytoskeleton and suggest a far more important role for actin in the development of the peripheral nervous system. Moreover this provides a biological framework for the exploration of future regenerative therapies.

Cytoskeletal Mechanics and Mobility in the Axons of Sensory Neurons

By

Joshua Michael Chetta

Dissertation submitted to the Faculty of the Graduate School of the
University of Maryland, College Park, in partial fulfillment
of the requirements for the degree of
Doctor of Philosophy
2011

Advisory Committee:
Assistant Professor Sameer Shah, Chair
Professor Helim Aranda-Espinoza
Professor Adam Hsieh
Professor Sergei Sukharev
Assistant Professor Arpita Upadhyaya

Dedication

Wham

Acknowledgements

This work would not have been possible without the help and support of my advisor, Dr. Sameer Shah. I cannot thank him enough for his patience. He gave me the freedom to define the scope of this research and has always expressed unwavering belief in me and my abilities as a scientist and a thinker. For me, that confidence has been essential to this achievement. This work would also not have been possible without the help of the outstandingly bright and creative undergraduate students with whom I have been fortunate enough to work: Cecilia Kye, Kelliann Wachrathit and Bao Nguyen. I would also like to thank the current and former members of Dr. Shah's lab: James Love, Gunja Dave, Tom Chuang, Sebila Kratovac, and Christina Kyrtsos. I would like to thank the members of my committee: Dr. Helim Aranda-Espinoza, Dr. Adam Hsieh, Dr. Sergei Sukharev, and Dr. Arpita Upadhyaya as well as Dr. Jens Herberholz who served on my proposal committee. Finally, I would like to thank my family and friends for their help, support and love during the last 29 years.

Table of Contents

List of Tables

List of Figures

proportion of anterograde and retrograde directed tracks compared to Lifeact-TagGFP2 which had a larger number of paused tracks. (B) Similarly, both GFP-actin and Lifeact-TagGFP2 had a larger number of new tracks begin during the imaging time. (C) Tracks were divided into runs, and GFP-actin and Lifeact-TagGFP2 exhibited a larger number of runs on average than maxGFP during the imaging time. Additionally, maxGFP expressing axons had a disproportionately large number of stationary runs compared to Lifeact-TagGFP2 and GFP-actin. (D) The stationary nature of maxGFP is even more striking when viewed in terms of time. The total time for all runs was summed and the fraction of that time spent in each of the three phases of movement calculated. MaxGFP particles spent a disproportionate amount of the total time paused. (E) The average net displacement for each time lapse was defined as the average displacement of each track in a time lapse. GFP-actin expressing axons exhibited a slight anterograde average net displacement, while Lifeact-TagGFP2 exhibited an average net displacement of zero. The average net displacement calculation for maxGFP expressing axons was dominated by the fast moving retrograde particles, contributing to the large retrograde average net displacement. When these particles were not included in the calculations, the average net displacement decreased to zero. (F, G) The average velocity, the duration in seconds and the distance traveled by a particle during a run were all calculated for Lifeact-TagGFP2 (F) and maxGFP (G) expressing cells. A Kolmogorov Smirnov test was used to determine statistically significant changes in these axons compared to GFP-actin expressing axons. Confidence values for the change are indicated by the number of arrows, and the direction of the arrow indicates whether it increased or decreased. An open circle indicates no statistically significant change.

Figure 3: Actin density identity. Fluorescence recovery after photobleach (FRAP) was used to determine the contribution of monomeric soluble actin to the movement of actin in the axon. (A) A 30 μm long region of the axon (indicated in green) was bleached and observed for recovery of fluorescence. A number of 10x10 pixel regions of interest (ROIs) inside the axon were used to quantify the changing fluorescent signal over time. These are indicated by the colored brackets flanking the axon. (B) Fluorescence recovery was not uniform within the bleached region, though; the purple and the yellow regions recovered fluorescence much faster than the surrounding axon. (C) In another experiment, high magnification and a high frame rate were used to capture the birth and death of an actin density (arrow) in detail. Selected frames from the time-lapse are shown. Scale bar: 5 μm. (D) A kymograph of the region outlined by the black box in C between 45 and 120 seconds, illustrating the change in width of the particle track (black arrow) over time, suggesting that these particles are mediated by condensation and dissolution of bundles of actin filaments. (E) Line traces of the fluorescent intensity over time in the colored 10x10 pixel ROIs shown in C. Note the increased fluorescent intensity corresponding to the particle birth (red trace). (F) Lack of ribosomal co-localization with actin. Axons were stained for RPL-4 and labeled with phalloidin as well. “x” indicates phalloidin labeled puncta. The arrows indicate RPL-4 positive puncta. Scale bar: 10 μm.

Figure 4: Figure 4: Effect of microtubule associated drugs on the mobility of actin densities in the axon. (A-C) After exposure to either nocodazole (B) or EHNA (C), cells were fixed and stained for actin and tubulin to determine the effect of drug treatment on the axonal cytoskeleton. Note the disruption of microtubule continuity after exposure to nocodazole (Scale bars 10 μm). (D) Nocodazole exposure increased average net displacement in the axon, while EHNA treatment initially induced a strong retrograde average net displacement, which then diminished over time. (E-G) Both nocodazole and EHNA affected the overall number of tracks over time as well as the direction of those tracks. (H) Nocodazole increased the dynamic nature of actin mobility in the axon, increasing the duration and distance traveled for all three phases of motion. The effect on paused particles was particularly striking as they moved a significant distance in the anterograde direction, thus contributing to the observed anterograde average net displacement. (I) EHNA treatment initially increased the velocity with which retrograde particles moved, which contributed to the net retrograde average net displacement. However, over time, EHNA decreased the overall dynamics of actin mobility. Particle tracks lasted longer, but moved more slowly.

Figure 5: Effect of actin associated drugs on the mobility of actin densities in the axon. (A-E) After exposure to either latrunculin (B) or BDM (D), cells were fixed and stained for actin and tubulin to determine the effect of drug treatment on the axonal cytoskeleton. C is a frame from a time lapse movie of a GFP-actin axon treated with jasplakinolide. Note that latrunculin affected the distribution of actin, but also seemed to affect microtubule integrity as well; some microtubules buckled, and protruded through the axonal cortex (arrow). (E) Latrunculin and jasplakinolide had a significant effect on the distribution of actin, within the growth cone. BDM treatment induced a less severe disruption. Scale bars 10 μm, all panels. (F) Latrunculin exposure increased retrograde average net displacement in the axon initially, but this effect gradually decreased over time. BDM treatment induced a strong anterograde average net displacement which increased over time. (G-I) Both latrunculin and BDM affected the number of tracks over time as well as the direction of those tracks. Note that BDM preferentially reduced the number of retrograde and paused tracks. (J) Latrunculin increased actin particle dynamics, increasing the duration for all three phases of motion and increasing the distance traveled by moving particles. The retrograde velocity was most significant, though, in affecting the retrograde average net displacement. (K) BDM reduced the speed with which particles moved and increased the pause duration. It induced an increasingly strong anterograde average net displacement by reducing the number of paused and retrograde directed tracks.

Figure 6: Filopodia and actin densities. A portion of the mobile actin densities gave rise to filopodia that protruded from the side of the axon. However, not all of the observed filopodia were populated with fluorescent actin. Lifetime, maximum length achieved and the angle of protrusion out of the axon were all measured in the DIC channel and compared between those filopodia which were populated with fluorescent actin (DIC w/F) and for those that weren't (DIC w/o F). Additionally, these same parameters were measured using only the fluorescent channel (Fluorescent). (A) There was no

possible pairs of mitochondria was plotted as a function of the initial length of the segment between the pairs for the unstretched (I) and stretched (J) axons shown in A-F.

Figure 3: Strain heterogeneity is increased at small length scales. Data from all instantaneous deflections were pooled and analyzed. (A) Strain in a segment between two mitochondria was plotted as a function of the initial length of the segment (cf. Fig. 3I-J). The average value for strain in stretched axons approaches the expected strain of 10% (0.1 on the Y-axis – heavy black line). (B) Variability of strains in (A) was calculated using O'Brien's method. (c) Variability for five μm bin sizes as quantified by O'Brien's method is greatest between 5 and 10 μm, and decreases dramatically for regions longer than 20 μm in length. While this same trend is noted in unstretched axons, the magnitude of the variability is much smaller. Using a two-tailed Student's T-test, variability in stretched axons was shown to be statistically different from variability in unstretched axons for the bins incorporating data from regions of the axons of initial length, 5-10, 10-15 and 15-20 μm as indicated by *, ‡,and ● respectively. Not enough data was collected from regions of unstretched axons smaller than 5 μm to test for statistically significant differences from stretched axons.

Figure 4: Regions within stretched axons exhibit continued remodeling following stretch. (A, B) Sample images of unstretched (A) and stretched (B) axons in which mitochondrial position was monitored over 22 minutes. (B) shows the axon before stretch. (C-E) Kymographs were created by tracing along the axon at each time and extracting the position of mitochondria from pixel intensities. For reference, the positions of mitochondria in the axon shown in B before stretch are shown in C. Kymographs for mitochondrial movement in unstretched (D) and stretched (E) axons from (A, B). Strain in regions of unstretched (F) and stretched (G) axons, calculated from the positions of consecutive pairs of mitochondria. A particularly active region of the stretched axons (arrow) exhibited very large strains that were achieved very quickly and then stabilized (G). As with other axons, this region of large strain was between closely spaced mitochondria, while strains in the rest of the axon and in unstretched axons were all of smaller magnitude (G, F).

Figure 5: Remodeling in axons following stretch is length- and time-dependent. As with axons analyzed for instantaneous strain, all pairs of mitochondria in axons were used to calculate strain during the 22 minute experimental period. (A) Average calculated strain for all mitochondrial pairs over all time points. Strain in a segment of an axon between two mitochondria was plotted as a function of the initial length of that segment. Positive and negative strains represent net elongation or contraction of the axon, respectively. (B) Variability in this data, quantified using O'Brien's Method. (C-F) To evaluate the change in strain over time, strain was calculated using the change in position of mitochondria between 1 and 4 minutes of imaging (beginning), between 9 and13 minutes (middle) and between 18 and 22 minutes (end). The average strain magnitude and variability are plotted for unstretched (C, D) and stretched (E, F) axons. A two-tailed student's T-test was used to confirm that strain magnitude and variability decreased by a statistically significant amount in stretched axons over the course of the experiment.

velocity, duration, and distance traveled by a particle were measured in axons expressing one of the three fluorescent constructs. Because the distributions were broad and non-normal, a Kolmogorov Smirnov test was used to test for significant differences between groups. The results of this analysis are summarized in the tables of figure 2.

Figure S2: Cumulative histograms showing the distribution of transport parameters for particles in axons treated with either nocodazole or EHNA. The velocity, duration, and distance traveled by a particle were measured in axons expressing GFP-actin. Statistically significant differences are summarized in the table of Figure 4.

Figure S3: Cumulative histograms showing the distribution of transport parameters for particles in axons treated with either Latrunculin or BDM. The velocity, duration, and distance traveled by a particle were measured in axons expressing GFP-actin. Statistically significant differences are summarized in the table of Figure 4.

Figure S4: Changes in particle direction over time. (A) All of the drugs decreased the total number of tracks over time, although latrunculin showed a slight recovery during the last 12-20 minutes of imaging. (B) Run direction as a percentage of the total number of runs in a given time-lapse calculated for the middle time phase (6-12 minutes of drug exposure). (C-F) Track direction as a percentage of the total number of tracks for each of the three temporal phases of drug exposure.

Chapter 1: General Introduction

The axon as a unique model system for studying transport and mechanics

The neuron is responsible for transmitting electrochemical signals in the body. To accomplish this, peripheral neurons develop long specialized signaling projections called axons that grow out from the cell body, advance through the activity of a highly motile growth cone and establish a synaptic connection with other neurons or a muscle fiber. The energetic and structural costs of axonal outgrowth and maintenance are huge and the axonal cytoskeleton plays multiple roles meeting these demands throughout the life of the cell. First, microtubules and actin filaments form polymer scaffolds inside the axon that serve as tracks along which a variety of metabolic, structural and signaling cargoes are carried by motor proteins. Additionally, peripheral nerves are exposed to applied forces during movement and growth of the organism. Mechanical interactions between the cytoskeletal networks and their associated cross-linking and force generating proteins help axons within the nerves accommodate these loads.

Previous work on individual cells has shown that axonal outgrowth and morphology are affected by an applied stretch, but the mechanisms underlying these effects are not known. In this work we have explored the hypothesis that both growth and mechanical adaptation in the axon are processes that depend on the structural integrity, passive connectivity and

activity of force generating components of the cytoskeleton. In effect, the axon's ability to exert force and mechanically adapt to its changing environment depends on the adaptability of its supporting cytoskeleton. In the first part of this dissertation, our discovery of a novel transport mechanism for actin during axonal outgrowth will be discussed. This mechanism suggests that actin and microtubules exhibit greater interconnectivity in the axon than previously thought, and that this connectivity is extremely dynamic. In the second half of this work, we will present a discussion of the response of the axonal cytoskeleton to an applied tensile load. We found that in response to stretch, the axon behaves as a series of independent linked regions, suggesting heterogeneity in the integrity and connectivity of the underlying cytoskeleton. Furthermore, after stretch the cytoskeleton changes over time, a result that reinforces the idea that connections within and between the actin and microtubule polymer networks are dynamic. Taken together, our findings represent a major step forward in neuronal cell biology and provide a foundation for future research on axonal biomechanics and peripheral nerve regeneration.

Background: Cytoskeletal Organization in the Axon

The axonal cytoskeleton is a dynamic array of filamentous polymers connected by various static and force generating cross linking elements (Figure 1). Microtubules run through the core of the axon, with neurofilaments filling space between them and actin arrayed in a cortex lying directly

underneath the plasma membrane (Gallo et al. 2002; Heidemann et al. 1985; Lee and Cleveland 1996; Peters and Vaughn 1967; Yamada et al. 1971). Crosslinking elements include both rigid connectors and dynamic motor proteins. Microtubules in the axon exhibit a characteristic polarity, with their plus-ends, or rapidly polymerizing ends, extending away from the cell body(Baas and Black 1990). Along with their structural role in the axon, controlled and facilitated by microtubule associated proteins (MAPs), microtubules serve as the tracks along which the motor proteins kinesin and dynein walk (Schnapp and Reese 1989; Vale et al. 1985a). The majority of kinesins move towards the plus end of the microtubule, while dynein and a few minus-end oriented kinesins move towards the minus end. Filamentous actin (F-actin) is a polymer rod composed of monomers of globular (G-actin) subunits (Chang and Goldman 1973). Actin filaments are also complimented by a multitude of actin binding proteins (ABPs) which regulate functions important to the structural integrity of the actin cortex (Koenig and Letourneau 2009). Additionally, multiple types of myosin motor proteins move along actin(Unsicker K 1978).

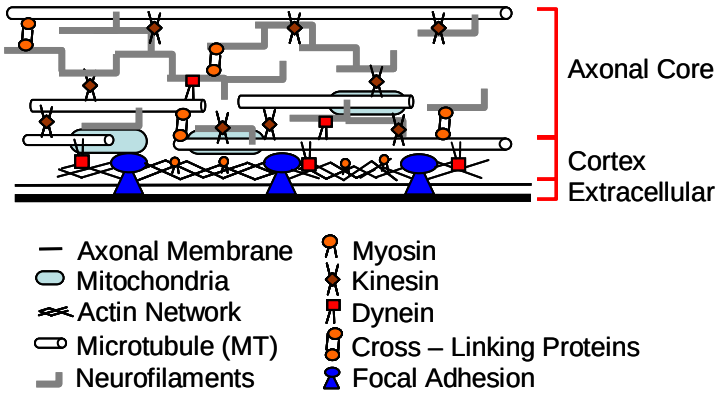

Figure1: Cytoskeletal organization in the axon. The axonal cytoskeleton is composed of arrays of polymer filaments. Actin lies in a cortex underneath the membrane, while microtubules and neurofilaments occupy the core of the axon. A number of accessory proteins are associated with both actin and microtubules, including the motor proteins, kinesin, dynein, and myosin as well as other proteins which form more stable cross links.

Background: Axonal Transport

The history of axonal transport is covered in depth in the review by Alvarez (Alvarez et al. 2000), but, briefly, the transport of material from the cell body down the axon was proposed as a mechanism in 1948 (Weiss and Hiscoe 1948) and a number of subsequent radio-labeling experiments resulted in the parsing of axonal transport into one fast component, which moved at upwards of 40mm/day and two slow components, Slow component b (SCb) which moves between 2-7mm/day and slow component a (SCa) which moves between 0.1 and 1mm/day. (Black and Lasek 1980; Droz B 1963; Hoffman and Lasek 1975; Willard et al. 1974). Microtubules were known to be important early on, (Banks et al. 1971a; Banks et al. 1971b), but it wasn't until the 1980's that kinesin and dynein were identified as the motors responsible for anterograde and retrograde movement of vesicles along the axon, respectively. (Schnapp and Reese 1989; Vale et al. 1985a; Vale et al. 1985b) Because of their integral role in axonal outgrowth and the axon's structural integrity, the mechanism underlying the transport of cytoskeletal proteins has been an area of intense debate and active study. Neurofilaments and microtubules are transported in the slow component but, unexpectedly, don't move at a consistently slow rate. Rather these filaments are moved by

kinesins and dynein at the same instantaneous rate as fast cargoes but their motion is less processive; it is punctuated by pauses and reversals. (Allen et al. 1982; Brady et al. 1982; Wang and Brown 2002). Less well understood is the mechanism by which actin is transported in the axon. Early radiolabeling experiments indicated that actin is transported at rates associated with slow component-b (Black and Lasek 1979; Willard et al. 1974), though other studies report that some actin may also travel with tubulin in both slow component-a and -b (McQuarrie et al. 1986; Tashiro and Komiya 1989). However, the initial possibility of a role for acto-myosin activity in the transport of SCb components has recently been rejected in favor of a microtubule based mechanism (Roy et al. 2000; Roy et al. 2007; Roy et al. 2008).

Biochemical and radiolabeling experiments from squid giant axon and chick sciatic nerve suggest that much of transported actin is soluble (Mills et al. 1996; Morris and Lasek 1982; Morris and Lasek 1984) but the role of monomers, oligomers, or short actin filaments to the soluble fraction is still unknown. However, there is frequent exchange between the filamentous fraction and these smaller units along the axon and within the growth cone (Okabe and Hirokawa 1992; Takeda et al. 1994). Additionally, recent work has demonstrated that actin is more mobile in the axon than originally thought (Gallo and Letourneau 2000). Actin is a key component of axonal filopodia, protrusions of which extend and retract and which may ultimately represent precursors to branches (Ketschek and Gallo 2010; Spillane et al. 2011). In addition, actin has also been observed to move as a wave in the neurites of

cultured hippocampal neurons (Flynn et al. 2009; Ruthel and Banker 1998; Ruthel and Banker 1999).

Background: Mechanical Loading and Growth

Peripheral nerves undergo tensile loading, or stretch, within a physiological range during growth and voluntary or imposed joint extension and flexion (Topp and Boyd 2006). Nerves are lengthened even more dramatically during orthopedic or regenerative surgery, including limb-lengthening procedures(Murray et al. 1993). Animal models of chronic nerve lengthening suggest that a threshold of strains and strain rates determine whether stretch is injurious or ameliorative, based on the structure and electrical conduction capabilities of the affected nerve (Eggli et al. 1999; Shi and Pryor 2002; Shi and Whitebone 2006; Shibukawa and Shirai 2001). However, the mechanisms underlying this empirically-determined threshold remain to be determined. At the cell level, axons, situated between the adherent cell body and extending growth cone are also thought to be under tension (Bray 1979; Lambert de Rouvroit and Goffinet 2001). As is true for many biological cells of the musculo-skeletal system, (Smith and Gilligan 1996; Vandenburgh et al. 1991) neurons also exhibit a morphological response to mechanical loading. Under a “towed growth” loading regimen, micromanipulator controlled glass needles have been used to apply and measure tensile forces on axons by pulling on the growth cone. These studies have revealed that axonal growth rate increases linearly with an

applied load, and that tension is important throughout neurite development (Heidemann et al. 1995). Related studies also showed that tension applied to the cell margin can induce neurite formation (Chada et al. 1997) and specify axonal fate(Lamoureux et al. 2002). A recent extension of towed growth, termed stretch growth (Pfister et al. 2004) has been used to create tracts of multiple axons that are up to 5 cm in length, towards a strategy for spinal cord regeneration(Iwata et al. 2006; Pfister et al. 2006b). Collectively, these studies establish that neurons both produce and respond to tensile forces.

Significance for Regenerative Medicine

A major goal of neuroregenerative medicine is the replacement of axonal function lost due to disease or traumatic injury. Although autologous nerve transplantation after injury can achieve this reasonably well, the procedure may require multiple surgeries and is only suitable for bridging short lesions in the peripheral nervous system (Deumens et al.). Much of the current research is focused on producing new materials that take advantage of extracellular signaling molecules to facilitate regeneration (Schmidt and Leach 2003). Particularly in light of the numerous effects of mechanical loading on axonal physiology and growth (see previous section: *Mechanical Loading and Growth*), a complimentary research perspective is to study the fundamental biological systems underlying the ways in which an axon interacts mechanically with its extracellular environment to modulate its internal structure during growth.

In many ways, this work was motivated by previous reports which enumerated the empirically determined thresholds and effects of mechanical loading. Our research extends those studies to provide a more complete understanding of dynamic cytoskeletal connectivity during growth and provides a biological mechanism for how the axon accommodates an applied tensile load in terms of the magnitude of cytoskeletal reorganization and the time course over which those changes take place. This more complete knowledge of axonal biology will facilitate the development of more comprehensive therapeutic interventions towards the goal of peripheral nerve regeneration.

Organization and Summary of Dissertation

This work examines the role of cytoskeletal dynamics in the axon during actin transport and in modulating the axon's response to an applied tensile load. The research in this dissertation is divided into three chapters (chapters 2-4). In chapter 2, a novel image processing algorithm is discussed which facilitates the analysis of axonal transport in highly mobile axons. In chapter 3, this algorithm is used to analyze the movement of actin in the axon during growth and in chapter 4, the response of an axon to an applied tensile load is examined.

Chapter2:

Kymograph analysis offers a simple and effective tool for use in analyzing axonal transport. A kymograph is a graphical representation of

motion along a one dimensional path, where position along the path is one axis, and time is along the other (Ch 2. Fig. 1). Typically, kymographs are built by having a user trace the path of the axon in one frame of a time-lapse movie and extracting intensity profiles from subsequent frames along that path. This method cannot accommodate movies in which translation of the axon, or changes in axonal orientation or geometry, occur. Both are frequently observed in long-term movies of neurons, both in vitro and in vivo. To solve this problem and automate the creation of kymographs from these movies, we developed a two step algorithm which is discussed in the next chapter. The first step implemented a simple image registration algorithm that aligned axons based on identification of a reference point on the axon in each image. The second step used a Hough transformation (HT) to automatically detect the axonal contour in each frame. Intensity profiles along this contour were then used to construct a kymograph. This algorithm was able to build an accurate kymograph of mitochondrial and actin transport in dynamic cultured sensory neurons, which were not amenable to previously used analytical methods.

Chapter 3:

This algorithm was then used to analyze the transport of GFP-actin in cultured sensory neurons, as discussed in chapter 3. GFP-actin expressing axons exhibited GFP labeled puncta that appeared and disappeared during the course of a time lapse and moved bidirectional with frequent pauses. Phalloidin staining as well as transfection with the actin labeling protein

Lifeact-TagGFP2 confirmed that these puncta were composed of filamentous actin. Additionally, the existence of these densities appeared to be controlled by bundling and dissociation of actin filaments rather than by de novo synthesis or polymerization. Most importantly, the overall dynamics of these particles exhibited a net anterograde displacement with rates of transport similar to those reported previously for the movement of slow component cargoes. To determine the mechanism by which these particles moved, pharmacological agents were used to perturb various components of the cytoskeletal network. Through rigorous quantification of changes in the transport parameters after exposure to these drugs, a model was developed in which actin transport is mediated by both actin and microtubule dependent processes. Most other transport in the axon occurs by kinesin and dynein motors carrying cargoes along stationary microtubules but our evidence suggests that actin is moved partially as a passive cargo attached to moving microtubules and is also moved by myosin, which is presumably walking along filaments in the actin cortex. This work represents a major step forward in understanding cytoskeletal mobility and slow component transport.

Chapter4:

In the fourth chapter, a novel cell stretching device was designed and implemented to study the response of the axonal cytoskeleton to a tensile load applied by stretching the culture substrate. Rat sensory neurons were seeded onto a flexible silicone sheets and imaged during substrate stretch. The positions of stationary mitochondria, docked to the axonal cytoskeleton,

were determined before and after 10% stretch, and used to calculate the resulting “instantaneous” strain in regions of the axon. There was dramatic heterogeneity in strain along the length of the stretched axons, particularly in regions shorter than 20 μm. The substrate was then held at 10% strain and the axons imaged for 20 minutes during “relaxation.” Both strain magnitude and variability were larger at small lengths in stretched axons during the initial phase of relaxation, but after 14 minutes, decreased to levels smaller than those seen in unstretched axons. Mitochondrial pairs in stretched axons showed uncoordinated movement with each other at all lengths, suggesting that cytoskeletal cohesion is reduced after stretch. Collectively, these data present the axonal cytoskeleton as a dynamic structure, which responds to stretch rapidly and locally. Although, globally the axon behaves as a viscoelastic continuum, below a characteristic length, it appears to behave as a series of independent linked elements, each with unique mechanical properties. This suggests a length scale within which cytoskeletal structural elements may be altered to modulate the biomechanical response of the axon.

Concluding Remarks and Summary

In this work we have studied the dynamic connectivity between actin and microtubules in the transport of actin and in the axon’s response to an applied tensile load. We addressed fundamental questions concerning neuronal force transmission and its effects on local regulation of cytoskeletal reorganization during growth and transport in the axon. We provide evidence

that the dynamic nature of the actin cytoskeleton itself and its connectivity with microtubules play a central role in both processes. This suggests a more prominent role for actin in the axon's engagement with its environment and answers questions about the role of the cytoskeleton in mediating the response of the axon to an applied stretch. Overall, this work provides a comprehensive framework for axonal physiology that has broad implications for the study of neuronal growth and peripheral nerve regeneration.

Chapter 2: A novel algorithm to generate kymographs from dynamic axons for the quantitative analysis of axonal transport[1]

Introduction

The axon is a long, narrow process that facilitates electrical signaling within the nervous system by transmitting action potentials. It also serves as a conduit within which a variety of structural, energetic, and signaling cargoes necessary for cellular function are actively transported by molecular motors along cytoskeletal tracks (Goldstein and Yang 2000; Hirokawa and Takemura 2004). Defects in axonal transport have been implicated in a variety of neurodegenerative diseases, including Alzheimer's Disease, Parkinson's Disease, and Amyotrophic Lateral Sclerosis (Chevalier-Larsen and Holzbaur 2006; Duncan and Goldstein 2006; Gunawardena and Goldstein 2004; Shah et al. 2009). The biological and clinical relevance of axonal transport has motivated an explosion of new approaches to its study. An increasingly common technique is the generation of fluorescence or bright field movies of labeled, motile cargoes in axons, both in vitro and in vivo (Cavalli et al. 2005; Mondal et al. 2011; Wang and Brown 2001; Waterman-Storer et al. 1997). Understanding changes in parameters describing the axonal transport of a particular cargo, such as directionality, velocity, or flux, can reveal details

[1] This has been previously published as: Chetta J, Shah SB. 2011. A novel algorithm to generate kymographs from dynamic axons for the quantitative analysis of axonal transport. Journal of Neuroscience Methods 199(2):230-240.

about cellular mechanisms underlying transport as well as pathways of transport dysfunction.

Performing such analysis requires the accurate identification of the coordinates of individual axonal cargoes of interest in each frame of a movie. These can then be consolidated into a set of cargo tracks, from which transport parameters can be extracted. Several image processing approaches have been implemented to generate high-resolution tracks. At the more computationally intensive edge of the spectrum, combinatorial optimization problems have been solved to generate 2-D trajectories of cargo movement (Cameron et al. 2006). In addition to computational expense, such methods also require a very high signal to noise ratio, which can be difficult to achieve in live cell fluorescence or bright field microscopy.

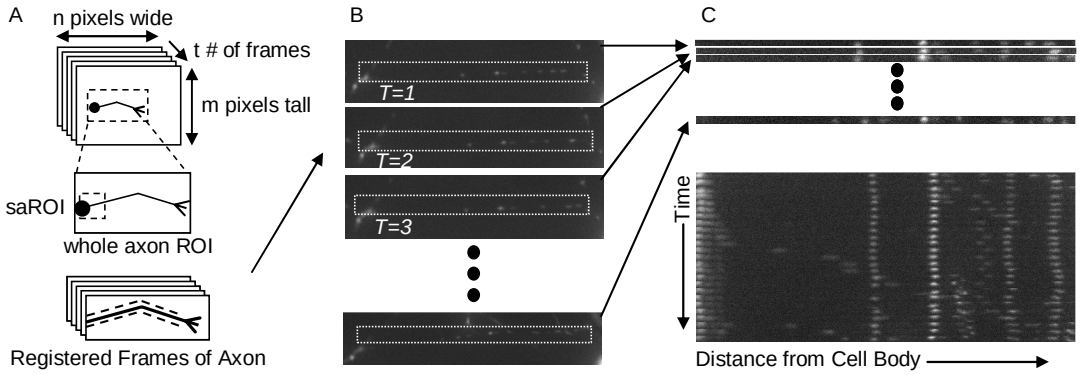

Figure1: Building a kymograph. (A) A time-lapse movie is an ordered series of still images, in which data is encoded by a pixel's intensity at specific x and y coordinates in an image at a particular time. A small region of interest (saROI) is used to align the images so that an axonal reference point is located in the same position in all frames. (B) The specific path of the axon is then defined and used to extract an intensity profile from each image. (C) When aligned vertically, these intensity profiles illustrate the position of particles within the axon as a function of time.

More simply, a kymograph provides a plot of the cargoes' positions along the one-dimensional path of the axon as a function of time. This graphical representation of cargo trajectories requires tracing a line upon the axon, from which intensity profiles are extracted and aligned at each time point (Bilsland et al. 2010; Haghnia et al. 2007; Miller and Sheetz 2004; Zhou et al. 2001). The kymograph can then be analyzed to determine the position of individual particles within the axon. To accurately interpret cargo trajectories, a fixed frame of reference for cargo motion must be identified, typically the axon itself. Additionally, the axon must be stationary for the duration of the movie, to provide a stable contour along which intensity profiles are generated. These requirements are often confounded by two major types of problems. The first, image drift, may result from temperature fluctuations or from instrumentation creep, and results in loss of focus and translation of the axon within the imaging field. The second problem is biological in nature; axons are dynamic, particularly over longer time periods, and frequently both their geometry and position change over time. Either of these two problems can result in unusable kymographs, due to movement of the axon away from, or even within (during elongation or retraction), the initially selected contour. More detrimental to interpretation may be trajectories in which more subtle artifacts of erroneous particle motion are introduced.

We have developed image processing algorithms that address artifacts and errors associated with axonal translation and altered axonal geometry.

First a stable reference point for cargo motion is established by bringing the beginning of the axon into registration in all frames of a time-lapse and then the axon is automatically identified in each frame. This method enables us to generate kymographs from movies of highly mobile axons not previously amenable to quantitative transport analysis. We have demonstrated the application of this method to track the movement of two fluorescently labeled cargoes with markedly different transport profiles, mitochondria and actin, in cultured mammalian sensory neurons. Ultimately, we anticipate that our methods will enable more rigorous quantitative characterization of transport within the context of axonal physiology, enhancing our understanding of mechanisms underlying transport function and dysfunction.

Methods and Materials:

Cell Culture and Microscopy

Time lapse (TL) movies of the axons of sensory neurons were created with paired Differential Interference Contrast (DIC) and wide field epi-fluorescent images. Dorsal root ganglia (DRG) were cultured in glass-bottom dishes (MatTek Corp. Ashland, MA) coated with laminin and labeled with Mitotracker Green (Invitrogen, Carlsbad, CA), per previous methods (Chetta et al.). For examining the movement of actin, prior to plating, DRG were electroporated with plasmid encoding GFP-actin (a generous gift from Dr. Helim Aranda-Espinoza) using protocols provided for Amaxa Nucleofector II. Images were captured using a Nikon TE-2000E inverted microscope fitted with a 40x 1.35NA PlanApo oil-immersion objective (0.16μm/pixel), every 45

seconds for mitochondria and every 5 seconds for actin. Exposure times were 3-5ms for the DIC channel and 100-200 ms for the fluorescent channel. The microscope stage was enclosed within an environmental chamber, which controlled temperature (37℃), humidity, and carbon dioxide (5%). Animal work has been approved by the IACUC at the University of Maryland.

Statistics

All statistical comparisons of significance were performed using a two tailed t-test assuming unequal variances.

Algorithms – Overview

Algorithms for image processing were developed using Matlab software (The Mathworks, Natick, MA) and were designed to process the time-lapse frames from a typical experiment (Figure 1), towards the generation of a kymograph, which could then be analyzed using any number of published manual, semi-automated, or automated methods.

The numbered steps of the algorithm summary (Figure 2) may be used to guide the remaining discussion of the algorithm. Those steps which required manual user inputs are outlined in a double box. Those which the computer performed automatically are outlined in a single box. Examples of image processing results for each step are provided in Figures 3-6. For clarity, we

occasionally refer to both the summary and examples in the description of the algorithm itself as well as the results.

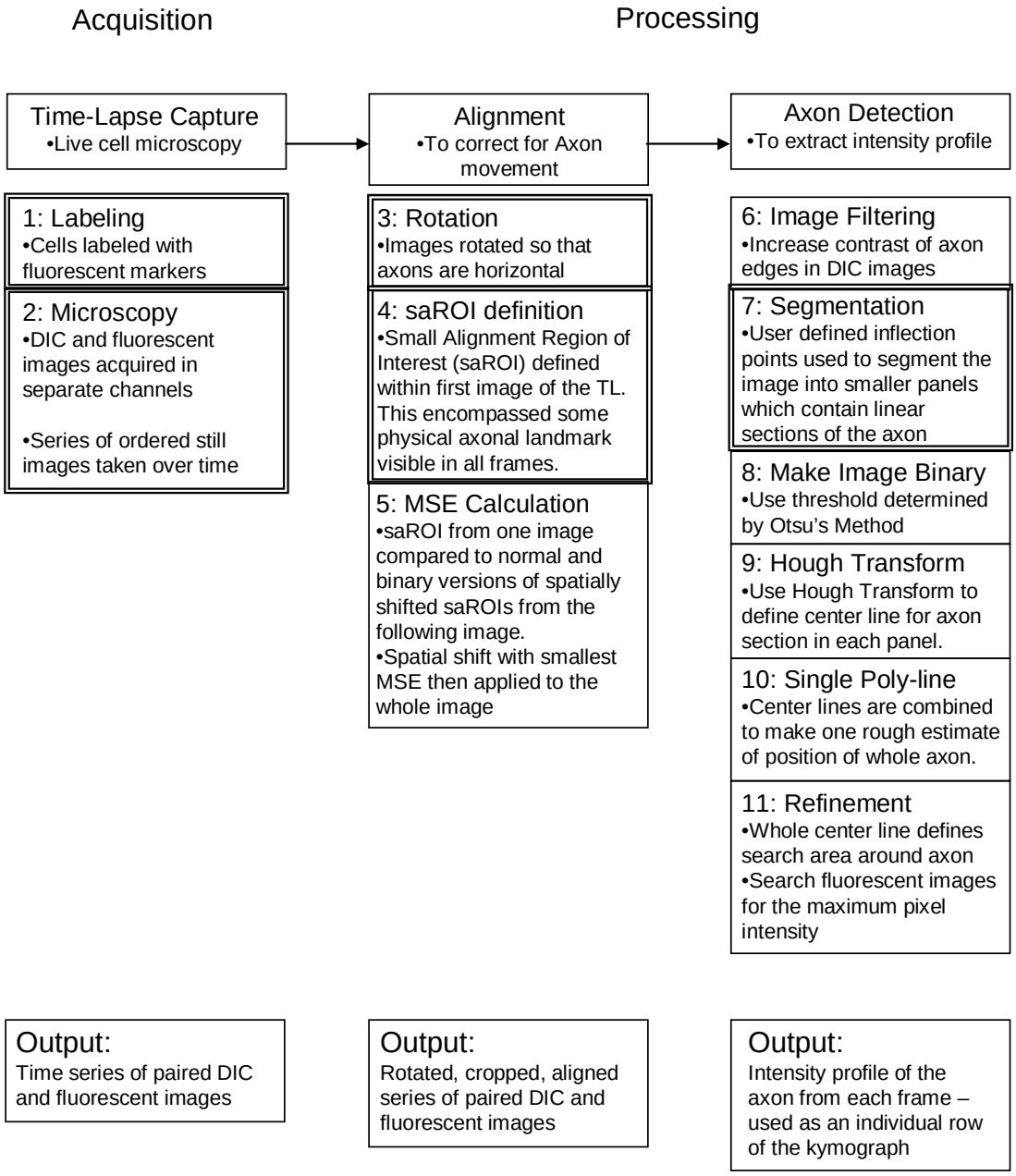

Figure 2: Flowchart of the image processing algorithm. Those steps which required manual user inputs are outlined in a double box. Those which the computer performed automatically are outlined in a single box. Refer to text for details.

The algorithm to build a kymograph consisted of two main steps. In the first step, a user designated a distinctive axonal landmark to serve as a stable reference point for cargo moving in the axon. This axonal reference point was some feature visible in all frames, such as a branch point or the transition point (i.e., change in concavity) between the cell body and axon. An automated registration algorithm processed the images so that this landmark was located at the same x and y coordinates in all frames of the time lapse. In the second step, the axonal contour was identified automatically in each frame, and an intensity profile along this contour was extracted from each image to populate one row of the final kymograph.

Fluorescence signals often vary within and across experiments, while DIC images have a higher and more consistent signal to noise ratio (SNR). Therefore, DIC images were used for axonal identification and alignment, and the results were mapped to the corresponding fluorescent image for each frame of the TL (Figure 2: Steps 1 and 2). This allowed for the generation of kymographs and the analysis of labeled cargoes that varied in fluorescent intensity and spatial distribution over time. This also enabled the creation of kymographs from the DIC movies themselves, which are useful for the analysis of dense cargoes visible in bright field and the analysis of axon outgrowth. To demonstrate the applicability of our methods to a range of cargo and transport profiles, kymographs will be presented for fluorescently labeled mitochondria and GFP-actin. Mitochondria are distributed relatively sparsely and exhibit punctate fluorescence (e.g., Figure 3), while GFP-actin is

a more prevalent and more diffuse label, interspersed with regions of brighter intensity (e.g., Figure 5).

Image Registration:

Overview:

Briefly, the image registration algorithm worked by comparing the location of a user designated axonal landmark in one frame of the TL to its location in the next frame. If the two positions were different, then the second frame was translated along the x and y axes until the locations of the landmarks were coincident. This was repeated with pairs of consecutive frames until all frames were processed. Because kymographs represent motion relative to some stationary point, it was necessary only to align this single reference point at the beginning of the axon. This greatly simplified the problem and reduced computation time. The comparisons and calculations were made using frames from the DIC channel, but the same translations were applied to the fluorescent channel(s) as well. The end result was a new series of images for each color channel.

Algorithm:

Before registration, each image in the time series was rotated so that the majority of the axon of interest was horizontal to within ± 15^{o} (Figure 2: Step 3). The rotation was determined manually by the user and was performed to align the central axis of the axon with the x-axis of the image.

The whole time series was rotated by the same amount. In the case of a curved axon, the maximum possible length of the axon was aligned with the x-axis. To reduce the size of the image and associated computations, the user was asked to manually select a rectangular region around the axon, which was cropped out of the first frame of the TL. The user was then shown that cropped image and asked to manually select a region within it that encompassed a distinctive morphological feature, such as a branch point, that would be visible in all frames of the TL. This region will be referred to as the small alignment ROI (saROI, ~70x70pixels) in this discussion (Figure 1; Figure 2: Step 4; Figure3A-B). Finally, the user was asked to manually select the "centroid" of the feature. These initial selection steps were performed manually, but the following comparisons were all performed automatically.

To determine how far out of register the axonal landmarks in consecutive images were, the saROI from the first image, called the reference image, was compared to shifted versions of the saROI collected from the next image in the series, called the target image (Figure 2: step 5; cf. (Zitová and Flusser 2003)). The saROI was spatially shifted within a 30 pixel x 30 pixel (roughly 5μm x 5μm) neighborhood in the target image, to create 900 candidate saROIs which were all the same size as the reference saROI. The mean squared error (MSE) between each candidate saROI and the reference saROI was calculated and the candidate saROI which yielded the smallest MSE was recorded. If two candidates resulted in a similar MSE, the one which was produced by the smaller spatial shift was chosen.

Additionally, to confirm that this was the correct spatial shift, two further calculations were made, based on the MSE between binary versions of the spatially shifted candidate saROIs and a binary version of the reference saROI. Threshold levels for the reference and the target saROIs were determined automatically using Otsu's method. For the first calculation, the reference threshold value was used to convert both the reference and target saROIs to binary images. In the second calculation, the reference threshold was applied to the reference saROI and the target threshold was applied to the target saROI. In both cases, the MSE between the binary saROIs was calculated and the associated spatial shift recorded. If they failed to produce a consensus for the correctly shifted saROI, the user was asked to manually pick the centroid in the target saROI and the images were aligned so that the two centroids coincided. Only a small fraction (<8%) of image pairs required that the user manually choose the centroid. Additionally, selecting a smaller alignment ROI (30x30 pixels) increased the number of times the user was asked to intervene.

Once the appropriate spatial shift was determined by the above methods, it was applied to the rectangular region around the whole axon in the large target image so that the axonal landmark from the saROIs appeared at the same coordinates in both whole axon cropped images. The target image then became the reference image for the next round of alignment, and was compared to the image following it, and the process was repeated until all frames had been aligned. This simple image registration algorithm takes

advantage of the fact that the differences between consecutive images are small; although there may be significant differences between the position of the axonal landmark in the first and last images of a time-lapse, these large changes take place gradually. Tracking these small translational changes between consecutive images is straightforward and robust.

Automated Axon Detection:

Overview:

The generalized Hough transform (HT), used to identify lines in an image, was originally developed by Duda and Hart (Duda and Hart 1972) and has since been extended to identify other geometric shapes (Ballard 1981). It is an elegant method that transforms the computationally intensive problem of finding co-linear points in the x-y plane into a different problem, of finding the intersection point of sinusoidal curves in the θ-p plane, where θ and p are parameters that describe the angle and normal distance of a line away from the origin, respectively. The registration algorithm created a new set of smaller images, in which the original time lapse frames had been rotated, aligned, and cropped (Figure 2: Steps 3-5). The second step of this algorithm used the HT to identify the position of linear portions of the axon in frames from the DIC channel in these new images. Axons often follow tortuous paths, which can be approximated by a series of connected straight line segments. To identify each line segment, each DIC frame of the time lapse was binarized and then divided into smaller panels which contained one roughly linear section of the axon. Each of these binary panels was then analyzed

using the HT to determine the position of the axon section within it. The resulting line segments from all the binary panels were then combined to create an approximate map of the position of the axon. This map was then applied to images from the fluorescent channel, and a search was implemented to find the exact position of the axon based on the maximum pixel intensity.

Algorithm

To divide the frames of the TL into smaller segments, the user was shown an overlay of the first and last images of the TL and asked to select points where the axon changed orientation at any point during the movie (inflection points). Inflection point selection was performed only once and the same points were used for all frames of a movie, so it was possible and acceptable for axon orientation to change in one part of the movie, but remain fixed for the remainder of the movie. This point selection was performed manually by the user; the following steps were all performed automatically. The possibility of error associated with these user-defined points and the associated size of the subdivided panels will be discussed in the results section.

Only binary images can be used as an input for the HT, so each frame of the DIC channel of the TL had to be processed to create a binary version in which the axon was emphasized. First, a high pass Sobel filter with the kernel [-1 -2 -1; 0 0 0; 1 2 1] was used to emphasize the axon's edges. This kernel is

“tuned” to recognize regions of high frequency change in the vertical direction (horizontal edges). Because it is directional, it was applied once from the top down and once from the bottom up (Figure 2: Step 6). The two resultant images were converted to binary images using thresholds determined by Otsu’s method and then combined into one composite image, with the edges of the axon in white against a black background (Figure 2: Step 7; Figure 4A, E; Figure 5C). The previously chosen inflection points were then used to divide the image into small panels (Figure 2: Step 8), which were processed with the HT (Figure 2: Step 9; Figure 4B-D, F-H; 5D-K). Two lines, one for each edge of an axon section, were determined and their end points averaged. These two resulting end points defined one consensus line through the middle of the axon section in each panel (Figure 4I, J). The center lines from neighboring panels were then joined end-to-end to make a continuous poly-line along the whole axon. If the end point of one center-line did not align with its neighbor’s end point, the average of the two was used (Figure 2: Step 10). This poly-line lay roughly along the center of the axon. To extract one row of the kymograph, this rough poly-line was applied to the time-matched frame(s) of the fluorescent channel(s). To refine the position of the axon, a window roughly twice the width of the axon was defined and, at each point along the axon’s length, searched for the maximum pixel intensity (this window was 15 pixels wide for images acquired at 40x; Figure 2: Step 11). These points were used to define one row of the final kymograph (seven pixels wide for images acquired at 40x). It is worth emphasizing that the HT

provided a rough starting point for the location of the axon in the form of a linear approximation but this last step resulted in a more accurate final contour that was not necessarily linear. The kymograph was then finalized by vertically aligning the extracted intensity profiles in the correct temporal order. Cargo tracks were then visually apparent, and ready for analysis through the use of any number of manual, semi-automated, and automated methods commercially available or in the literature.

Results:

I: Identification of potential pitfalls in traditional kymograph analysis

We first present an analysis of fluorescently labeled mitochondria moving within a cultured rat DRG axon. In this experiment, images were captured every 45 seconds for 20 minutes. This example was selected because it emphasizes the dynamic nature of cultured axons and the potential for resultant errors and misinterpretation. Figure 3A shows the same axon at three different time points. The geometry of the axon clearly changes over this time period (cf. slopes at T=9min vs. T=19min). In the standard construction of a kymograph, a single user defined path is drawn in the first image of a TL and used to extract intensity profiles from all subsequent frames of the movie (outlined by the dashed white lines in Figure 3A), under the assumption that the axon has remained stationary from frame to frame. Such a kymograph is shown in Figure 3D. Due to the changes in axon orientation, the last several rows are dark because the axon has drifted

outside of the initially traced path, but a more subtle problem occurs within the rows in which particles are visible. This standard construction assumes a stable reference point along the axon, but figure 3B and 3C demonstrate the mobility of reference point used here, a branch point. A non-automated approach to deal with a changing reference point, as well as changing axonal geometry requires the user to manually trace the axon in many or all of the frames throughout the time lapse, beginning each trace from the same reference point. These contours may then be assembled into a kymograph. Such analysis is shown in Figure 3E, using the branch point to the left of the figure as a reference point. This manual correction highlights the pitfalls of misalignment, as four seemingly mobile particles (arrowheads in figure 3D) are, in reality, stationary with respect to the branch point (arrowheads in figure 3E and 3F).

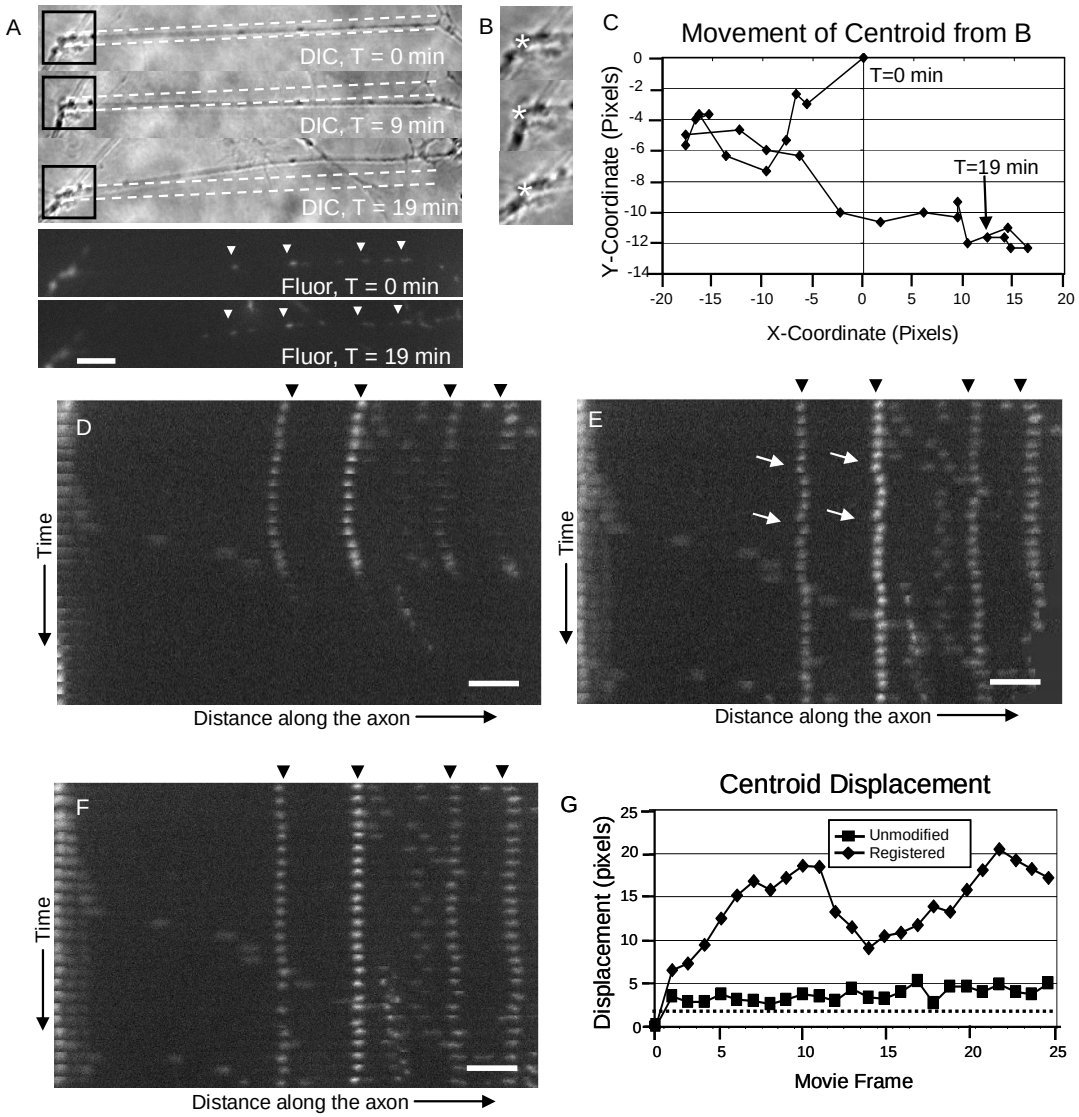

H	Mean±S.D. (Max)
Displacement of axonal landmarks in highly motile axons. (n = 6 axons)	Before alignment: 41.8±37.6 (158.2) After alignment: 7.8±5.1 (16.8)
Displacement of axonal landmarks in less motile axons. (n = 4 axons)	Before alignment: 2.8±1.9 (7.8) After alignment: 2.5±1.2 (6.1)

Figure 3: Automated method of kymograph generation outperforms manual methods. (A) DIC and fluorescent images of an axon labeled with Mitotracker green, taken from a time-lapse movie illustrating the change in geometry and orientation of the axon over time. The black boxes outline the saROI used for alignment purposes. The white dotted lines in the DIC images illustrate the position of the axon in the first frame of the TL and the movement of the axon outside of that path in subsequent frames. The white arrows in the fluorescent images indicate the four stationary mitochondria discussed in the text and indicated in D-F. (B) Larger view of the saROIs from A. The white stars indicate the "centroid" of the branch as chosen by

the user. (C) Movement of the centroid shown in B over time. (D) Kymograph built using one path traced in the first frame of the movie to extract intensity profiles from all subsequent frames. The black arrows indicate the four stationary labeled mitochondria discussed in the text. (E) Kymograph in which the path of the axon was manually traced in every frame of the movie. White arrows identify jumps in particle position between frames. (F) Kymograph built using our automated algorithm. (G) Graph showing the displacement from its original position of the centroid of the saROI from B before and after image registration. (H) The displacement of the centroid of an axonal landmark, such as the branch point shown in B, was analyzed in TL movies of 10 axons. While the gains were positive for both highly motile and more stationary axons, the algorithm made significant improvement for highly motile axons. Scale bar, 10μm in all panels.

While this manual approach resolves several artifacts associated with the standard method of building a kymograph, it is time consuming and also holds the potential for considerable user error highlighting the need for an automated method. A kymograph generated by this manual method was compared to a kymograph produced using our automated algorithms (Figure 3F), the construction of which will be detailed in sections II and III. It is apparent that the kymograph built using our algorithm is qualitatively similar to that built with manual input, especially compared to the kymograph shown in Figure 3D, but there are slight differences between them. The most notable is in the tracks of the four stationary particles (black arrows). Watching the raw movie, these particles appear to be stationary with respect to the axon and also appear to be stationary in these kymographs. However, in Figure 3E, there are noticeable regions of discontinuity in these tracks (white arrows) not seen in Figure 3F. The tracks in Figure 3E also display a very slight drift to the right. Comparing the last row to the first row in this figure, from left to right, the particles each move to the right by 7.7 pixels (1.3%),2.7 pixels (0.4%), 9.3 pixels (1.6%), and 8.7 pixels (1.5%) respectively, where the parenthetical

percentages refer to the shift relative to the total kymograph width (578 pixels). In Figure 3F, this drift is smaller; the difference in position between the first and the last frame for these tracks is reduced to 3 pixels right (0.5%), 3 pixels left (0.5%), 3 pixels right (0.5%) and 1 pixel left (0.2%), respectively, with a kymograph width of 662 pixels.

II: Alignment of Reference Points

The MSE based image registration algorithm aims to solve the alignment problem highlighted above by bringing an axonal landmark into register in all frames of the time lapse to serve as a reference point for particle motion. When manually tracing paths (cf. Figure 3E), the user draws a line segment drawn in each frame that begins at approximately the same point on the axon, based on visual cues. To accomplish this computationally, small regions of the axon (saROIs) were used to align the same reference point in all images. In fact, it was not necessary to align the whole axon, but only to bring one point of the axon into registration to serve as a reference point while building the kymograph. To determine the effectiveness of this alignment protocol, the position of the branch point shown in figure 3B was determined before and after alignment. A user was asked to manually select the position of its centroid in all 25 frames of the unmodified TL as well as in the series after alignment. Before alignment, the branch point moved significantly over time, translating up to ten pixels between frames, and over 35 pixels over the course of the movie (Figure 3B). It exhibited an average

displacement from its initial position of 13.8 pixels (Figure 3G: diamonds). After alignment, its average displacement decreased to 3.7 pixels (Figure 3G: squares), which is only slightly larger than the average user error when selecting the same point multiple times (2 pixels; Figure 3G - horizontal dotted line). In an additional five TL movies of extremely motile axons created under similar imaging conditions (1 frame per 45 seconds, between 25 and 41 total frames) we were able to reduce the average displacement significantly ($p<0.000001$, Table 3H) . In four additional time lapse movies, with frames captured every 5 seconds, the axonal displacement was much less dramatic and the gains from our alignment procedure still positive, but not significant.

III: Implementation of the Hough transform

The real power of this algorithm is the implementation of the HT to automatically identify axons that trace complex paths in the imaging field. Figures 4 and 5 demonstrate three characteristics of this transform that make it particularly effective. First, it is capable of accurately identifying linear structures in the image that are partially occluded or otherwise discontinuous. Additionally it retains a high degree of accuracy despite variation in user defined inputs as well as in images which contain noise. Between steps 5 and 6 in the algorithm described above, the user was asked to choose inflection points – places where the axon changed orientation or geometry, or where it would change orientation or geometry during the movie. These points were used to define boundaries to divide the image into segments which contained

linear portions of the axon. The same points were used to segment all frames of a TL so that for some frames, a longer linear section of the axon was split into smaller sections to accommodate future or past axonal geometries. As an example, in the TL described in Figure 3, the axon was pulled upward during the last few frames by another cell (Figure 3A, Figure 4A,E), creating three distinct linear sections in one previously linear axon (Figure 4B-D, F-H). The left-most panels of both frames are shown in detail to illustrate a few important points (Figure 4 I, J). First, both edges of the axon were identified by the HT and then averaged to specify the location of the center line (not shown in these figures). Second, although binary images may show incomplete or ambiguous axonal edges due to inconsistencies in illumination or debris in the imaging field, the HT is able to accurately identify these broken lines (white arrows).

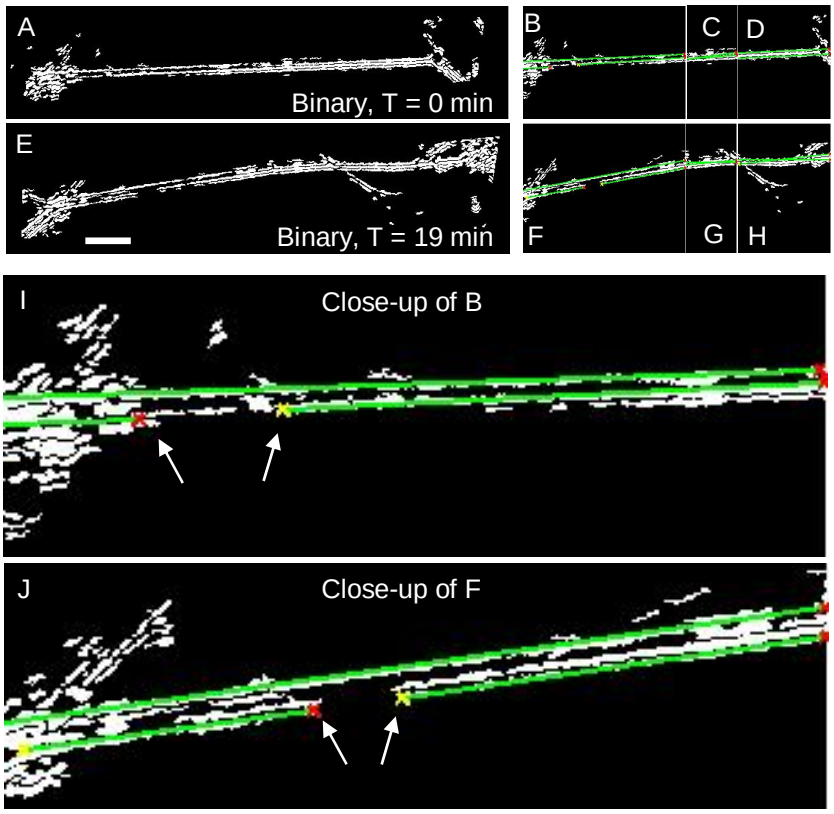

Figure 4: Hough transform. (A, E) Binary images created from the DIC images shown in Fig. 3A after image filtering and thresholding as discussed in the text. (B-J) Binary images with endpoints and lines determined by the HT overlaid on top. (B-D, F-H) Image segments analyzed with the Hough transform to identify the two edges of the axon. Although in A the axon is one straight segment, it was divided into smaller regions to accommodate the more complex geometry in E, a frame from later in the movie. (I, J) Detailed views of panels B and F illustrating the accuracy of the Hough transform, even in the case where the axon is incomplete (white arrows). Scale bar, 10μm.

In this algorithm, we have used the Hough transform to identify the axonal center-line in an image, but this only provides a rough approximation of the axon's position. This center-line is used to define a 15 pixel-wide window within which the actual position of the axon is refined through a search for the brightest pixel in the fluorescent channel. In the analyses discussed below, the HT was considered able to accurately identify the axon

if it was able to locate the position of the axon to within 7 pixels of its actual position.

To demonstrate the ability of the HT to accurately identify the axon in frames of a TL movie, a user was asked to manually select points along the axon. The x-coordinates chosen were used to divide the image into segments, which were then processed with the HT. Both the HT coordinates and whole axon center-lines they defined were compared to those chosen manually. Fourteen different axons were analyzed in this way (Figure 5A), and on average, the y-coordinate of an endpoint determined by the HT was different from one selected manually by 2.3 ±1.7 pixels. While the position of the endpoints for individual axonal segments is important, the more applicable metric for validation of this process is the position of the axonal center line determined by those endpoints. To test this, the center-lines defined by the manually selected endpoints were compared with those determined by the automatically generated HT endpoints. The residual, defined as the square root of the sum of the squares of the difference between the two lines, was calculated and normalized to the length of the axon. This error per unit length of the axon was found to be 2.2±0.5 pixels.

Additionally, The HT is relatively insensitive to noise in the image. Obtaining a clean image for all frames of a long time-lapse can be difficult and to demonstrate the ability of this algorithm to analyze noisy images, increasing amounts of Gaussian white noise was added to the original DIC images of these fourteen axons. The position of the endpoints and axonal

center-lines were then determined and compared to the manually selected positions. Gaussian white noise was added to each image in four increments, with the smallest amount of added noise having a standard deviation roughly one quarter of that of the image pixel intensity and the largest amount of noise having a standard deviation roughly equal to that of the image, such that the signal to noise ratio (SNR, defined here as the mean pixel intensity for the whole image divided by the standard deviation of the pixel intensity, $\mu_{image}/\sigma_{image}$), decreased from an average of 31.1 in all of the unaltered images to an average of 12.6 in those versions with the highest level of noise. The extent of image degradation is illustrated by the three panels in Figure 5B. These show an unaltered image, that same image with the least amount of noise added and, finally, with the largest amount of noise. It was found that for moderate levels of added noise, the HT performed well, and was able to accurately identify the position of the axon, but its accuracy diminished significantly ($p<0.06$ for residuals and $p<0.01$ for endpoints) at the two highest levels of additional noise (Figure 5C).

A

	Mean±S.D. (Min,Max)
Number of segments required for axon in image (n = 14 axons)	6.1±1.3 (4,9)
Size of image segments containing linear axon section, in pixels (n = 86 segments)	215±115 (58,640)

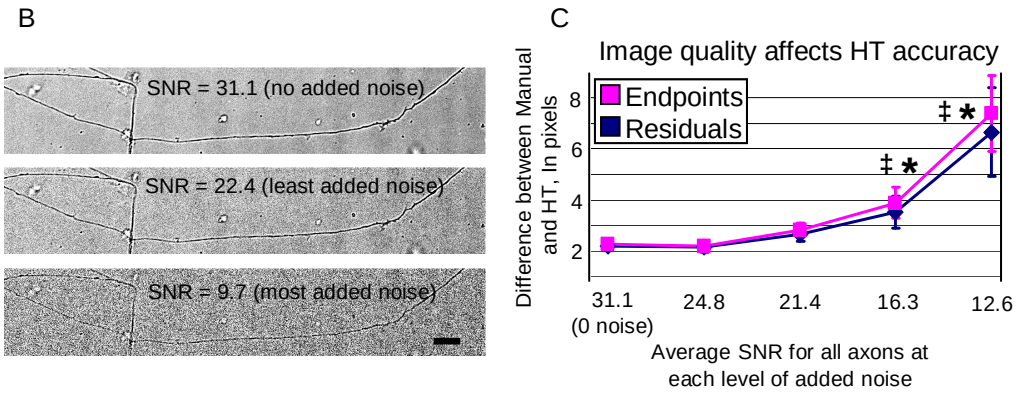

Figure 5: Robust Hough I. (A) Images of 14 different axons were analyzed using our algorithm. The HT is only able to identify linear structures in an image and so individual frames were broken into segments which contained linear sections of the axon. The parameters in this table define the standard criteria for which this algorithm was optimized. (B-C) To test the resilience of this algorithm to image noise, increasing levels of Gaussian white noise were added to a DIC image and the position of the resulting endpoint and centerline as determined by the HT algorithm were compared to those determined by manual user inputs. (B) Example of an unaltered image (top) and images with increasing levels of added noise. (C) The algorithm performed well for smaller levels of added noise, accurately identifying the axon to within seven pixels of its manually determined position, but at higher noise levels, both the discrepancy between the manual and automated selections increased as well as the variability in output from the automated algorithm. * and ‡ indicate groups that have statistically significant differences from the unmodified (no added noise) images for residuals and endpoints, respectively. ($p<0.06$ for stars and $p<0.001$ for endpoints). Scale bar, 10μm.

Figure 6 shows the construction of a kymograph from a movie of a rat sensory neurons expressing GFP-actin. In this case, the axon was curved, requiring a number of smaller linear sections to be used (Figure 6 A-K). The HT was able to accurately identify the axon in regions as small as 50 pixels wide, which translates to the ability of this algorithm to detect a radius of curvature of approximately 14.5 microns. The segmentation boundaries were

user defined, offering the potential for error and so the dependence of the HT's accuracy on the boundaries' position was tested. The same region of the axon was analyzed multiple times, each time using different points to define the segment boundary. Nine small regions from different axons were chosen, such that one or both edges lay at an inflection point of the axon. An example is shown in Figure 6 L-P. This example segment was 74 pixels wide, but the others varied from 56 to 116 pixels wide, with an average width of 75.5. In all cases, the small region was expanded incrementally by the addition of 10, 20, 30, or 50 pixels of the flanking axonal segment on either side, so that the inflection points were now incorporated into the segment. For this example, regions were created with total widths of 94, 114, 134 and 174 pixels. Each region was then analyzed with the HT and the position of the endpoints for the resulting lines compared (Figure 6 R). These results suggest that the HT is largely insensitive to variations in user defined boundaries. Finally, it should be noted that one 46 pixel wide region performed poorly in this analysis and was not included in the presented data. The endpoints determined by the HT for all of the expanded regions were similar to each other, but below 50 pixels wide, this algorithm was unable to accurately identify the axonal section.

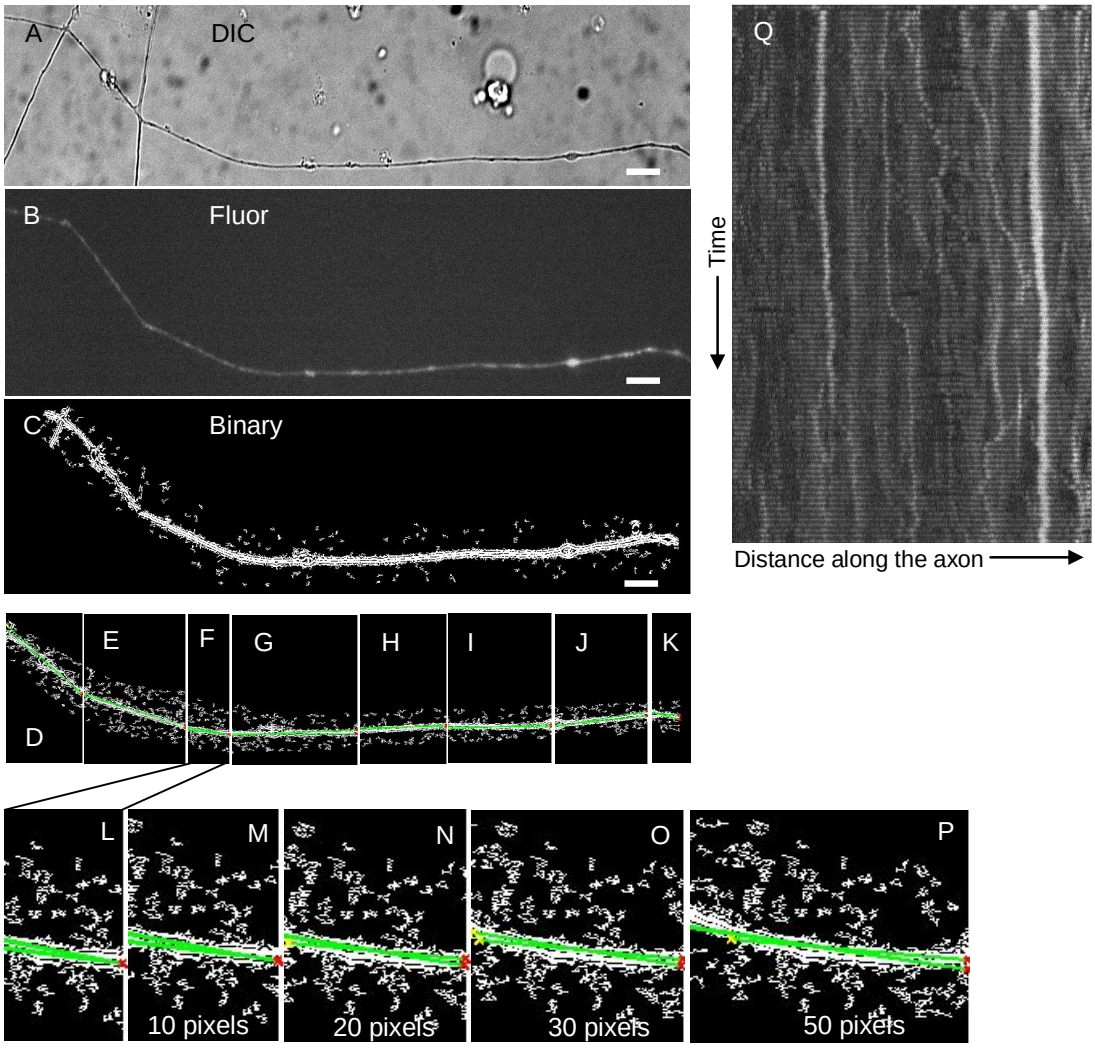

R

	Increase in section width in pixels added to each side			
	10	20	30	50
Manual vs HT endpoint in pixels. (LHS, RHS of the section)	(-0.8±1.9, -0.3±2.7)	(-2.1±4.1, -0.3±4.3)	(-2.0±2, 0.3±2.1)	(-0.3±3, 1.3±2.1)
Magnitude of difference between manual and HT endpoint. (LHS, RHS of the section)	(1.3±1.7, 2±1.9)	(2.9±3.9, 2.8±3.4)	(1.7±1.1, 1.6±0.6)	(2.7±1.7, 1.7±1.1)

Figure 6: Robust Hough II. (A) A DIC image of an axon transfected with actin GFP. (B) GFP-actin expression. (C) Binary image created from A after image filtering and thresholding as discussed in the text. (D-P) Binary images with endpoints and lines determined by the HT overlaid on top. (D-K) User-defined image panels used to approximate the curve of the axon showing the lines determined by the HT for each segment. These lines were used to create one continuous poly-line along the center of the axon. (L) Detailed view of panel F, 74 pixels wide. (M-P) Modified versions of panel L, used to illustrate the effect of the user defined segmentation boundaries. 10,

20, 30, or 50 pixels were added to each side of panel L to encompass more of the surrounding axon and then analyzed with the HT. The resulting lines, shown, were compared to that for L. (Q) Final kymograph of GFP-actin within axon. (R) The analysis was repeated for 8 additional axons (n=9 total) and the position of the end points of the center lines determined by the HT for the expanded panels was compared to their position in the original panel. The discrepancy and magnitude of the discrepancy between are summarized here. Scale bar, 10μm in all panels.

All of the characteristics discussed are vital to the utility of the Hough transformation as the central analytical tool in this algorithm; it can accurately track the axon despite inconsistencies in image quality, changes in axon shape and variability in user defined boundaries between segments of the axon, making it ideal for the often suboptimal images produced from biological experiments.

Discussion

A variety of cargoes move bidirectional between the cell body and the terminal of an axon. Tracking the movement of fluorescently labeled cargoes over time can provide insight into the biological mechanism underpinning this transport, as well as the conditions under which transport profiles change. Because of their inherent simplicity and reasonable accuracy, kymographs are frequently used in the analysis of axonal transport for fast cargoes. However, because of the longer imaging times required to accurately capture the motion of slow cargoes, the risk of artifacts or errors from changing axonal geometry is greater. This algorithm is particularly effective for these cases.

Regardless of their origins, though, there have been a number of successful efforts made to automate the detection of a particle's path from a kymograph (Mukherjee et al.; Welzel et al. 2009; Zhang et al.) but the methodology to create a kymograph has remained relatively underdeveloped, often at the expense of efficiency and accuracy.

In this paper we have described the development of an algorithm that can accurately detect the contour of an axon in individual frames of a time lapse movie and extract intensity profiles to build a kymograph. The traditional method used to build a kymograph is unable to deal with changes in axonal position and geometry which arise from translation due to drift of the microscope stage, or from motility and growth. These confounding issues result in inconsistent extraction and alignment of axonal contours, and thus, cargo positions. The robustness and accuracy of the alignment algorithm and the resilience of the HT to noise and user-based error were demonstrated by analyzing axons of dynamic and varied geometry (Figures 3-6). These analyses also highlighted the versatility of this algorithm in analyzing both punctate and more uniform fluorescent signals within the axon (Figure 3, 5). Our method achieved a significant reduction in the required user inputs and the produced kymograph was equal or superior to kymographs produced by manual tracing of either a single line in the first frame of the movie, or axonal contours in each frame of the movie (Figure 3D-F). By implementing a method of axon identification that is independent of fluorescent signal

distribution, intensity, and SNR, we have ensured both versatility and wide usability for this procedure.

The first step of this algorithm used a small region of the whole image (the saROI) to align an axonal reference point to the same coordinates in all frames of the TL. Alignment was achieved by comparing the region in one image to spatially shifted versions of that region extracted from the next image in the TL. This protocol is similar to other commonly used methods, such as correlation analysis (Anuta 1970; Barnea and Silverman 1972, Pratt, 1974 #1362), and was chosen here for its simplicity and ease of implementation. The selection of this reference point was at the discretion of the user. It was important that it lie on the axon in cases where significant axonal motility was observed in order to establish the necessary stationary reference point against which particle motion could be measured in a kymograph. In the case where axonal motility was low, this reference point could have been outside of the axon if necessary, such as a stationary marker on the substrate that might be used to correct for translation due to stage drift. For the needs of kymography, it was only necessary to align one axonal reference point at the beginning of the axon, rather than align the entire axon in all frames, a process which would require us to solve for a tensor that describes global rotational and shear deformations as well. Others have worked towards the development of “smarter” methods to direct the search for an optimal shift of the saROI to reduce computation time (see (Zitová and Flusser 2003) for a review), or towards methods to align an object

to a prototypical standard which can then be analyzed (Qu and Peng; Xin et al. 2007). By design we searched only for translational deformations; for simplicity, the image rotation was explicitly defined by the user rather than solved computationally. Additionally, applying a unique shear tensor to individual TL frames risked the introduction of motion artifacts into cargo tracks by changing the axonal geometry. While potentially useful in future extensions of this protocol, these more complicated methods were unnecessary for the simple translational alignment required here.

The Hough transform has been used extensively in image processing and computer vision for object detection because of a few key features: it is relatively insensitive to noise and it retains its accuracy despite broken or occluded features (Shapiro 1978). Additionally, it is amenable to parallel processing applications and can be used to detect multiple objects simultaneously (Illingworth and Kittler 1988). Despite its broad use in other fields, this is the first instance we know of in which the HT has been used for analysis of dynamic axons towards the creation of a kymograph, and more broadly, to examine protein mobility. Interestingly, the HT has been used in medical imaging applications (Dove et al. 1994; Philip et al. 1994), and a modified HT tuned to find ellipses has been used to find axons in an electron micrograph of a whole-nerve cross-section (Ying-Lun et al. 1996). The latter work also implemented a commonly employed, but computationally intensive, active contour model (ACM) in order to identify the boundaries of the internal and external sides of the axonal membranes. The ACM is an iterative energy

minimization process that utilizes “snakes,” which are splines guided by energy minimization functions that incrementally gravitate towards features of interest based on the particular minimization functions used as well as user inputs (Kass et al. 1988). The final position of the snakes is heavily dependent on their initial position and so this method is frequently used following another coarse localization procedure.

While an ACM or other comparable algorithms may be readily layered upon our simple application of the linear HT to individual image segments, such contour refinement is likely unnecessary. Standard kymograph generating programs require the user to trace a path composed of straight lines, so the use of the approximation here isn’t unwarranted. Additionally, the classic neuronal mechanics paper by Dennis Bray, suggesting that neurites in culture are under tension, was developed from the observation that the neuron is composed of linear regions connected by nodes (Bray 1973; Bray 1979; Letourneau 1975a; Letourneau 1975b). This linear approximation will fail at some point, but the theoretical limit for the radius of curvature we can detect is well below that calculated from reported observations of sensory neurons grown in culture; 99.7% of chick and frog axons have radii of curvature greater than 20.1 microns (Katz 1985). On the other hand, additional refinement might be useful to better define the profile of the axonal membrane, to answer questions regarding axonal diameter, membrane addition, filopodial protrusion, collateral branch formation, or even growth cone dynamics.

Our algorithm also has the potential for broader applicability. While our focus for this study has been on cultured neurons, the ability to track the movement of axons over time makes it particularly useful for axonal transport experiments in vivo, particularly those in Danio embryos, Drosophila larvae, C. elegans, or mammalian models (Bilsland et al.; Haghnia et al. 2007; Miller and Sheetz 2004; Zhou et al. 2001). Axon movement from animal motion as well as from breathing or pulsatile blood flow could all be efficiently accommodated using our algorithm.

Conclusions:

We have developed and tested an algorithm that automates the generation of and increases the accuracy of kymographs. This algorithm addresses the confounding changes in axonal orientation and geometry arising from stage translation or biological plasticity. The algorithm is based on the combination of straightforward and robust axon alignment and detection strategies. Our methods are resistant to noise in the images as well as to error in user defined parameters. This algorithm offers a new and powerful tool for use in the analysis of axonal transport, and should serve as a foundation upon which more sophisticated image processing applications can be built towards answering a myriad of other neurophysiological questions.

Chapter 3: Dynamic Actin Densities in the Axons of Sensory Neurons

Introduction

The cytoskeleton is vital for the development and maintenance of neuronal morphology, motility, and function. Dynamic forces between networks of microtubules, actin microfilaments, and intermediate filaments control axonal morphology and growth (Gallo et al. 2002; Heidemann et al. 1985; Lee and Cleveland 1996; Peters and Vaughn 1967; Yamada et al. 1971). In addition to their structural roles, microtubules and actin also support the long- and short-range movement, respectively, of a variety of cargoes within the axon through the activity of molecular motors (Bridgman 2004; Schnapp and Reese 1989; Vale et al. 1985a; Vale et al. 1985b) . Among these cargoes are cytoskeletal elements themselves, which are transported over a range of spatial and temporal scales to enable axonal outgrowth and pathfinding, regulate structural integrity, and guide the transport and localization of other cellular components.

Axonal transport of cytoskeletal proteins is an area of intense debate and active study. Initial radio-labeling experiments resulted in the parsing of bulk axonal transport into a fast component, which moves at upwards of 40mm/day and two slow components, slow component b (SCb) and slow component a (SCa), which move at 5-8 and 0.1-1 mm/day, respectively (Alvarez et al. 2000). Neurofilaments and microtubules, which primarily

occupy the axonal core, are transported in SCa (Black and Lasek 1980; Droz B 1963; Hoffman and Lasek 1975; Willard et al. 1974). Actin, which localizes largely to the cortex of the axon(Chang and Goldman 1973; Letourneau 1983; Nagele et al. 1988; Spillane et al. 2011), but also occasionally as short filaments within the axonal core, is transported in SCb (Willard et al. 1974). Mechanisms guiding axonal transport of neurofilaments and microtubules have been recently elucidated through live imaging experiments (Wang and Brown 2001; Wang and Brown 2002; Wang et al. 2000). Mobile neurofilament and microtubule units appear primarily to be short polymers several microns in length. Interestingly, neither cargo moves continuously at rates predicted by measurements of bulk transport. Rather, they move for short bursts punctuated by long pauses at instantaneous velocities similar to fast cargoes. Consistent with such rates of movement, neurofilaments, like many vesicular cargoes, are moved upon microtubules anterogradely (away from the cell body) by conventional kinesin and retrogradely (towards the cell body) by cytoplasmic dynein (Motil et al. 2006; Shea 2000). Interestingly, when the cargo binding domain of a dynein motor is bound to a structure offering high resistance, such as the actin network or other microtubules, the motor domain pushes mobile microtubules down the axon. Thus, counterintuitiviely, dynein is responsbile for the anterograde movement of microtubules (Ahmad et al. 1998; Baas et al. 2006; Hasaka et al. 2004). Motor proteins responsible for retrograde microtubule movement remain to be confirmed, but may include kinesin 5 (Myers and Baas 2007).

Mechanisms by which actin is transported in the axon are far less clear. Elucidation of these mechanisms is essential, given the critical roles for actin in such diverse cellular activities as adhesion, defining morphology, mechanical signaling, pathfinding, and anchoring of various organelles and protein complexes (Koenig and Letourneau 2009). Biochemical studies indicate that axonal actin exists dynamically in both soluble and filamentous states (Mills et al. 1996; Morris and Lasek 1984). A key role for microtubules in actin transport was suggested based on reduced bulk transport of actin in the presence of nocodazole (Banks et al. 1971a; Banks et al. 1971b). Recent work has suggested that actin and associated myosin motor proteins are neither directly responsible for SCb transport, nor does actin serve as a scaffold for other components of SCb (Roy et al. 2000; Roy et al. 2007; Roy et al. 2008). However, such hypotheses remain to be tested in the context of actin itself. Initial live imaging of fluorescence recovery after photobleaching (FRAP) of injected fluorescein labeled actin suggested that actin moved primarily as a soluble, diffusible cargo rather than through active, directional transport (Okabe and Hirokawa 1992). On the other hand, large complexes of actin “waves” have been observed in cultured hippocampal neurons (Ruthel and Banker 1998; Ruthel and Banker 1999) and in short axons in vivo (Flynn et al. 2009). These large, self-contained complexes of actin, similar in shape, size and dynamics to growth cones, move processively down the axon, and eventually fuse with the growth cone. In addition, GFP-actin expressed in the axon of cultured chick neurons forms transient patches of F-actin, a subset of

which give rise to axonal filopodia through an NGF-mediated signaling cascade (Ketschek and Gallo 2010; Spillane et al. 2011). Finally, indirect evidence inferred from the fluctuations of stationary mitochondria, which are likely docked to actin, suggests a baseline level of actin mobility in stationary axons that is enhanced in response to mechanical stimuli (Chetta et al. 2009).

In this work we have undertaken the first comprehensive characterization of actin mobility and the first systematic investigation of the mechanism underlying its transport in the axon. Using a combination of high resolution imaging, image processing and perturbation of various components of the cytoskeletal network, we have revealed novel dynamics within the axon, characterized by the appearance and disappearance of filamentous densities which move short but significant distances bidirectionally. These movements reveal some similar principles, but also key differences compared to the movement of fast cargoes, other cytoskeletal filaments and even other SCb cargoes. Our data suggest a novel mechanism of transport in which the connectivity between the actin and microtubule cytoskeletons plays a crucial role in regulating actin mobility in the axon. We demonstrate that such transport can contribute both to slow anterograde bulk axonal transport of actin as well as local biological function.

Methods:

Tissue culture and expression of fluorescent proteins

Dorsal Root Ganglia (DRG) were isolated from the entire spinal column of 2-5 day old Sprague-Dawley rats and maintained in ice cold F-10

supplemented with gentomycin. Cells were transfected with a plasmid encoding either GFP-actin, lifeact-tagGFP2, (ibidi GmbH, Germany), or maxGFP (Lonza, Walkersville, MD) through electroporation using an Amaxa Nucleofector II (Lonza, Walkersville, MD) following the protocol provided by Lonza. Briefly, after removal from the spinal column, the whole DRGs were incubated with 2.5mg/ml collagenase II (Roche, Basel, Switzerland) for 15 minutes at 37^{o}C, pelleted at 76xg for 5 minutes, triturated in F-10, pelleted again and resuspended in electroporation media with 3mg/ml DNA and immediately electroporated. After electroporation they were allowed to recover for 20 minutes in RPMI at 37^{o}C. Cells were then resuspended in growth media (10% Horse Serum in F-10, with 1% pen/strep,1% L-glutamine), seeded onto laminin coated glass bottomed dishes (MatTek, Ashland, MA) at a density of 100,000 to 250,000 cells/ml, and incubated at 37^{o}C and 5% CO_2 for 16-20 hours.

Chemical perturbation

For pharmacological experiments, cells were imaged for 6 minutes with images captured every 5 seconds in normal media. The appropriate drug was diluted in prewarmed media and added to the dish and the same axon was then imaged for an additional 20 minutes. All drugs were diluted from stocks dissolved in DMSO and care was taken so that the final concentration of DMSO in all experiments was less than 0.1%. The following concentrations were used: 10 μM Nocodazole (Sigma-Aldrich, M14047), 0.5 mM erythro-9-(2-hydroxy-3-nonly)adenine (EHNA, Sigma-Aldrich, cat# E114), 10 μM

latrunculin (Sigma-Aldrich, cat# L5288), 10μM jasplakinolide (Calbiochem, cat# 420107) or 25 mM 2,3-Butanedione monoxime (BDM, Sigma-Aldrich, cat# B0753). Animal work has been approved by the IACUC at the University of Maryland.

Immunocytochemistry

Cells were fixed for 10 minutes in 4% paraformaldehyde in PBS, rinsed well and permeabilized with 0.2% Triton X-100 in PBS for 10 minutes, incubated in blocking buffer (10% FBS, 3% BSA in PBS) for 30 minutes, and either incubated in primary antibody for one hour, followed by incubations with secondary antibody for one hour, or incubated with phalloidin for 30 minutes. The following antibodies and labels were used: for F-actin: AlexaFluor 594 phalloidin (Molecular Probes); for mitochondria: Mitotracker Red (Molecular Probes); monoclonal antibodies (Sigma-Aldrich) produced in mouse against ribosome (RPL-4), talin, and α-tubulin were labeled with secondary antibodies raised in goat conjugated to either AlexaFluor-488 or AlexaFluor-594 (Molecular Probes).

Live imaging of actin

For tracking the movement of individual actin densities, images were captured using a Nikon TE-2000E inverted widefield fluorescence microscope fitted with a 40x 1.35NA PlanApo oil-immersion objective, every 5 seconds. In some cases, additional high fame-rate movies were captured using a 100x 1.4NA PlanApo oil immersion objective, with images captured every 600ms.

The microscope stage was enclosed within an environmental chamber, which controlled temperature (37℃), humidity, and carbon d ioxide (5%). Care was taken to image axons with free growth cones, and which were not undergoing active bouts of elongation.

For fluorescence recovery after photobleaching (FRAP) experiments, a 30 µm long region of interest (ROI) in the axon was bleached and fluorescence recovery imaged using a Leica SP5X Laser scanning confocal microscope fitted with a 63x/1.4NA objective. Cells were maintained in an environmental stage enclosure at 37^{o}C and 5% CO_2. The ROI was bleached using multiple high laser power scans from an argon laser. Recovery of fluorescence was monitored with images captured every 1.2 seconds for the first minute and every 5 seconds until fluorescent intensity in the bleached region recovered to that of surrounding unbleached regions. Multiple 10x10 pixel square ROIs within the bleached region were then analyzed to examine spatial differences in the recovery rate. A fluorescent ROI away from the bleached region was used to normalize the ROI's intensity at each time point. The fluorescence recovery profile was then fit with an exponential curve and the time constant, tau, calculated to quantify recovery.

Image analysis

All image analysis was performed in ImageJ (NIH, Bethesda, MD) or MATLAB (The MathWorks, Natick, MA). Paired DIC and fluorescent images were captured every 5 seconds, and used to build kymographs for quantification of particle motion in the axon. Kymographs were built using a

novel semi-automated image processing algorithm (Ch.2). Briefly, images were rotated so that most of the axon was roughly horizontal (±15^{o} from the axis) and brought into register so that the beginning of the axon was positioned at the same point in all frames of a time lapse. Each DIC frame was filtered and made into a binary image that was divided into smaller regions at user defined inflection points along the axon. The position of the axon in these sections was automatically detected and an intensity profile was then extracted from the fluorescent channels and used for one row of the kymograph.

Individual trajectories on kymographs were traced manually. Errors in tracing were no more than 3 pixels from the centroid of a fluorescent particle. The paths of the actin particles were complex, traveling both anterogradely and retrogradely. Trajectories also appeared and disappeared during the movie (e.g., Fig 1A, described in additional detail in the results). The entire path of a particle was termed its “track” and tracks were categorized by the net displacement of the particle over its entire lifetime (Fig 1B). Those particles which achieved a net displacement in either direction of less than 0.3 microns during the 6 minute time-lapse were considered to be stationary, and those moving in either direction were categorized as anterograde or retrograde, as appropriate. 0.3 μm was the distance traveled by 68% of the particles which were empirically considered to be stationary “by eye” in the kymographs.

To further quantify the dynamics of each particle's track, the track was broken into a series of "runs." A run consisted of that section of a particle's motion during which it was moving in one direction or remaining stationary. If the particle changed its behavior, either by pausing (if moving), starting to move (if paused), or reversing direction, it was considered a new run; as long as the particle moved in one direction, regardless of it's acceleration, it was considered a single run. Along with the direction of the motion, the duration in seconds of each run was calculated, as well as the distance traveled and the average and maximum velocities of the particles. A run was considered to be stationary if moved less than 0.11 μm in one 5 second time-step. Again this cutoff was determined empirically by the average displacement of those particles considered stationary by eye. An analysis of tracks allowed the quantification of the broad scale changes that occurred during a particle's existence, but analysis of the runs provided insight into the details of how that motion occurred. It is important to point out that a stationary track could contain anterograde or retrograde runs, and vice versa and so runs were analyzed in both directional and stationary tracks.

To quantify the global behavior of actin in the axon during imaging, two additional calculations were performed. In the first, the average net displacement for all particles in a movie was calculated by dividing the sum of the net displacement of all tracks by the number of tracks. This calculation did not take into account the variation in a particle's lifetime and so the average "instantaneous" displacement was also calculated. The total displacement

was calculated at each time step for all particles in existence at that time and then averaged over all time steps to produce a single average displacement for each movie. For most of the time steps these displacements were close to zero but there were intermittent spikes of high anterograde or retrograde movement. Despite the different formulas used for the two calculations, their results about the average displacement of actin densities during the time lapse were in strong agreement.

Statistics

Transport parameters (average velocity, distance traveled and the duration of the run) were collected from runs pooled from multiple experiments. Sample sizes are provided in figure and table captions. Because most data sets had a broad, non-normal distribution, a two-sample Kolmogorov-Smirnov test was used to test for statistical significance between distributions. To test for statistically significant differences in the number of tracks and runs, two-tailed heteroscedastic paired student's T-tests were used. Confidence values are indicated in the figure legends or captions for all tests.

Results:

Identity of actin densities

Dissociated sensory neurons from neonatal rats were transfected with GFP-actin and grown on laminin coated glass coverslips. Axons with

unimpeded growth cones were imaged and frequent densities of GFP were noted. A general low level of background fluorescence was apparent in transfected axons, but these dense spots of GFP intensity arose along the length, and frequently moved for a short distance before disappearing again. In other cases, the densities appeared, remained stationary and then disappeared a short while later. In many cases, the particles exhibited complex, bidirectional movement interspersed with brief pauses. Kymographs were constructed to summarize this movement (Fig 1A), and were subsequently analyzed to quantitatively define the behavior of these actin densities.

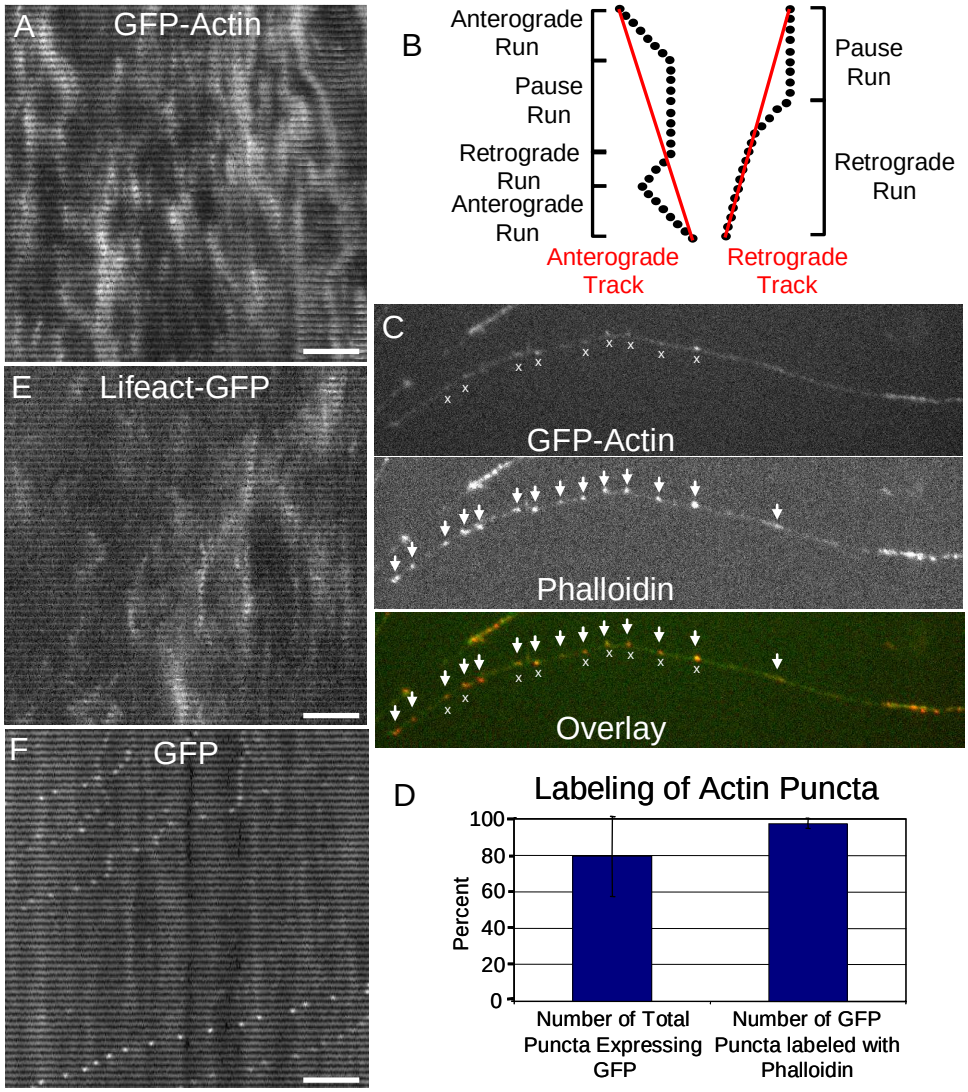

Figure 1: Particle mobility in the axon. Rat sensory neurons were transfected with either GFP-actin, Lifeact-TagGFP2 or the soluble fluorescent reporter maxGFP. Kymographs were used to quantify the movement of fluorescently labeled particles along the axon. (A) GFP-actin expressing axons exhibited puncta that appeared and disappeared, and moved bidirectionally with frequent pauses. (B) The entire particle track was broken up into short segments, called "runs" during which the particle moved in one direction or remained paused. A track was categorized as anterograde or retrograde directed based on its net displacement (Red lines). Note that anterograde tracks could contain retrograde runs, during which the particle moved in the retrograde direction, and vice versa. Also note that a change in velocity without a change in direction was still counted as a single run (e.g. retrograde track). (C) GFP-actin puncta were co-labeled with phalloidin, suggesting they are composed of filamentous actin. "x'' indicates the position of GFP-actin densities. The arrows indicate the position of phalloidin labeled puncta. (D) Nearly all of the GFP expressing puncta were labeled with phalloidin, but some phalloidin labeled puncta did not express GFP, suggesting that the GFP labeled actin puncta represent a subset of all actin densities in the axon. (E) The filamentous nature of these densities

was confirmed by expression of lifeact-TagGFP2, which only binds to filamentous actin and exhibited punctate expression in the axon with similar dynamics to those for GFP-actin (see Fig. 2). (F) The fluorescent signal in axons expressing maxGFP exhibited distinct behavior compared to both GFP-actin and Lifeact-TagGFP2 expressing axons. Many particles were indistinct and stationary, but fast moving retrograde particles were also apparent. Scale Bar: 10 μm in all panels.

First, in light of the reported presence of both soluble and filamentous pools of actin in the axon, (Allison et al. 1998; Cotman et al. 1974; Sankaranarayanan et al. 2003), the composition of the observed actin densities was examined. GFP-actin transfected cells were fixed and co-labeled with alexa-fluor-594-phalloidin, which binds only to polymerized F-actin (Fig 1C). The regions of the axon analyzed were an average of 32.4 microns in length, and the average distance between phalloidin labeled puncta was 1.1 microns. In four axons expressing GFP-actin, phalloidin labeled 90 out of 92 (97.8%) of the GFP puncta (Fig 1D). Importantly, there were several phalloidin stained puncta that did not express GFP, suggesting that fluorescent densities are representative of native structures.

Although no morphological differences or differences in phalloidin-labeled puncta were observed between GFP-actin expressing and non-expressing neurons, the actin filament binding protein Lifeact-TagGFP2 (lifeact) was used to confirm the identity of these particles as filamentous actin in live cells, free from more subtle effects of over-expression on the axonal cytoskeleton (Riedl et al. 2008). Dissociated sensory neurons were transfected with Lifeact-TagGFP2, and axons expressing the protein were imaged and analyzed using kymography (Fig 1E). Lastly, to confirm that the movement of these densities was specific to actin and not due to general

processing of soluble axoplasmic proteins, the fluorescent reporter maxGFP was expressed in cultured sensory neurons and kymographs created of the axons (Fig 1F). As an unconjugated fluorescent reporter, this served as a biologically inert marker. Qualitatively, kymographs of GFP-actin and Lifeact-TagGFP2 appeared similar, but distinct from maxGFP.

Quantitative characterization of actin mobility

Because of its complexity, the entire trajectory of a particle over its entire lifetime, or track, was divided into smaller directional sections called runs (Fig 1B, Methods). On average, anterograde and retrograde tracks were composed of 31±32% and 35±32% paused runs by time, respectively, and paused tracks spent 14±21% moving in the retrograde direction and 10±16% moving in the anterograde direction, by time. The average velocity, duration, and distance traveled by a particle were calculated for anterograde and retrograde directed runs, as well as for paused runs. Although the velocity and distance would seem to be unnecessary for a stationary particle, in fact these apparently stationary particles exhibited a very slow drift in response to certain perturbations, and could move a noticeable distance over the course of the six-minute imaging time. For clarity, statistically significant differences in parameters are summarized in charts within figures (Fig 2F, G; 4F, G; 5F, G), but raw cumulative histograms of these parameters can be found in supplemental figures (Fig S1, S2, S3) as well.

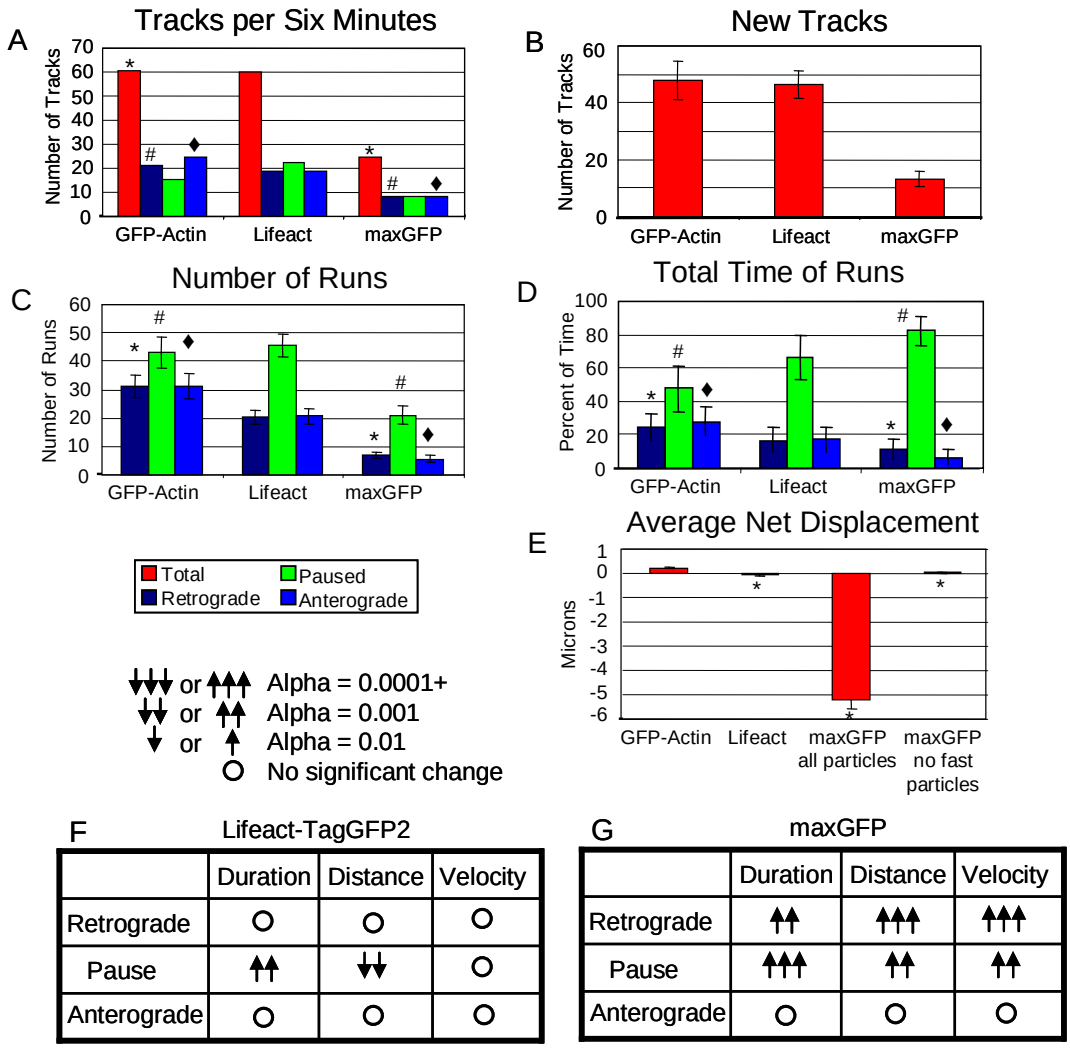

	Duration	Distance	Velocity
Retrograde	O	O	O
Pause	↑↑	↓↓	O
Anterograde	O	O	O

	Duration	Distance	Velocity
Retrograde	↑↑	↑↑↑	↑↑↑
Pause	↑↑↑	↑↑	↑↑
Anterograde	O	O	O

Figure 2: Transport characteristics of GFP-actin, Lifeact-TagGFP2 and maxGFP in axons. GFP-actin and Lifeact-TagGFP2 expressing axons exhibited distinct differences in a number of transport parameters compared to maxGFP. A student's T-test was used to test for significant differences between the groups. The *, #, and ♦ indicate those groups which were statistically different from GFP-actin with an alpha = 0.01 (A) GFP-actin and Lifeact-TagGFP2 were both more dynamic than maxGFP, exhibiting a larger number of tracks on average during each 6 minute movie. However, GFP-actin had a larger proportion of anterograde and retrograde directed tracks compared to Lifeact-TagGFP2 which had a larger number of paused tracks. (B) Similarly, both GFP-actin and Lifeact-TagGFP2 had a larger number of new tracks begin during the imaging time. (C) Tracks were divided into runs, and GFP-actin and Lifeact-TagGFP2 exhibited a larger number of runs on average than maxGFP during the imaging time. Additionally, maxGFP expressing axons had a disproportionately large number of stationary runs compared to Lifeact-TagGFP2 and GFP-actin. (D) MaxGFP particles spent a significantly larger amount of the total time paused. (E) GFP-actin expressing axons exhibited a slight anterograde average net displacement, while Lifeact-TagGFP2 exhibited net displacement of zero. The average displacement for maxGFP expressing axons was dominated by the fast

moving retrograde particles, resulting in significant retrograde movement. When these particles were not included in the calculations, the net displacement decreased to zero. (F, G) The average velocity, the duration in seconds, and the distance traveled by a particle during a run were all calculated for Lifeact-TagGFP2 (F) and maxGFP (G) expressing cells. A Kolmogorov Smirnov test was used to determine statistically significant changes in these axons compared to GFP-actin expressing axons. Confidence values for the change are indicated by the number of arrows, and the direction of the arrow indicates whether it increased or decreased. An open circle indicates no statistically significant change.

Analysis of kymographs made from axons expressing GFP-actin, lifeact, and maxGFP revealed a number of significant differences in transport parameters. First, the number of distinguishable tracks in maxGFP expressing axons was much lower than in axons expressing GFP-actin or lifeact (Figure 2A). Particle “births,” quantified as the number of new tracks originating during the course of the six minute imaging period, also occurred significantly less frequently in maxGFP expressing axons (Fig 2B). Similarly, the number of runs was much lower in maxGFP expressing axons than those expressing either GFP-actin or lifeact (Fig 2C), and well over 80% of the total combined time for all runs in maxGFP expressing axons was spent stationary (Fig 2D).

Collectively, the net displacement for GFP-actin was slightly, but significantly, positive, with a calculated average displacement of 0.23±0.09 μm per track within the imaging period (Fig 2E). The average duration for all tracks was 71.5 seconds, corresponding to an average rate of up to 0.8 mm/day, which is slower than SCb transport rates, but well within transport rates for SCa. The average velocity for anterograde directed runs was much

faster than this, with an average rate of up to 8.5mm/day, commensurate with the maximum reported velocities for SCb cargo transport. This average net displacement was significantly different from that of lifeact, which was essentially zero. The low average net displacement for lifeact was due to the fact that stationary runs were stationary for a longer percentage of time than for GFP-actin particles, although there were no statistically significant differences in the duration, velocity, or distance traveled by particles which were moving in either the anterograde or retrograde direction (Fig 2F, Fig S1). GFP-actin average net displacement was also significantly different from that of maxGFP. The most notable feature of maxGFP kymographs was the numerous maxGFP labeled fast vesicular cargoes (Fig 1F), which moved primarily in the retrograde direction. This phenomenon was observed only once in all of the GFP-actin kymographs (>1,200 tracks). These fast moving cargoes dominated the calculation for average net displacement (Fig 2E) resulting in a very large retrograde value for maxGFP expressing axons. Average net displacement calculated without the fast moving maxGFP particles was not significantly different from zero, due the stationary nature of maxGFP labeled particles not associated with vesicles. Finally, compared to GFP-actin, maxGFP particles had larger paused and retrograde directed durations, distances, and velocities (Fig 2G). Collectively, these data suggest that both the existence and observed motion of GFP-actin densities are specific to filamentous actin, and that this GFP-actin construct is a reliable reporter of the activity and position of actin in the axon.

Table 1: Comparison of transport parameters in GFP-actin, lifeact, or maxGFP expressing axons.

	GFP-Actin	Lifeact	maxGFP
Retrograde Duration (seconds)	26.29±18.35	22.96±14.78	43.1±36.77
Retrograde Distance (Microns)	-1.51±1.47	-1.33±1.29	-14.7±17.29
Retrograde Velocity (Microns/Second)	-0.059±0.036	-0.056±0.038	-0.236±0.182
Pause Duration (Seconds)	35.51±38.39	47.43±48.46	130.67±90.36
Anterograde Duration (Seconds)	28.79±19.3	25.45±14.88	22.13±10.82
Anterograde Distance (Microns)	1.73±1.47	1.25±0.94	1.72±1.6
Anterograde Velocity (Microns/Second)	0.064±0.041	0.052±0.03	0±0.052

Assembly of actin densities

A key and unique feature of the actin densities was their appearance and disappearance over time. Having demonstrated that they were composed of polymerized actin we next evaluated the possible role of monomeric G-actin using fluorescence recovery after photobleaching (FRAP) within a region of interest (ROI) (Figure 3). Two major findings were of particular interest. First, the rate of recovery was quite rapid. The time constant for complete recovery after bleaching was 12.8±8.3s corresponding to a diffusion constant of ~70 μm^2/sec, which is similar to previous values reported for actin monomers in endothelial cells (McGrath et al. 1998). Additionally, the dynamics of the recovery appeared distinct from dynamics observed for actin densities in kymographs. First, the directional movement of bright actin

densities into the bleached region was not observed. Second, in a few cases, recovery was not uniform within the bleached region. Rather, there were islands in the middle of the bleached region which were brighter before bleaching and which recovered fluorescence much faster than the surrounding axon (Fig3B-C).

To further examine the dynamics surrounding a particle's inception and disappearance, higher resolution and higher frame rate movies were made using a 100x oil immersion objective with images captured every 600ms. Selected frames from one of these movies (Fig 3C) and a kymograph of a small section of the axon illustrate the characteristic appearance and disappearance of a particle (Fig 3D, black arrow) in the absence of photobleaching. ROI analysis was used to calculate the average fluorescent intensity in sections of the axon around this particle (colored boxes in figure 3C) and line traces illustrating the average fluorescent intensity over time for five of these regions are plotted (Fig 3E). An obvious peak in fluorescent intensity appears around 60 seconds, which moves to the right before dissipating (Fig 3D-E). Before and after this peak, the density is more diffuse and this coalescence followed by dissolution seems to be characteristic of both GFP-actin densities as well as lifeact densities (Fig 1, 2), suggesting that small actin filaments are undergoing bouts of organization and disorganization.

Though there is a clear narrowing of densities during coalescence, this occurs without apparently diminishing the overall fluorescence in regions of

the axon flanking the density. To test for the possibility of local actin synthesis, the axons of untransfected cells were co-labeled with phalloidin and with an antibody against RPL-4, a ribosomal protein. Although both ribosomes and actin exhibited punctate expression in the axon, there was minimal overlap between the two (Fig 3G), suggesting that the birth of these densities was unlikely to result from local synthesis.

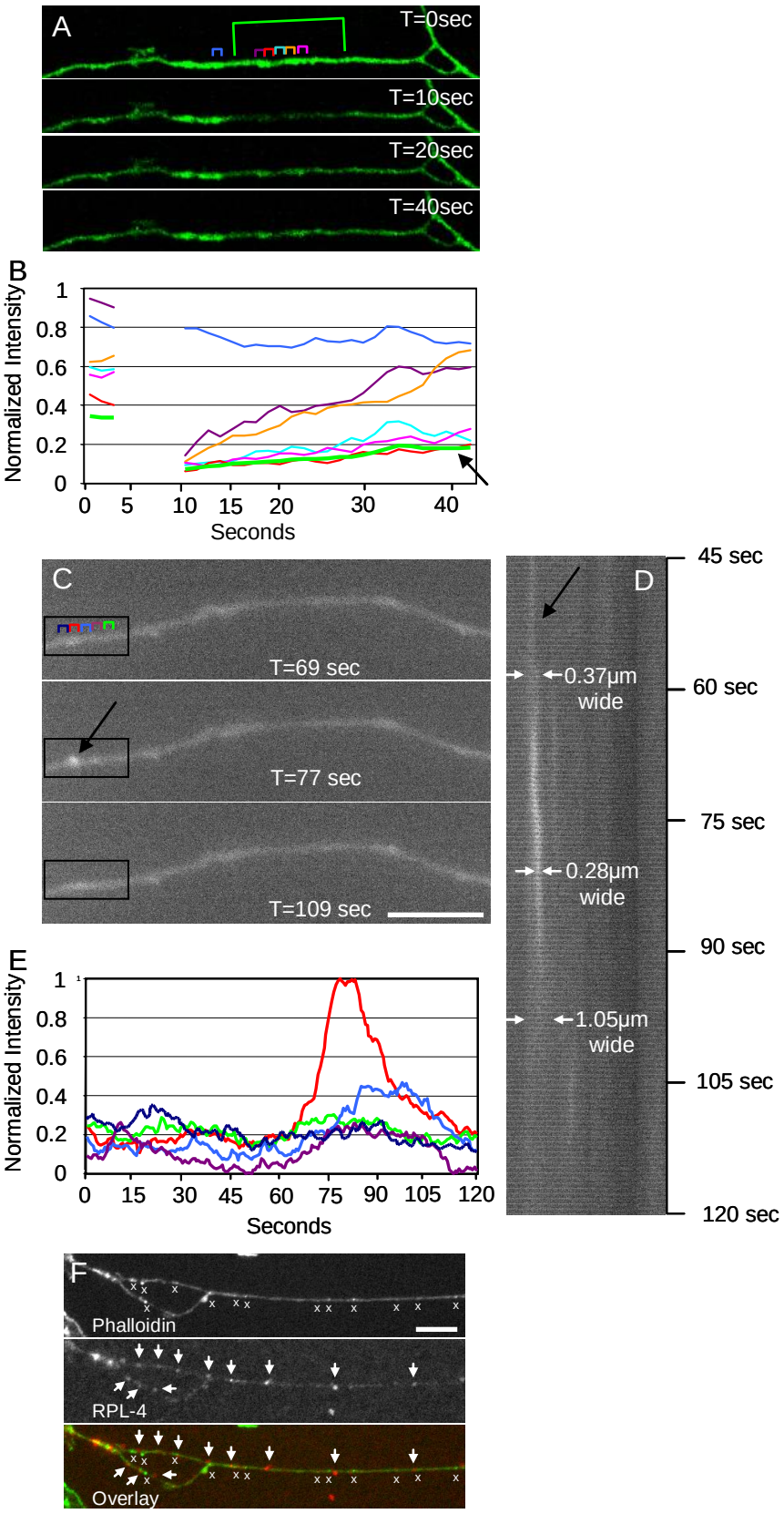
A
T=0sec
T=10sec
T=20sec
T=40sec
B
Normalized Intensity
1
0.8
0.6
0.4
0.2
0
0 5 10 15 20 30 40
Seconds
C
T=69 sec
T=77 sec
T=109 sec
D
45 sec
60 sec
75 sec
90 sec
105 sec
120 sec
0.37µm wide
0.28µm wide
1.05µm wide
E
Normalized Intensity
1
0.8
0.6
0.4
0.2
0
0 15 30 45 60 75 90 105 120
Seconds
F
Phalloidin
RPL-4
Overlay

Figure 3: Actin density identity. Fluorescence recovery after photobleach (FRAP) was used to determine the contribution of monomeric soluble actin to the movement of actin in the axon. (A) A 30 µm long region of the axon (indicated in green) was bleached and observed for recovery of fluorescence. A number of 10x10 pixel regions of interest (ROIs) inside the axon were used to quantify the changing fluorescent signal over time. These are indicated by the colored brackets flanking the axon. (B) Fluorescence recovery for the entire bleached region (thick green line, arrow) was used to calculate the time constant and diffusion coefficient for actin-GFP. Fluorescence recovery was not uniform within the bleached region though; the purple and the yellow regions recovered fluorescence much faster than the surrounding axon. (C) In another experiment, high magnification and a high frame rate were used to capture the birth and death of an actin density (arrow) in detail. Selected frames from the time-lapse are shown. Scale bar: 5 µm. (D) A kymograph of the region outlined by the black box in C between 45 and 120 seconds, illustrating the change in width of the particle track (black arrow) over time, suggesting that these particles are mediated by condensation and dissolution of bundles of actin filaments. (E) Line traces of the fluorescent intensity over time in the colored 10x10 pixel ROIs shown in C. Note the increased fluorescent intensity corresponding to the particle birth (red trace). (F) Lack of ribosomal co-localization with actin. Axons were stained for RPL-4 and labeled with phalloidin as well. “x” indicates phalloidin labeled puncta. The arrows indicate RPL-4 positive puncta. Scale bar: 10 µm.

Microtubule-based influences on actin mobility

Nocodazole: Having characterized the identity and movement of GFP-actin densities, an examination of the mechanism underlying the observed motion was undertaken. We first examined the role of microtubule-based transport on actin mobility by exposing cells to 10µM of nocodazole, a concentration which induced growth cone collapse in some axons within 5 minutes. Untreated axons exhibited small discontinuities in tubulin staining (Fig 4A) but treatment with nocodazole produced noticeable disruptions in the continuity of the microtubule cytoskeleton in many cases, severely, within 20 minutes (Fig 4B). Analysis of kymographs of axons exposed to nocodazole revealed significant changes in a number of transport parameters. First,

anterograde average net displacement increased in magnitude, though not significantly (Fig 4D). A systematic inspection of transport parameters provided insight into this increase. There were no changes in bidirectional velocities, but significant increases both in run duration and run distance in both directions (Fig. 4H), suggesting a minimal effect of these parameters to the increased displacement. Conversely, although moving tracks decreased in number (Fig 4E, G), anterograde directed tracks still comprised a larger percentage of the total number of tracks (Fig S4C), suggesting a contribution of these tracks to the increased anterograde displacement. Interestingly, the major determinants for the increased displacement were the small, but significant anterograde movements of stationary particles. Although the number of stationary tracks decreased (Fig 4F), the increased duration of anterograde drift in paused runs resulted in an increase in the average distance traveled from 0.03±0.3 microns in untreated axons, to 0.12±0.6 microns after treatment (Fig 4H, S2D). Collectively, then, although destabilizing microtubules decreased the total number of moving particles in the axon, when a particle did move, it did so for a longer duration, and covered a greater distance. This served to amplify the net anterograde displacement observed in untreated axons, through the increased anterograde displacement of both moving and paused particles.

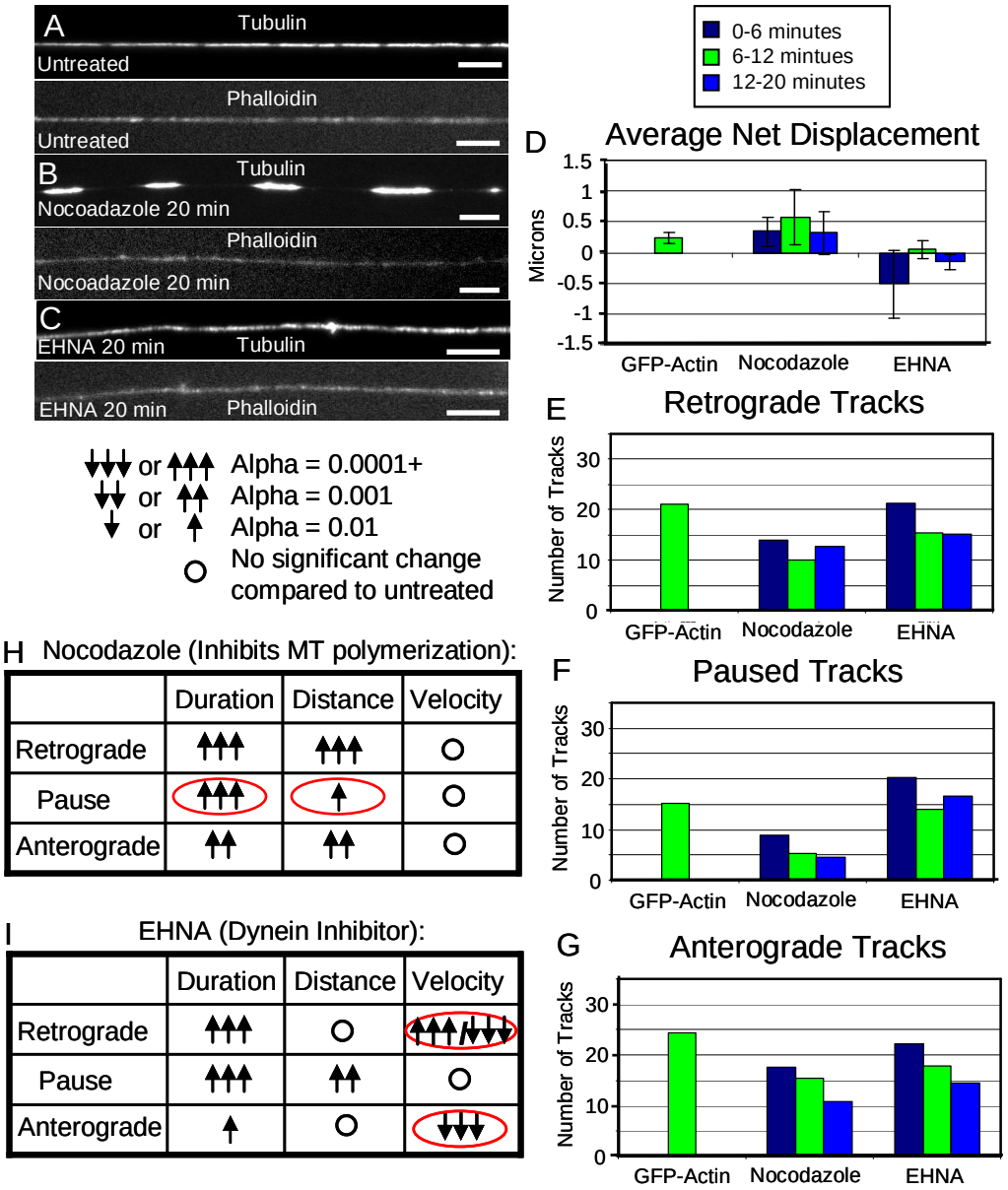

Figure 4: Effect of microtubule associated drugs on the mobility of actin densities in the axon. (A-C) After exposure to either nocodazole (B) or EHNA (C), cells were fixed and stained for actin and tubulin to determine the effect of drug treatment on the axonal cytoskeleton. Note the disruption of microtubule continuity after exposure to nocodazole (Scale bars 10 μm). (D) Nocodazole exposure increased average net displacement in the axon, while EHNA treatment initially induced a strong retrograde displacement, which then diminished over time. (E-G) Both nocodazole and EHNA affected the overall number of tracks over time as well as the direction of those tracks. (H) Nocodazole increased the dynamic nature of actin mobility in the axon, increasing the duration and distance traveled for all three phases of motion. The effect on paused particles was particularly striking as they moved a significant distance in the anterograde direction, thus contributing to the observed anterograde average net displacement. (I) EHNA treatment initially increased the velocity with which retrograde particles moved, which contributed to the net retrograde average

net displacement. However, over time, EHNA decreased the overall dynamics of actin mobility. Particle tracks lasted longer, but moved more slowly.

EHNA: Given the interaction of dynein and the cortical actin network in the anterograde transport of short microtubules (Hasaka et al. 2004; Schnapp and Reese 1989), we examined the converse possibility that dynein could move smaller, more mobile actin densities in the retrograde direction upon microtubules. To test this hypothesis, neurons were treated with 0.5mM EHNA, a drug shown to selectively decrease retrograde axonal transport by inhibiting the action of dynein (Ekstrom and Kanje 1984; Forman et al. 1983; Penningroth et al. 1982). While EHNA's interference with actin dynamics has been reported for higher concentrations of EHNA (additional details on possible non-specific effects in the discussion), phalloidin staining in fixed cells after exposure to 0.5mM EHNA for 20 minutes shows no obvious disruption of actin in the axon (Fig 4C, cf. latrunculin treatment in Fig 5B), and only very slight changes in lamellae. Similarly, EHNA exposure resulted in no obvious changes to the integrity of axonal microtubules (Fig 4C). EHNA treatment did, however, induce a rapid and significant retrograde average net displacement during the first 6 minutes of exposure, which gradually abated (Fig 4D). The initial reduction in average net displacement was due in part to a slight decrease in the number of anterograde and stationary tracks (Fig 4E, G) and a decrease in anterograde velocity (Fig 4I, S2E; Table 2). However, the primary contributor to the retrograde displacement was a dramatic doubling of retrograde run distance resulting from the increased average

velocity of retrograde particles (Fig 4I, S2F, G; Table 2). Consistent with this, stationary particles also drifted retrogradely in response to EHNA treatment. However, after 12 minutes of exposure, anterograde track number continued to decrease (Fig 4G), the average velocity in both directions decreased and stationary particles regained a slight anterograde drift (Fig 4I). Additionally, EHNA treatment resulted in a significant 40% reduction in the number of runs per track (Table S1), suggesting that the ability of actin densities to transition between the different directional phases was inhibited. Taking into consideration all of these changes, EHNA treatment seems to have reduced the mobility of actin bidirectionally after the initial burst of retrograde mobility.

Actin-based influences on actin mobility

Latrunculin: We next tested the hypothesis that the actin cytoskeleton influences the mobility of actin densities. First, we tested the importance of the structural integrity of the actin cytoskeleton on actin transport. Axons were exposed to 10μM latrunculin, which, by binding to actin monomers, prevents the polymerization of actin filaments and results in a disorganized actin cytoskeleton over time (Coué et al. 1987). Phalloidin staining of cells treated with latrunculin for 10 minutes revealed a severely disrupted lamella and regions of the axon either void of actin or containing actin–enriched puncta (Fig 5A, B, E). Additionally, the axonal microtubule network was also moderately disrupted, (Fig 5B), confirming the interconnected nature of the actin and microtubule networks (Baas et al. 2006). It was not possible to fix

and reliably stain cells exposed to latrunculin for the full 20 minutes, as the staining protocol washed cells from the coverslip, presumably due to increased structural fragility and actin-associated adhesion. Not surprisingly, given that actin densities appear filamentous, latrunculin treatment resulted in a reduced number of total tracks as well as new tracks appearing over the course of 20 minutes (Fig S4A, Table S1). The densities that were observed appeared similar to those in GFP-actin controls. As with all drug treatments, latrunculin induced a significant increase in pause duration, implying some role of the actin cytoskeleton on actin mobility. Like EHNA, latrunculin induced a strong retrograde average displacement at early time points (Fig 5F), driven in large part by a significant increase in retrograde velocity (Fig 5J, S3E; Table 2) and a concomitant increase in the distance and duration of retrograde directed runs (Fig 5J; Table 2). Unlike EHNA, latrunculin did not affect the velocity of anterograde directed particles, but did induce an increase in anterograde duration and distance that slightly counteracted the retrograde average net displacement (Fig 5G). At later time points, net average net displacement as well as the number of anterograde, retrograde, and stationary tracks all rebounded slightly, though not quite to control levels (Fig 5F-I). Overall, the net retrograde shift in mobility suggests an important role for an intact actin cytoskeleton in guiding actin mobility.

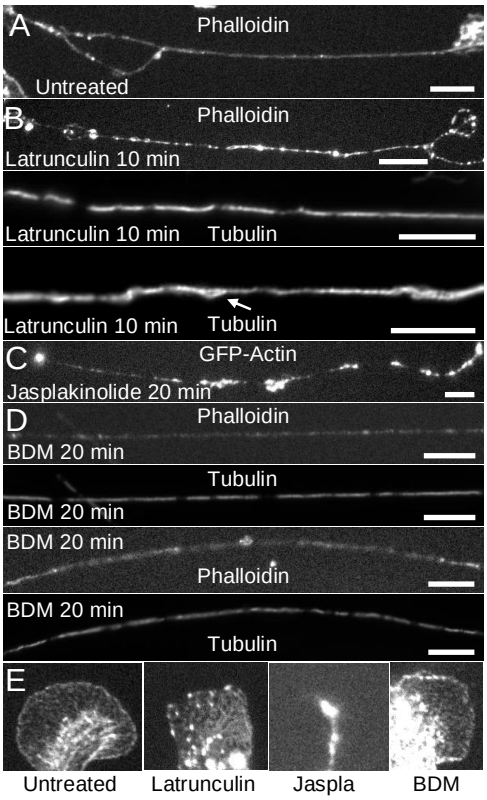

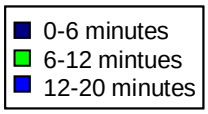

F Average Net Displacement

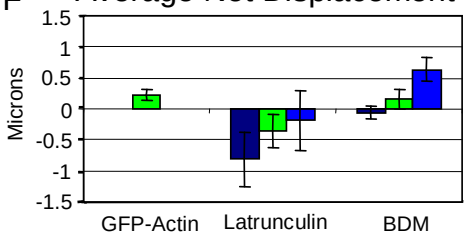

G Retrograde Tracks

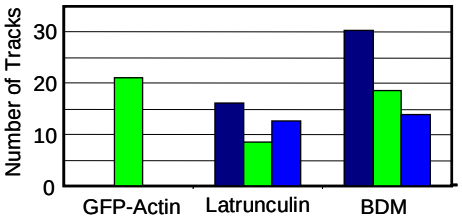

H Paused Tracks

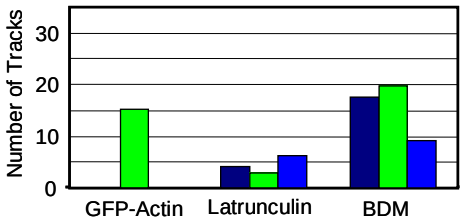

I Anterograde Tracks

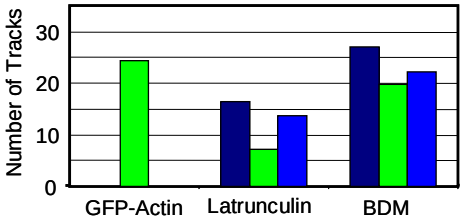

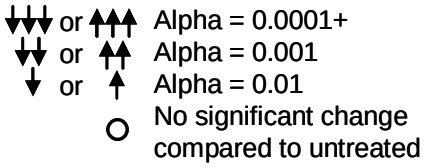

J Latrunculin (Inhibits actin polymerization):

	Duration	Distance	Velocity
Retrograde	↑↑	↑↑↑	↑↑↑
Pause	↑↑↑	↓	○
Anterograde	↑	↑↑↑	○

K BDM (Myosin Inhibitor):

	Duration	Distance	Velocity
Retrograde	○	○	↓↓
Pause	↑↑↑	○	○
Anterograde	○	○	↓↓

Figure 5: Effect of actin associated drugs on the mobility of actin densities in the axon. (A-E) After exposure to either latrunculin (B) or BDM (D), cells were fixed and stained for actin and tubulin to determine the effect of drug treatment on the axonal cytoskeleton. C is a frame from a time lapse movie of an GFP-actin axon treated with Jasplakinolide. Note that latrunculin affected the distribution of actin, but also seemed to affect microtubule integrity as well; some microtubules buckled, and protruded through the axonal cortex (arrow). (E) Latrunculin and jasplakinolide had a significant effect on the distribution of actin within the growth cone. BDM treatment induced a less severe disruption. Scale bars 10 μm, all panels. (F) Latrunculin exposure increased retrograde average net displacement in the axon initially, but this effect gradually decreased over time. BDM treatment induced a strong anterograde average net displacement which increased over time. (G-I) Both latrunculin and BDM affected the number of tracks over time as well as the direction of those tracks. Note that BDM preferentially reduced the number of retrograde and paused tracks. (J) Latrunculin increased actin particle dynamics, increasing the duration for all three phases of motion and increasing the distance traveled by moving particles. The retrograde velocity was most significant, though, in affecting the retrograde average net displacement. (K) BDM reduced the speed with which particles moved and increased the pause duration. It induced an increasingly strong anterograde average net displacement by reducing the number of paused and retrograde directed tracks.

Jasplakinolide: To further test the role of actin in directing actin transport, neurons were exposed to 10 μM jasplakinolide, which induces actin polymerization in cells by enhancing the rate of filament nucleation in a manner that depends on the concentration of monomeric actin (Bubb et al. 1994; Bubb et al. 2000). Treatment with jasplakinolide had a dramatic effect on actin in the axons (Fig 6C). Almost immediately upon addition of the drug, large fluorescent densities appeared along the axon, which did not move for the remainder of the imaging time; there was a complete cessation of all activity. Growth cones were also severely compromised, collapsing rapidly to a brightly fluorescent dense point. The rapid rate at which these densities formed is consistent with a large pool of soluble monomeric actin implied by rapid FRAP (Figure 3). In combination with the results of latrunculin

treatment, these results suggest that polymerization and turnover are both vital to the existence and mobility of these densities.

BDM: To further dissect the role of actin networks on actin transport, the role of myosin motors, which have been implicated in the short-distance transport of a number of cargoes, including neurofilaments, was probed. (Bridgman 2004; Jung et al. 2004; Lalli et al. 2003; Rao et al. 2002). Neurons were exposed to BDM, a broad spectrum myosin inhibitor (Cramer and Mitchison 1995; Cramer and Mitchison 1997). Although the efficacy and specificity of BDM have been questioned in the past (Ostap 2002), considerable evidence suggests that BDM interferes with the activity of all myosins except non-muscle myosin II, which generates contractility. However, we provide additional details on possible non-specific effects in the discussion. In our rat sensory neurons, exposure to BDM induced only minimal actin disruption in the axon, and only a mild decrease in staining at the leading edges of lamellipodia, as determined by phalloidin staining of fixed cells (Fig 5D, E). Similarly, the microtubule cytoskeleton showed only slight changes in its continuity. Like all drugs, BDM induced an increase in the pause duration of actin densities. Unlike EHNA and latrunculin, a net increase in the anterograde average net displacement was observed over time (Fig 5F). Unlike the other drugs, BDM treatment decreased the velocity of both anterograde and retrograde directed runs (Fig 5K, S3A, B, and Table 2). Additionally, the net displacement of stationary particles was not significantly affected in one direction or the other (Fig 5K). The major contributor to

increased average net displacement was the decrease in retrograde directed and paused tracks, by 54% and 48%, respectively (Fig 5G, H), compared to anterograde tracks, which decreased only by 18% (Fig 5I). These results suggest that myosin is important for the bidirectional transport of actin densities in the axon, but may exhibit a retrograde bias.

Table 2. Comparison of transport parameters in axons treated with nocodazole, EHNA, latrunculin, or BDM.

	GFP-Actin	Nocodazole	EHNA	Latrunculin	BDM
Retrograde Duration (seconds)	26.29±18.35	32.9±22.65	31.1±21.21	35.28±27.45	25.62±17.58
Retrograde Distance (Microns)	-1.51±1.47	-1.91±1.9	-1.66±1.63	-3.1±3.42	-1.24±0.97
Retrograde Velocity (Microns/Second)	-0.059±0.036	-0.056±0.038	-0.058±0.043	-0.084±0.059	-0.05±0.031
Pause Duration (Seconds)	35.51±38.39	67.7±79	65.41±83.48	87.86±120.9	66.52±81.56
Anterograde Duration (Seconds)	28.79±19.3	39.97±28.83	30.07±19.2	41.65±32.59	28.73±18.91
Anterograde Distance (Microns)	1.73±1.47	2.21±1.9	1.69±1.42	2.69±2.55	1.42±1.08
Anterograde Velocity (Microns/Second)	0.064±0.041	0.066±0.046	0.058±0.041	0.067±0.04	0.052±0.029

Biological roles for actin densities

Filopodia: Actin densities have been implicated in the formation of axonal filopodia in chick DRG through mechanisms enhanced by, but not requiring NGF. (Ketschek and Gallo 2010; Spillane et al.). We examined the formation of axonal filopodia in our mammalian DRG model, free from NGF. Twenty-two untreated GFP-actin expressing axons were analyzed. Filopodia protruded outward from the axon (Figure 6). The time at which a filopodium first protruded from the axon was recorded, as well as the time at which it reached its maximum length and the time at which it had retracted completely

back into the axon. For those filopodia which remained extended at the end of the time-lapse, the last frame was counted as its time of retraction. Similarly, for those filopodia which were already visible at the beginning of the time lapse, their protrusion time was counted as the first frame. The maximum length achieved by a filopodium was also measured as well as and the angle at which it protruded from the axon. Only 54.5% of the axons had any filopodia. In those axons which exhibited filopodia, an average of 1.75 filopodia were observed along the axon per minute, which is comparable to previously reported rates (Ketschek and Gallo 2010). Additionally, only 51.4% of the observed filopodia were populated with GFP-actin. There was no difference between the total lifetime of filopodia which were populated with actin GFP and those that weren't. Similarly, there was no difference between the time it took those filopodia to reach their maximum length, or to disappear (Fig 6A). However, the maximum length of those filopodia without GFP-actin was significantly less than those associated with fluorescent actin (Fig 6B). While most filopodia protruded perpendicular to the axon (Fig 6C), it was not uncommon for a filopodia to protrude at a more acute angle (Fig 6D) or to move with respect to the axon, so that the angle between the two changed (Fig 6E). In fact, filopodia tended to protrude with their tips pointed slightly toward the cell body, but it is unclear if this indicates a polarity within the underlying actin cytoskeleton. Lastly, staining for the focal adhesion protein, talin, shows talin localization to the base of these filopodia, and in some

cases, filling the body of the filopodium as well, suggesting that these filopodia protrude from stable adhesive islands along the axon.

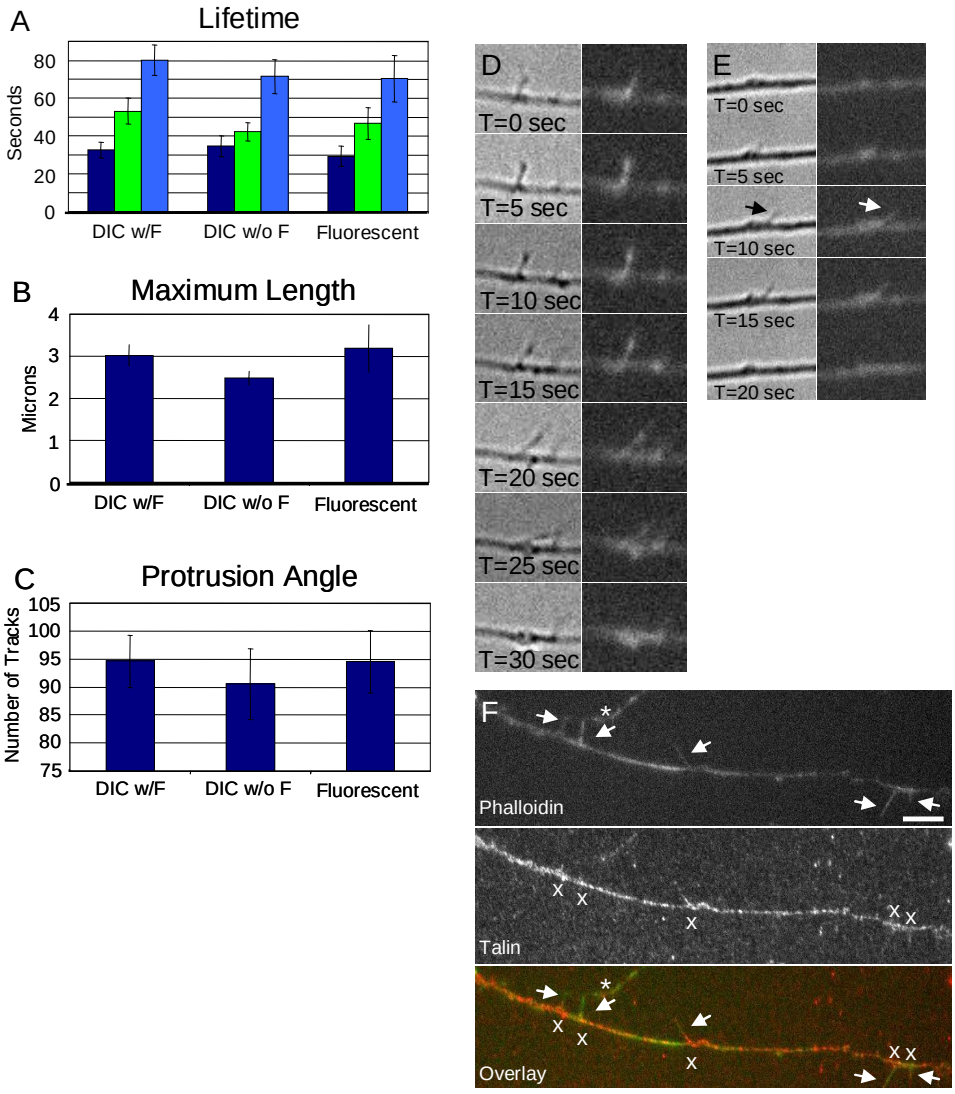

Figure 6: Filopodia and actin densities. A portion of the mobile actin densities gave rise to filopodia that protruded from the side of the axon. However, not all of the observed filopodia were populated with fluorescent actin. Lifetime, maximum length achieved and the angle of protrusion out of the axon were all measured in the DIC channel and compared between those filopodia which were populated with fluorescent actin (DIC w/F) and for those that weren't (DIC w/o F). Additionally, these same parameters were measured using only the fluorescent channel (Fluorescent). (A) There was no statistically significant difference between the lifetimes of these three groups. (B) But those filopodia which were not populated by fluorescent actin were statistically shorter than those with fluorescent actin (alpha=0.0008). (C) There was also no difference in the measured angle of protrusion for filopodia between these three groups. (D, E) Individual filopodia were quite dynamic, often protruding out of the axon at one angle, and then moving through an arc before retracting back

in. (F) The focal adhesion protein, talin, localized to the base of these filopodia, suggesting that they protrude from regions of stable adhesion to the substrate. Note that the starred filopodium at the top of the picture is actually protruding from another axon outside the field of view (Scale bar 10 μm).

Mitochondria: Previous work has shown that mitochondria are transported along the actin network by myosin, and require actin for docking in the growth cone (Morris and Hollenbeck 1995; Ruthel and Hollenbeck 2003). Additionally, stationary mitochondria are associated with actin in the axon (Kang et al. 2008; Ketschek and Gallo 2010; Miller and Sheetz 2006). Although the movement of the actin densities appeared qualitatively different from the movement of mitochondria in the axon, we labeled axons transfected with GFP-actin with Mitotracker Red in order to examine the possibility that the motion of GFP-actin was correlated with the motion of mitochondria. It is clear that only a small fraction of the actin particles are associated with mitochondria for substantial periods of time. Inter-mitochondrial spaces appear to be particularly dynamic (Fig 7A), but even the regions around the mitochondria show obvious motility (Fig 7B arrow). Additionally, not all of the mitochondria are labeled with actin (Fig 7B stars) suggesting that not all mitochondria are surrounded by actin. Finally, it is important to note that not all “stationary” actin particles are associated with a mitochondrion (Fig 8C arrows). While mitochondria may serve as a sort of scaffold for actin accumulation, or vice versa, the relationship between GFP-actin and mitochondria in these cultured sensory neurons appears to be more complex and dynamic than previously thought.

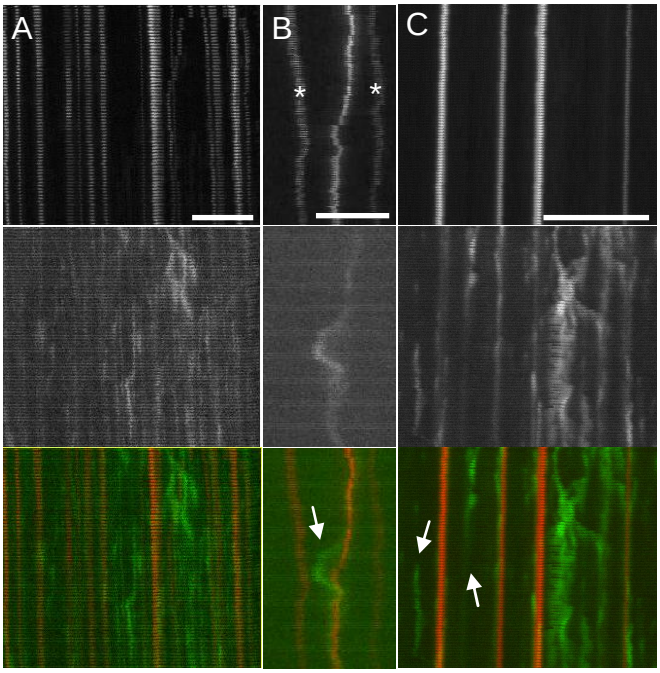

Figure 7: Actin's association with mitochondria in the axon. Axons were transfected with GFP-actin as well as with mitotracker red, and imaged over time. Kymographs from selected movies are shown here at 40x (A, B) and 100x (C). (A) Actin does associate with mitochondria but the inter-mitochondrial spaces appear more dynamic. (B) However, not all mitochondria are labeled with actin (stars) and the actin that is associated with a mitochondrion can still be active, as shown here (arrow) where an actin puncta moves away from the mitochondrion only to return a few seconds later. (C) Finally, not all stationary actin densities are localized to stationary mitochondria (arrows). Scale bars: 10 μm in all panels.

Discussion:

It is only recently that details have emerged regarding mechanisms by which slow cargoes are transported. Microtubules and neurofilaments, which exist in SCa, move as filaments several microns in length at fast instantaneous velocities punctuated by frequent pauses (Wang and Brown 2001; Wang and Brown 2002; Wang et al. 2000). On the other hand, a recent model proposes that cytosolic SCb cargoes form directional, transiently

associated multi-protein complexes, which display a net anterograde drift (Scott et al. 2011). However, details underlying actin transport have remained elusive. In this study, through the high resolution imaging of rat sensory neurons expressing GFP-actin and subsequent image processing, we have characterized the complex bidirectional movement of fluorescent actin densities. We have developed a novel model for the axonal transport of actin based on changes in this movement following the perturbation of specific components of the cytoskeletal network. We propose the coalescence of actin into short filamentous densities, which are then directionally translocated via contributions from coupled microtubule- and actin-based transport systems. Such transport can contribute both to the slow anterograde bulk axonal transport of actin as well as local biological function.

Composition and formation of mobile actin densities

Several results indicate that the mobile actin densities subsequently characterized are composed of filamentous actin. Most notably, these densities are labeled with both phalloidin and lifeact, which bind only to filamentous actin (Fig 1). Further, it appears that the coalescence, or birth, events responsible for the formation of visible densities represent a process in which stable polymerized actin is collected and bundled together. Such bundling is consistent with the similar number and dynamics of coalescence events observed in axons expressing lifeact compared to GFP-actin (Fig 2, Table 1). Additionally, imaging at higher temporal and spatial resolution

reveals the gradual transition from diffuse, but still distinguishable, puncta to a more intense and compact puncta prior to dissociation (Fig 3).

Given the concentration dependence of actin filament nucleation, polymerization may play an indirect role in the formation and existence of actin densities. For example, the puncta which recovered fluorescence most quickly after photobleaching (Fig. 3A) were also the brightest before bleaching. They likely were bundles of polymerized actin, which served as sites of high polymerization during fluorescence recovery. However, a mechanism in which polymerization alone is the major driving force in density formation seems unlikely, since the tight punctate signal would seem to require the simultaneous polymerization multiple densely packed filaments. Additionally, while latrunculin treatment decreased the total number of axonal densities (Table S1, S2), it did not change the appearance or dynamics of coalescence events. Finally, the lack of co-localization between actin puncta and ribosomes suggests that the densities are likely not formed through local actin synthesis.

While we cannot rule out the possibility that these densities are integrated within the actin cortex, and while no other studies have directly looked at this possibility, their dynamic natures suggests that they more likely exist as separate collections of F-actin. These findings are consistent with several electron microscopy studies, which reveal self-contained densities of F-actin lateral to the microtubule core as well as short actin filaments within

the core (Chang and Goldman 1973; Letourneau 1983; Nagele et al. 1988; Spillane et al. 2011).

Characterization of actin mobility

Qualitative inspection of axons expressing GFP-actin revealed dynamic and complex patterns of fluorescence. Through rigorous high-resolution imaging and image processing, we have quantified a number of parameters related to the instantaneous and longer-term movement of actin densities within the axon. The parameter which summarizes their global behavior is the average net displacement for all particles observed over a six-minute imaging period. However, to better understand the mechanisms underlying this displacement, full tracks were also broken into shorter runs comprised of either times during which the particle was stationary or was undergoing processive movement in either the anterograde or retrograde direction. Analysis of these runs revealed statistically significant directional changes in the duration, distance traveled, and average velocity in axons exposed to a variety of drugs that perturbed elements of the cytoskeletal network, as compared to untreated axons. As a brief comment on nomenclature, the word “transport” will be used to refer to any directed movement, and does not necessarily imply the long range processive movement normally associated with fast axonal cargoes; in the case of actin, movements were of short but significant duration and distance, often punctuated by pauses.

Actin densities as a mechanism for slow component transport

A key finding of this work was that GFP-actin in the axon showed a net anterograde displacement with a velocity of 0.8 mm/day. Though this average net displacement was slow, it was still significant and is commensurate with SCa transport rates. However, this displacement included contributions from retrogradely and anterogradely moving particles as well as paused particles. The average net displacement of moving particles yielded an anterograde velocity of 1.5mm/day, which is at the low end of SCb rates of transport, while the average net displacement of only anterogradely directed particles produced a velocity of 8.5mm/day, at the upper end of SCb transport rates. It should be pointed out that our methodology allowed us to track only densities with fluorescent intensities greater than the background fluorescence level. However, rates of FRAP suggest that diffusion of soluble actin in the axon is fast and shows no directional bias, indicating the absence of a significant concentration gradient within the axon. Thus while it is unlikely that diffusive movement contributes to directional actin transport, diffusion is likely to play a role by setting the G-actin concentration that ultimately drives polymerization of filaments.

Mechanisms for the movement of actin densities

A synthesis of the current models for transport in the axon, based on cell biological, biochemical, and biophysical literature suggests that non-diffusive directional, actin transport may be explained by one of four general

models: (1) actin polymerization or treadmilling; (2) actin movement upon microtubules, but not actin; (3) actin movement upon actin, but not microtubules or; (4) a hybrid of models (2) and (3), including contributions from both microtubules and actin.

There is little evidence in support of the first model. As described above, actin densities are composed of polymerized actin filaments, do not dramatically change their behavior in the presence of latrunculin, and do not display the characteristic treadmilling activity observed in the growth cone. To systematically examine the remaining models, we perturbed specific elements of the crosslinked cytoskeletal network and rigorously characterized parameters defining actin mobility.

Our data support the final model. Specifically, we conclude that particles are moved by myosin on actin tracks, but also as passive cargoes on microtubules being moved by dynein anchored to cortical actin (Figure 8). The evidence in support of this model will be discussed below, based on our analysis of the movement of actin densities as well as on previous work, particularly that of the Baas group. First, however, pharmacological treatment enabled tight temporal control over a particular perturbation, and the specificities of the reagents selected for this study are essential to interpreting our results. Possible non-specific effects are well documented in the literature so care has been taken to limit and/or quantify them. Although genetic manipulation might have facilitated more specificity, inactivation of

cytoskeletal proteins, which are involved in a number of cellular processes, would likely result in cell death or other less tractable side effects.

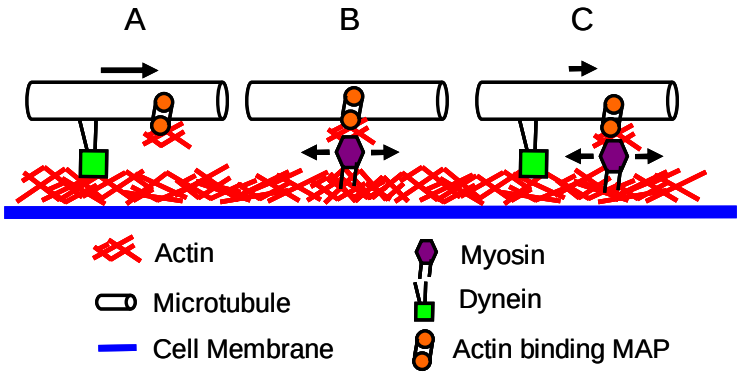

Figure 8: Model of actin mobility in the axon. The data support a role for both microtubules and actin in the transport of actin in the axon. (A) Actin is transported as a passive cargo on microtubules moved forward by the action of dynein. (B) Actin is also moved by myosin as a cargo along tracks of actin. (C) The loss of either actin or microtubules facilitates more robust movement suggesting that these two transport mechanisms act both as active movers of actin and as a brake to motion along the other.

A role for microtubules in actin transport

Treatment with nocodazole induced numerous changes in the measured transport parameters (Fig 4), indicating a role for microtubule stability and motor proteins in modulating axonal actin transport. However, this role appears distinct from the typical roles of microtubules in transporting fast or slow cargoes. Conventional transport of a cargo by kinesin or dynein, as observed for vesicular or neurofilament transport, assumes motor movement upon stationary microtubule tracks. If this were the case, then treatment with nocodazole should have inhibited the transport of actin bidirectionally. Although pause durations increased in response to nocodazole treatments, surprisingly, it resulted in an increased anterograde average net displacement. Both the duration and distance traveled during

runs increased as well as the anterograde drift of stationary particles. This response is markedly different from that of other SCb cargoes, which are unaffected by actin destabilization but cease movement bidirectionally after microtubule destabilization, presumably due to the absence of tracks for kinesin and dynein motors (Roy et al. 2008). Rather, the observed enhancement in anterograde mobility is reminiscent of the response of microtubules, whose anterograde movement via dynein, stabilized on actin tracks, was enhanced following their decoupling from microtubule scaffolds (Ahmad et al. 2006; Hasaka et al. 2004).

Intriguingly, several features of altered actin mobility following EHNA and latrunculin treatment were also consistent with dynein-mediated anterograde transport of microtubules upon intact actin scaffolds (Fig 8A). Actin densities in axons exposed to EHNA initially exhibited a large retrograde displacement, due to a reduction in their anterograde velocities and an increase in their retrograde velocities (Fig 4). This finding is opposite to that predicted for typical dynein-dependent retrograde transport, and provides strong evidence against a role for dynein in moving actin retrogradely in the axon. This interpretation holds true even factoring in unlikely, but possible, superposed non-specific effects on anterograde motors or actin polymerization (Penningroth et al. 1982; Schliwa et al. 1984; Walsh and Tellam 1986). Similarly, latrunculin also resulted in a large retrograde average net displacement. Taken together, the simplest explanation for these data is

that dynein does not directly move actin, but affects its movement indirectly, by moving microtubules on which actin is a passive cargo.

This model is also supported with data from nocodazole treated axons, where increased anterograde mobility may be explained by decreased connectivity within the axonal core (Figure 4), which frees up microtubules to be moved by motor proteins. The model is also consistent with multiple biochemical and electron microscopy studies. Structurally, actin is known to associate closely with microtubules in the axon (Chang and Goldman 1973; Letourneau 1983; Nagele et al. 1988)(Gallo et al., 2011), and the microtubule associated proteins, MAP2c, doublecortin, pod1 as well as a few different formins have all been shown to mediate actin dynamics, suggesting that microtubules could serve as a nucleation site for actin densities (Deeks et al.; Fujiwara et al. 1999; Roger et al. 2004; Rothenberg et al. 2003; Tint et al. 2009).

A role for actin in actin transport

While a bidirectional microtubule based model for actin transport is attractive in its simplicity, not all of the data are consistent with it. First, the instantaneous rates of movement for moving particles are far slower than those predicted by Baas and colleagues for microtubule-based transport. In fact, particles moved in both directions with average velocities of 0.06μm/sec, the same velocity reported for the movement of pigment granules carried along actin by myosin in fish melanocytes (Rodionov et al. 1998). Second,

retrograde microtubule transport is not affected by interfering with either dynein or actin (Ahmad et al. 2006; Hasaka et al. 2004), but in our experiments, both latrunculin and EHNA enhanced retrograde displacement of actin puncta (Fig 8b). Third, BDM treatment should have left transport unaffected if it were independent of myosin, even taking into account side effects on non-muscle myosin II (Chon et al. 2001; Forer and Fabian 2005; Yarrow et al. 2003). However, BDM significantly reduced the number of retrograde directed and paused tracks as well as the anterograde velocity. The milder effect on anterograde transport is consistent with the disruption of myosin mediated transport, but intact hitchhiking upon microtubules moving anterogradely against an intact actin cortex. This suggests a role for myosin in the retrograde movement of actin, but does not preclude one for piggy-backing on to retrogradely moving microtubules. Finally, treatment with jasplakinolide completely abolished any movement of actin within the axon, similar to previous reports of jasplakinolide induced inhibition of myosin mediated movement of vesicle bound cargoes (Semenova et al. 2008).

Interactions between actin and microtubule-based transport systems

A few results further support a stronger functional connectivity between actin and microtubules in our system. Both nocodazole and latrunculin treatments significantly increased the duration and distance traveled by particles bidirectionally. These results suggest a reciprocal inhibitory interaction between actin and microtubules; each serves to limit the

movement of actin densities along the other network. Destabilization of either decreased this inhibition and freed actin particles to move further and for a longer time. This seemingly passive inhibitory interaction is, however, likely a direct result of the active force generating components of the system. Myosin, dynein and other cross linking proteins are likely engaged in a sort of tug-of-war over these actin densities. When one protein “loses its grip” the actin is free to move for a short time, before it is rebound and frozen again (Fig 8C).

Implications for the organization and dynamics of the actin cortex

Changes in directional transport after microtubule destabilization with nocodazole could also suggest a directional bias in the orientation of actin filaments in the cortex. This type of organization has been proposed previously to explain the anterograde movement of mitochondria in microtubule depleted axons and neurofilaments after treatment with BDM (Jung et al. 2004; Morris and Hollenbeck 1995). In contrast to nocodazole treatment, when the actin cortex was interrupted by exposure to latrunculin, a net retrograde displacement of actin densities was observed, similar to the result of EHNA exposure. This retrograde average net displacement is likely due to the contractile nature of the actin cortex. On one hand, EHNA reduced the connectivity between actin and microtubules, and so freed actin to contract in a sort of contraction mediated translation of the actin framework (Miller and Sheetz 2006). Conversely, latrunculin treatment reduced the

connectivity within the actin cortex, but may have done so locally, causing actin to condense into disorganized puncta along the length of the axon.

Implications for neurobiological function

We have discussed polymerized and soluble actin in the context of axonal transport, but this transport occurs because actin is required for a number of biological functions at specific locations along the axon. To this end, while we have pooled our results, there is a strong possibility of functionally different populations within the pool of polymerized actin. We have built upon previous work noting that a subset of polymerized actin densities give rise to filopodia (Fig 6), and that some are associated with mitochondria (Fig 7) as well (Ketschek and Gallo 2010; Spillane et al. 2011). Additionally, our staining shows that actin densities co-localize with the focal adhesion protein talin (Figure 6F), as expected (Gardel et al. 2010). Surprisingly, although there is some co-localization with ribosomes in our axons (Fig 4F), the literature suggests a much stronger association between the two based on the importance of actin in transporting ribosomes and maintaining their distribution along the length of mature axons (Koenig and Koenig 2009; Koenig and Martin 1996; Koenig et al. 2000). One would expect the developing axon to require significant translational machinery as well. A quantitative study of the dynamic associations between actin densities and ribosomes or focal adhesion proteins along the length of growing axons would elucidate the possible interactions.

Summary and conclusions

Our data provide clear evidence for a novel mode of transport for actin densities in the axon. Short bursts of small but significant movement are mediated by both actin and microtubules to produce a net anterograde average displacement at speeds commensurate with slow component transport rates. These actin densities are filamentous in nature, and their emergence appears to be due to bundling and polymerization of filaments, rather than de novo translation. They are moved bidirectionally by the action of myosin motors, presumably walking along the actin cortex and a significant fraction of their anterograde movement seems to be as passive cargoes piggybacking onto moving microtubules. It is not clear what role, if any, this microtubule piggybacking plays in their retrograde movement. In addition to their active roles in transport, the actin and microtubule cytoskeletons each seem to serve as a brake on movement mediated by the other. Finally, these densities seem to have a number of biological functions, as they are associated with filopodial protrusion, and co-localize with mitochondria and the focal adhesion complex protein talin.

Chapter 4: Cytoskeletal dynamics in response to tensile loading of mammalian axons[2]

Introduction

Peripheral nerves are under tension and undergo additional tensile loading, or stretch, within a physiological range during growth and voluntary or imposed joint extension and flexion.(Topp and Boyd 2006) Nerves may be lengthened more dramatically during orthopedic or regenerative surgery, including limb-lengthening procedures. (Abe et al. 2004; Abe et al. 2002; Abe et al. 2003; Bora et al. 1980; Ichimura et al. 2005; Ikeda et al. 2000; Jou et al. 2000; Lee et al. 2006; Li and Shi 2006; Spiegel et al. 1993; Yokota et al. 2003). In vivo and in vitro animal models of nerve lengthening suggest that a threshold of strains and strain rates determines whether stretch is injurious or ameliorative, based on the structure and electrical conduction capabilities of the affected nerve.(Bueno and Shah 2008; Eggli et al. 1999; Shi and Whitebone 2006; Shibukawa and Shirai 2001) However, the mechanisms underlying this empirically determined threshold remain to be determined.

At the cell level, axons, situated between the adherent cell body and extending growth cone, are also thought to be under tension.(Bray 1979; Lambert de Rouvroit and Goffinet 2001) As is true for many cells of the musculo-skeletal system, (Smith and Gilligan 1996; Vandenburgh et al. 1991) neurons exhibit a morphological response to mechanical loading during

[2] This has been previously published as: Chetta J, Kye C, Shah SB. 2009. Cytoskeletal dynamics in response to tensile loading of mammalian axons. Cytoskeleton 67(10):650-665.

growth and development. In a “towed-growth” loading regimen, micromanipulator controlled glass needles have been used to apply and measure tensile forces on axons of cultured neurons by pulling on the growth cone (Bernal et al. 2007; Bray 1984; O'Toole et al. 2008; Zheng et al. 1991). These studies have revealed that axonal growth rate increases linearly with an applied load, and that tension is important for neurite development.(Heidemann et al. 1995) Related studies also showed that tension applied to the cell margin can induce neurite formation (Chada et al. 1997) and specify axonal fate.(Lamoureux et al. 2002) A recent extension of towed growth, termed stretch growth (Pfister et al. 2004), has been used to create long tracts of parallel axons, towards a strategy for spinal cord regeneration.(Iwata et al. 2006; Pfister et al. 2006a; Pfister et al. 2006b) Towed and stretch growth are likely to be distinct from normal axonal growth during development in that growth cones are no longer free to stop, turn or retract. Adhesion of the growth cone itself and any other potential adhesion along the axon are also likely to be interrupted during this type of loading.

Biomechanically, axons respond as a viscoelastic solid to imposed tensile or transverse loads (Dennerll et al. 1989). The observed changes in the length of an axon in response to such loads have been explained by traditional spring-dashpot models of viscoelasticity, which assume a continuum of mechanical properties (Fung 1993). More recently, elements of adhesion and tension generated by the growth cone and borne by the cytoskeleton have been integrated into a mathematical model of axonal growth (O'Toole et al.

2008) that incorporates force, viscosity, and adhesions to govern the mode of outgrowth. Each of these models accurately explains the observed bulk behavior of the axon, and has been valuable in multiscale modeling of axonal pathfinding (Aeschlimann and Tettoni 2001). However, it remains to be tested whether such models predict higher-resolution behavior of axons at smaller length scales.

Inside the cell, a well-developed and organized cytoskeleton is responsible for creating and bearing mechanical forces in the cylindrical axon. The adherent growth cone, powered by actin-myosin interactions, generates tension in the axon during advancement. This is opposed by longitudinal compression imposed by the contractile actin-myosin network immediately underneath the plasma membrane in the axon.(Gallo et al. 2002) This compression is also borne by microtubules (MTs), which run through the core of the axon.(Heidemann et al. 1985; Peters and Vaughn 1967; Yamada et al. 1971) Along with their structural role, microtubules serve as the tracks along which a variety of energetic, structural, nutritional, and signaling cargoes are transported bidirectional, through the action of kinesin and dynein motor proteins. (Chevalier-Larsen and Holzbaur 2006; Goldstein and Yang 2000; Hirokawa and Takemura 2004; Schnapp and Reese 1989) Among these transported cargoes are mitochondria, which localize to regions of high-energy use along the axon. (Hollenbeck and Saxton 2005) In addition to the many motile mitochondria, a significant number are stationary, presumably having localized to their site of necessity. These stationary mitochondria

have been described as markers for a slowly moving cytoskeletal framework, (Miller and Sheetz 2006) and may interact with and dock to microtubules, neurofilaments, and cortical actin (Chada and Hollenbeck 2003; Chada and Hollenbeck 2004), (Wagner et al. 2003) (Kang et al. 2008).

Collectively, these studies establish that neurons both produce and respond to tensile forces. While several key structural elements involved in load-bearing have been identified, the underlying mechanisms controlling the ability of neurons to respond to mechanical changes in their environment are not well understood. Towards the elucidation of these mechanisms, we examined the transmission of extracellular strains into the axonal cytoskeleton. We have developed a “substrate strain” loading regimen, in which cells are cultured on a flexible substrate, which is itself stretched (cf. a similar regimen applied to intervertebral disc fibroblasts (Gilchrist et al. 2007)). This configuration allows unconstrained plasticity of a free growth cone and enables continued adhesion, and thus, transmission of loads, between the substrate and the axon. Using this setup, a moderate strain was imposed upon rat sensory neurons, and cytoskeletal deformation was tracked immediately after stretch and during twenty minutes of subsequent remodeling, by monitoring the position of fluorescently labeled docked mitochondria. Our results reveal the axon as a dynamic and heterogeneous structure, which interacts with the extracellular environment in mechanically complex ways. Specifically, we find that strain and tension are not distributed uniformly along the axon and that at small length scales, the axon behaves as

a series of independent linked regions. Our results suggest a length scale within which cytoskeletal structural elements may be altered to modulate the local biomechanical response of the axon.

Methods and Materials

Stretcher Design:

We implemented a “substrate strain” loading regimen, in which cells were cultured on a flexible substrate, which was itself stretched (Fig. 1A). This configuration allowed unconstrained plasticity of a free growth cone and enabled continued adhesion, and thus, transmission of loads, between the substrate and the axon. Silicone sheets (SMI, Saginaw, MI) were fixed between two clamps bolted to a removable base plate. In control experiments without cells, deformation in the imaging region was confirmed to be repeatable, accurate, and homogenous at the μm length-scale, based on the imaging of fluorescent beads 200nm in diameter (Invitrogen, Carlsbad, CA) and ink markers on the silicone with both 100x/1.4 and 40x/0.95 oil immersion microscope objectives. Cells were cultured upright on the silicone but the short focal distance of oil immersion objectives required that the cells be inverted and suspended above a glass bottomed imaging window in a custom-designed chamber to perform live cell microscopy (Fig. 1B). Neurons exposed to long term (15 hours) inversion showed no significant differences in growth dynamics and behavior compared to upright neurons.(Shah et al. 2009) Linear translation stages (Newport Corporation, Irvine, CA) mounted on

either side of the chamber and attached to each clamp allowed the silicone sheet to be appropriately positioned above the coverslip. Stretch was applied in μm increments via a third translation stage.

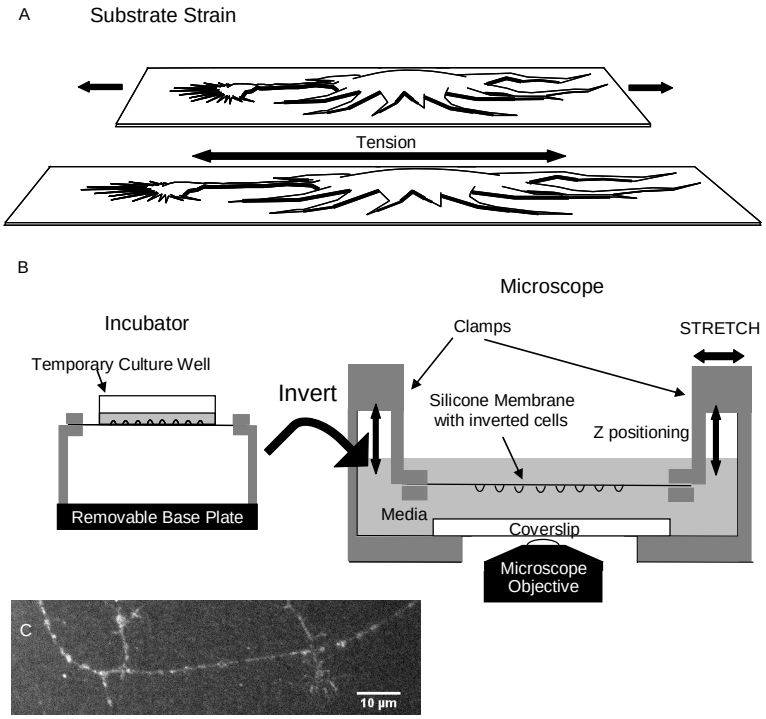

Fig. 1: (A, B) Diagram of loading regimen. Cells were grown on flexible silicone stretched between two fixed clamps and inverted into a glass bottomed imaging dish. Stretch is applied via linear translation stages and results in uniform strain in the silicone. Deformations in the silicone are transferred into the cell, presumably through adhesive sites. (C) Axon of a sensory Neuron stained for talin, a focal adhesion protein, showing the distibution of adhesive sites along its length.

Cell Culture:

Dorsal Root Ganglia (DRG) were isolated from the entire spinal column of 2-6 day old Sprague-dawley rats and maintained in ice cold F-10 supplemented with gentomycin. They were then incubated with 2.5mg/ml collagenase II (Roche, Basel, Switzerland) for 30 minutes at 37^{o}C, triturated and pelleted at 76xg for 5 minutes. Cells were then resuspended in growth

media (10% Horse Serum in F-10, with 1% pen/strep,1% L-glutamine, 50 ng/ml NGF 7-S and 2% B-27), seeded onto laminin coated silicone at a density of 100,000 to 250,000 cells/ml. and incubated at 37^0C and 5% CO_2 for 16-20 hours. To promote axon-enriched imaging regions, a temporary culture well was created in the middle of the membrane during cell seeding and initial cell body adhesion. Animal work has been approved by the IACUC at the University of Maryland.

Fluorescent Labeling of Mitochondria:

Dissociated DRG cultures were incubated with 1:10,000 dilution of mitochondrial dye, MitoTracker green (Invitrogen, Carlsbad, CA) for 2 minutes at 37°C and then allowed to recover in normal growth media for 1-3 hours before being imaged (modified from (Miller and Sheetz 2006)).

Fluorescence Microscopy:

Imaging was performed on an inverted TE-2000E microscope (Nikon, Melville, NY) outfitted with a LumenPRO2000 (Prior Scientific, Rockland, MA) illumination system and Chroma filters (Bellows Falls, VT. EPI: 488nm, Emission 530nm). Additionally, a custom built chamber (Precision Plastics, Beltsville, MD) maintained optimal temperature, humidity and CO_2 levels during imaging. Exposure time was limited to 200-300ms per image. Axons were chosen for analysis which were roughly oriented in the direction of the applied strain ($\pm 15^o$) and were alone and in a non- growing state. 3 paired (DIC and fluorescence) images were taken of the unstretched (0% strain) cells with a 30 second lapse between each image. These images were used

to confirm that mitochondria used to calculate strain were stationary. The cells were then exposed to a 10% strain applied at a rate of 0.03%/sec-0.04%/sec, after which 3 more paired images were captured. This strain rate falls on the high end of rates reported in the literature for long term growth of axons (0.012%/sec - 0.04%/sec). (Pfister et al. 2004; Smith et al. 2001) Similarly, 10% strain lies at the high end of deformations for which functional deficits are reversible (Wall et al. 1991; Wall et al. 1992). A subset of stretched cells were then imaged over the course of 20 minutes with paired images captured every 45 seconds to assess longer term changes in the distribution of mitochondria after the application of strain.

Image Analysis:

All image analysis was performed in ImageJ (NIH, Bethesda, MD) or MATLAB (The MathWorks, Natick, MA). Only those mitochondria which were "stationary," i.e. those not actively transported during loading were analyzed. The signatures of slowly moving or fast-transported mitochondria are different from stationary mitochondria (Miller and Sheetz 2004; Miller and Sheetz 2006), providing additional confidence in appropriate identification. Only individual mitochondria that were visible and in the same position relative to other mitochondria in all images were considered. This resulted in 4 - 9 (avg = 6.5) mitochondria being used per axon. The distance between a pair of fluorescently labeled mitochondria was determined for both 0% (unstretched) and 10% applied strain and used to calculate the strain in the intervening space, defined as the change in mitochondrial separation divided by the initial

separation, or $\Delta l/l_o$. For unstretched axons, two sets of three paired DIC/fluorescent pictures were taken four minutes apart (approximately the amount of time it took to stretch the neurons in the stretched group). For both groups, two points were chosen on the outside of the axon in the DIC images that encompassed the region containing the analyzed mitochondria. Strain calculated from these points was considered to be the whole axon strain and was defined as the "expected" strain based on the assumption of a homogenous distribution of strain inside the axon. Coordinates for mitochondrial position were defined based on manual identification of the peak of the intensity profile along the length of individual mitochondria. For stationary mitochondria, this peak moved <2 μm over 20 minutes, despite any minor fluctuations in mitochondrial shape over this time period. Also, repeated measurements of the same mitochondria in sample images by the same individual and by two different individuals yielded an error of <2 μm.

Kymograph Analysis:

To analyze the movement of mitochondria in the axon over time, a custom Matlab program was used to create kymographs from the timelapse movies. To create the kymograph, a line segment of pixel intensities along the axon was produced for each time point. These line segments were then aligned along their leftmost edge to provide a reliable frame of reference in the resulting composite image. The position of each mitochondria was then

manually extracted from these kymographs and used to calculate strain in the intermitochondrial spaces as a function of time.

Correlation Analysis:

If two mitochondria are coupled to each other, then a displacement of one should be reflected in an identical displacement of the other. To test for such coupling, the displacement for each mitochondrion per time step was determined for all time points in each experiment and plotted against the displacement of each other mitochondrion in the axon. This data was fit using linear regression. If two mitochondria were moving in perfect unison this data would all lie along the line y=x, so that the line of best fit would have a slope of 1. The lines y=0 (slope of zero) or x=0 (infinite slope) reflect a complete dissociation of the two mitochondria. Mitochondrial pairs with slopes between 0.65 and 1.35 were considered to be “correlated” with each other, while those with slopes between -0.35 and 0.35 were considered to be “not correlated” with each other. The R^2 value was also determined based on the goodness of fit for the regression line.

Statistical Analysis:

To quantify and compare the variability between the stretched and unstretched data sets, O’Brien’s transformation was performed (O'Brien 1981). Briefly, the data was divided into bins based on the initial length, and

each data point was transformed into its normalized distance from the mean of the bin according to the following formula:

$$u_{as} = \frac{N_a (N_a - 1.5) (Y_{as} - M_a)^2 - 0.5SS_a}{(N_a - 1) (N_a - 2)}, \quad (1)$$

with:

Y_{as}: Original value of datum

u_{as}: Transformed value of datum

N_a: Number of observations of Group *a*

M_a: Mean of Group *a*

SS_a: Sum of the squares of Group *a*: $SS_a = \Sigma_S (Y_{as} - M_a)^2$.

This procedure takes into account the number of data points per bin and transforms each point of the original data set into a new one which effectively represents the variability in the original data. Moreover, the transformation produces a normally distributed population, enabling the use of ANOVA on the transformed data, to formally compare differences in the variability of the original data between bins.

Bin sizes were initially set to 10 μm, but bin sizes of 5 and 8 μm were also used to test whether variability changed depending on bin size. The total bin number was chosen to maintain a similar number of points in each bin, as there are fewer data points at the longer lengths. Each point of the original data set was converted to its O'Brien number during the transformation, so

that the sizes of the original and transformed data sets were equivalent. Sample sizes for each comparison were selected based on a statistical power calculation with alpha = 0.05, beta = 0.8, and variances estimated from the first three experiments for each comparison.

Results

Phase I: Instantaneous response to strain

Strain magnitude varies along the length of the axon

Dissociated DRG neurons were seeded on a silicone substrate, loaded into a cell stretching device, and imaged using DIC and wide-field fluorescence at 0% (unstretched) and 10% substrate strain. Images and analysis from example stretched and unstretched axons are shown in Fig. 2 A – F. The distance between consecutive pairs of stationary mitochondria was used to calculate the cytoskeletal strain in the axon. Surprisingly, the magnitude of strain varied dramatically along the length of both unstretched and stretched axons (Fig. 2G, H - *diamonds*). Strain in the region between one pair of mitochondria was also different from strain in the region between its flanking neighbors, often in both the sign as well as the magnitude (Fig. 2G, H – *triangles*). For data combined from all axons, variability in strain was higher for stretched axons than unstretched axons (Table 1), suggesting that after stretch, the underlying heterogeneity in strain along the axon was increased. Interestingly, in unstretched axons there was ongoing adjustment in the position of stationary mitochondria, and thus the axonal cytoskeleton

over the course of 4 minutes. Comparison of strain in consecutive pairs of mitochondria in all axons revealed a wide range of differences in strain between neighboring pairs in stretched axons and to a lesser degree, in unstretched axons (Table 1). In addition, only two of the mitochondrial pairs in the unstretched axons and five from the stretched axons showed a similar strain to their neighbors, as determined by a difference of less than 0.01. Collectively, these results reveal heterogeneity in strain along the length of the axon, in both stretched and unstretched axons.

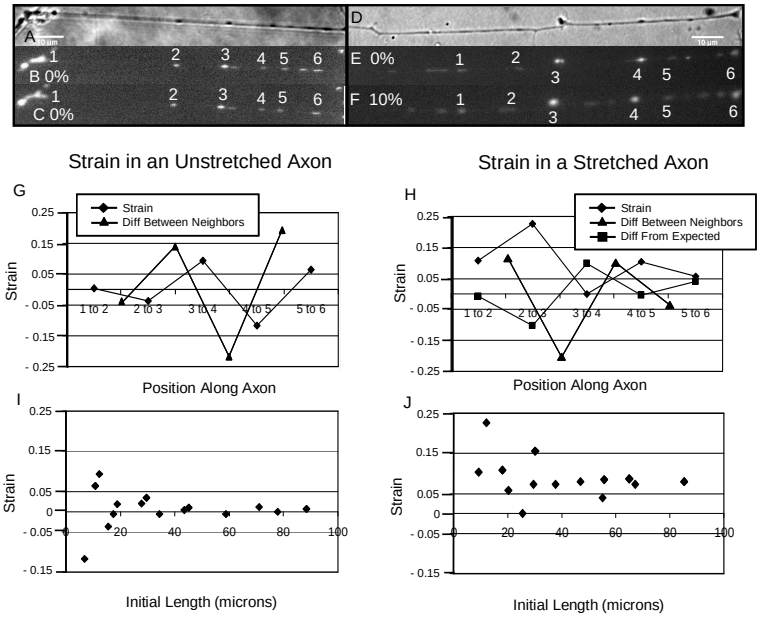

Fig. 2: Instantaneous strain in response to an applied tensile load is heterogeneous. An unstretched axon, under DIC illumination (A) and widefield fluorescence (B) was imaged at 0 (A, B) and 4 minutes (C). Four minutes was the amount of time it took to apply stretch to stretched axons and so it was necessary to quantify the underlying strain in unstretched axons over this same period of time. Stretched axons were imaged before (D, E) and after the application of 10% strain to the substrate (F). Individual mitochondria used for analysis are labeled. (G, H) Heterogeneity in strain along the length of the axon. Plot of calculated strain between consecutive pairs of mitochondria in unstretched (G) and stretched (h) axons shown in a-f. (I, J) Strain as a function of initial length. The calculated strain between all possible pairs of mitochondria was plotted as a function of the initial length of the segment between the pairs for the unstretched (I) and stretched (J) axons shown in A-F.

Table 2. Correlation in Movement of Mitochondria Over Time

	Control	10% Stretch
Average slope	0.47±0.53	0.51±0.45
Average r^2	0.31±0.19	0.22±0.17
Avg r^2 slope = 1	0.46±0.15	0.38±0.14
Percent of data	34.5%	27.1%
Length (μm)	29.5±22.9	39.8±25.3
Avg r^2 slope = 0	0.1±0.08	0.1±0.11
Percent of data	23.3%	41%
Length (μm)	43.0±25.2	51.4±33.7

Actual strain magnitude is different from the expected strain magnitude

To assess the fidelity of transmitting strain from the substrate to the axon, strain in the whole axon was calculated using the DIC images (Table 1). This whole axon strain was then used as the “expected” strain between mitochondrial markers, under the assumption that individual regions of the axon deformed with a uniform strain equal to that of the whole axon. The difference between the expected and actual strains revealed that very few regions of the axon deformed as expected (Fig. 2H – *squares*, Table 1 for all axons), although deviation from this expected strain was greater in stretched axons than in unstretched axons.

Table 1. Strain Along the Length of the Axon

	Description	Strain	Mean +/- STDEV (sample size) (minimum, maximum)
Observed Strain	Strain between mitochondria	0%	0-20 μm: 0.005±0.050 (n=39 pairs) (-0.088, 0.122) 20+ μm: 0.002±0.023 (n= 161 pairs) (-0.079, 0.149) Total: 0.003±0.03 (n=200 pairs) (-0.09, 0.15)
		10%	0-20 μm: 0.081±0.147 (n=124 pairs) (-0.315, 0.462) 20+ μm: 0.064±0.070 (n= 218pairs) (-0.208, 0.256) Total: 0.075±0.098 (n=342 pairs) (-0.32, 0.66)
Difference in Strain between Neighbors	Comparison of strain between one mitochondrial pair and flanking pairs	0%	Total: 0.007±0.07 (n=48 pairs) (-0.16,0.21)
		10%	Total: -0.002±0.21 (n=81 pairs) (-0.61, 0.49)
Whole Axon Strain	Measured based on deformation of axon from DIC images	0%	Total: 0.005±0.01 (n=17 axons) (-0.005, 0.031)
		10%	Total: 0.098±0.065 (n=17 axons) (0.002, 0.206)
Measured vs. Expected Strain	Difference between measured strain and expected strain, calculated based on whole axon strain	0%	0-20 μm: 0.038±0.031 (n=39 pairs) (0.001, 0.113) 20+ μm: 0.015±0.018 (n= 161 pairs) (0.000, 0.126) Total: 0.019±0.023 (n=200 pairs) (0.000, 0.126)
		10%	0-20 μm: 0.107±0.101 (n=124 pairs) (0.002, 0.458) 20+ μm: 0.052±0.060 (n= 218pairs) (0.000, 0.414) Total: 0.073±0.083 (n=342 pairs) (0.000, 0.458)

Variability in strain magnitude is dependent on the initial length of the the axonal region

To compare biomechanical continuity over a range of length scales, strains between all possible mitochondrial pairs in a single axon were calculated (n = 16 for both sample axons in Fig. 2). The strains for each segment were plotted against the initial length of the segment (Fig. 2I, J). Data from multiple experiments were then pooled to evaluate the length dependence of heterogeneity in strain. The measured strain between two mitochondria was plotted as a function of the initial distance separating them in the axon (Fig. 3A, cf. Fig. 2I, J). For both the unstretched and stretched groups, the lines of best fit through the data have slopes close to zero, (-3×10^{-5} and -9×10^{-6}, respectively). Consistent with stretch, however, the Y-intercept of the stretched group is larger than for the unstretched group (0.07 vs. 0.004) and the average strain reflects this as well (0.075 vs. 0.002). There appears to be larger variability in strain in shorter regions of the axon in stretched axons compared to unstretched axons (Fig. 3A). To estimate the length scale at which this phenomenon is significant, we statistically compared differences in the variability of strains using O'Brien's method (Fig. 3B, C). This analysis revealed that variability was significantly greater in stretched axons for lengths less than ~20 μm. Above this length, the variability decreased dramatically, suggesting that local discrepancies, and therefore local material properties, were averaged out over longer length scales. Interestingly, there

also appears to be a length scale of ~10 μm at which this variability is maximized, and below which variability actually decreases again (Fig. 3C). Collectively, these results support a hypothesis that individual regions of the axon exhibit unique material properties in response to tensile loading and suggest that there is a characteristic feature length that contributes to this variability.

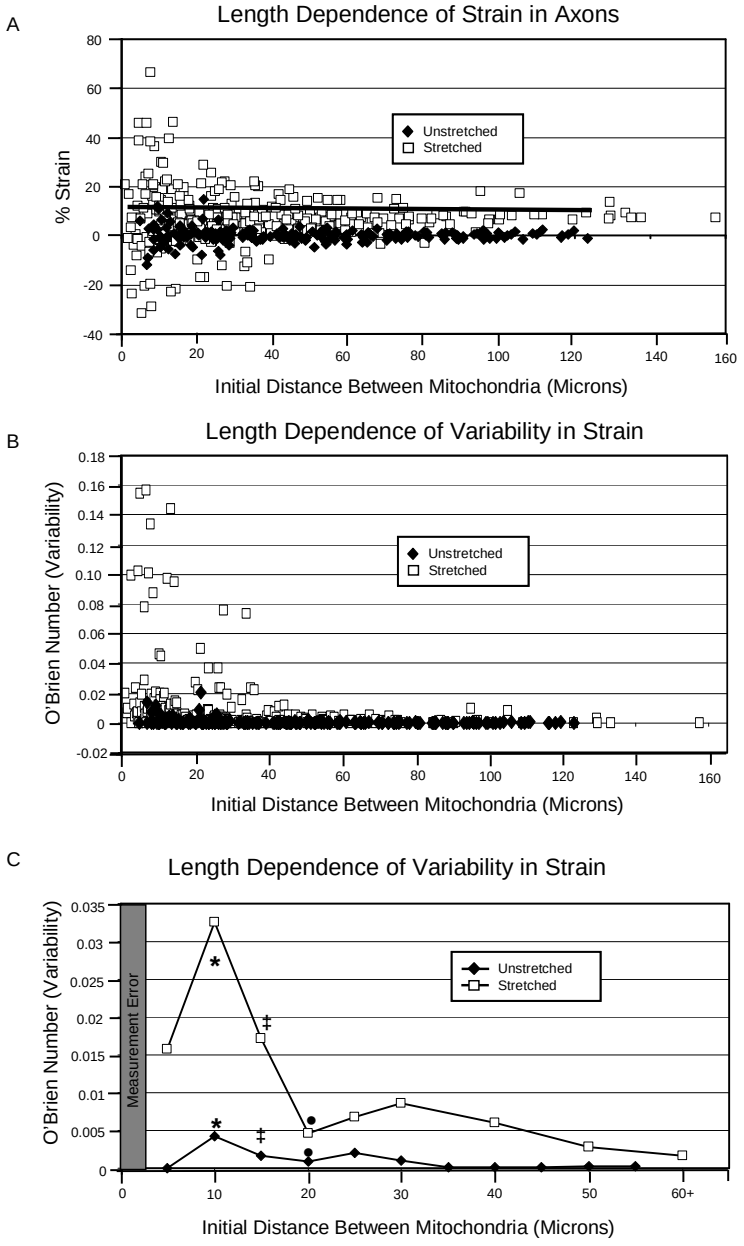

Fig. 3: Strain heterogeneity is increased at small length scales. Data from all instantaneous deflections were pooled and analyzed. (A) Strain in a segment between two mitochondria was plotted as a function of the initial length of the segment (cf. Fig. 2I-J). The average value for strain in stretched axons approaches the expected strain of 10% (0.1 on the Y-axis – heavy black line). (B) Variability of strains in (A) was calculated using O'Brien's method. (C) Variability for five μm bin sizes as quantified by O'Brien's method is greatest between 5 and 10 μm, and decreases dramatically for regions longer than 20 μm in length. While this same trend is noted in unstretched axons, the magnitude of the variability is much smaller. Using a two-tailed Student's T-test, variability in stretched axons was shown to be statistically different from variability in unstretched axons for the bins incorporating data from regions of the axons of initial length, 5-10, 10-15 and 15-20 μm as indicated by *, ‡,and ● respectively. Not enough data was collected from regions of unstretched axons smaller than 5 μm to test for statistically significant differences from stretched axons.

Phases II and III: Long-term remodeling in response to strain

Relaxation in stretched axons is rapid and localized

In a subset of the stretched (n=6) and unstretched (n=6) axons analyzed above, the silicone was held at the stretched length and the positions of stationary mitochondria in the axon were monitored over 20 minutes to assess additional cytoskeletal remodeling (Fig. 8B – schematic of stretch protocol). Sample results for one stretched and one unstretched axon are shown in Fig. 4A – C. Kymographs were used to track mitochondrial position over time (e.g., Fig. 4D, E). To calculate changes in strain during remodeling, the distance between a pair of mitochondria at any given time was compared to the distance between them at the beginning of the time lapse. In all of the stretched axons, no more than two regions of each axon developed large strains shortly after stretch (e.g., arrow, Fig. 4B, E). The deformation in these regions was then maintained, suggesting the realization of a new equilibrium configuration for these segments of the axon. In four of

the stretched axons, these regions attained high strains (30-150%) within a few minutes of stretch and maintained them with fluctuations of <25% for the remainder of the experiment. In the fifth axon, this region of high strain developed more slowly, reaching its peak of 75% approximately 12 minutes after stretch. In the last axon, a region of 75% strain developed quickly after stretch and was maintained for 18 minutes, at which point it became negative very briefly and then increased slowly to 240% over the course of 10 minutes. The latter complex response coincided with increased growth cone activity, the effects of which were likely superposed upon the response to the applied stretch. Other regions of the stretched axons showed relatively small strains (Fig. 4F). An interesting observation in one unstretched axon was consistent with observations in stretched axons; a highly motile cell deflected this axon during the course of the observation period, inducing, as with substrate-stretched axons, one region of high axonal strain (70% magnitude). In the remaining unstretched axons, strain was more uniformly distributed (10%-38%), and all regions of the axon experienced fluctuations in strain over time.

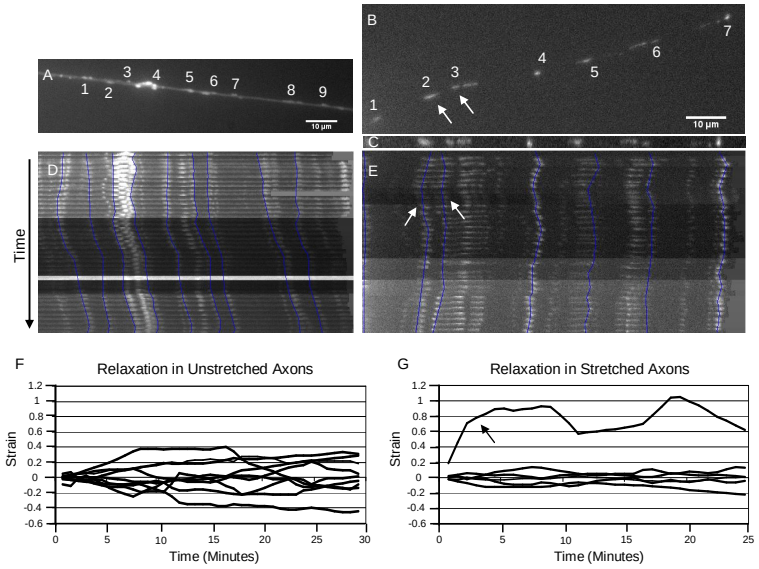

Fig. 4: Regions within stretched axons exhibit continued remodeling following stretch. (A, B) Sample images of unstretched (A) and stretched (B) axons in which mitochondrial position was monitored over 22 minutes. (B) shows the axon before stretch. (C – E) Kymographs were created by tracing along the axon at each time and extracting the position of mitochondria from pixel intensities. For reference, the positions of mitochondria in the axon shown in B before stretch are shown in C. Kymographs for mitochondrial movement in unstretched (D) and stretched (E) axons from (A, B). Strain in regions of unstretched (F) and stretched (G) axons, calculated from the positions of consecutive pairs of mitochondria. A particularly active region of the stretched axons (arrow) exhibited very large strains that were achieved very quickly and then stabilized (G). As with other axons, this region of large strain was between closely spaced mitochondria, while strains in the rest of the axon and in unstretched axons were all of smaller magnitude (F, G).

Strain magnitude and variability during relaxation show a length dependence

The length dependence of strain during relaxation was also analyzed, similar to the analysis performed for instantaneous strain (cf. Fig. 3). On average, including data from all time points, short segments of stretched axons showed larger positive and negative strains compared to regions of unstretched axons (Fig. 5A). Positive strains reflect regions of extension between mitochondria

and negative strains reflect regions of contraction. Based on analysis by O'Brien's method, stretched axons also exhibited greater variability in strain during relaxation at small lengths (Fig. 5B).

Strain magnitude and variability decrease over time after stretch

To test the time dependence of cytoskeletal reorganization, successive four-minute increments within the 20 minute period were analyzed for unstretched and stretched axons. During each four-minute period, strain and variability in strain were calculated from mitochondrial position to assess cytoskeletal mobility over a short time. The average strain during all four-minute time increments showed a length dependent heterogeneity, with strains and variability both larger in stretched axons than in unstretched axons. This suggests that on average, strains changed more rapidly in stretched axons. However, to evaluate the change in heterogeneity over time, three specific increments of four minutes, from 1-4 minutes, from 9-13 minutes and from 18-22 minutes were compared (Fig. 5C, E). In both stretched and unstretched axons, the large strains seen at small lengths decreased over time, but the decrease was much greater and statistically significant in stretched axons compared to that seen in unstretched axons. Moreover, both the magnitude and variability in strain at small lengths in stretched axons decreased over time to levels well below that in unstretched axons (Fig. 5D, F), suggesting that the cytoskeleton of stretched axons has a reduced capability for remodeling following ~20 minutes of relaxation. This result raises the

possibility of a refractory period, during which the ability of the cytoskeleton to respond to mechanical perturbations may be compromised.

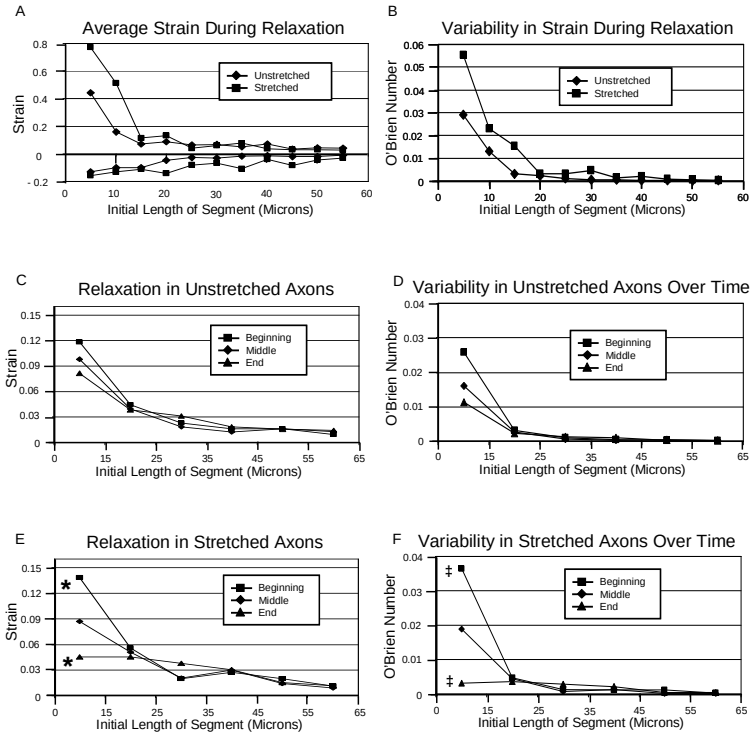

Fig. 5: Remodeling in axons following stretch is length- and time-dependent. As with axons analyzed for instantaneous strain, all pairs of mitochondria in axons were used to calculate strain during the 22 minute experimental period. (A) Average calculated strain for all mitochondrial pairs over all time points. Strain in a segment of an axon between two mitochondria was plotted as a function of the initial length of that segment. Positive and negative strains represent net elongation or contraction of the axon, respectively. (B) Variability in this data, quantified using O'Brien's Method. (C – F) To evaluate the change in strain over time, strain was calculated using the change in position of mitochondria between 1 and 4 minutes of imaging (beginning), between 9 and13 minutes (middle) and between 18 and 22 minutes (end). The average strain magnitude and variability are plotted for unstretched (C, D) and stretched (E, F) axons. A two-tailed student's T-test was used to confirm that strain magnitude and variability decreased by a statistically significant amount in stretched axons over the course of the experiment.

Mitochondrial correlation analysis suggests a less coherent cytoskeletal framework after stretch

It has been hypothesized that mitochondrial movement is coordinated by a coherent microtubule framework (Miller and Sheetz 2006). To investigate

the coherence of the cytoskeleton in response to stretch, pairs of mitochondria were analyzed for correlations in their movement over time in a manner similar to that described in (Miller and Sheetz 2006). The change in the position of one mitochondrion during a time step was plotted as a function of the change in position of a second mitochondrion, and a linear regression was performed on the data for all time points in an experiment (e.g., Fig. 6A, B, corresponding to mitochondria in Fig. 4A – E; cf. (Miller and Sheetz 2006)). Both the slope and the goodness of fit (R^2) for the line of best fit were used to assess the strength of the correlation between the two mitochondria. In both stretched and unstretched axons, best fit lines with a slope close to one (well correlated mitochondrial pair) had higher R^2 values than lines with a slope far from one (poorly correlated mitochondria), suggesting a strong relationship between these independent measures of correlation (Fig. 6C). As shown in Table 2, the average slope of all mitochondrial pairs was roughly the same for both stretched and unstretched axons. A two-tailed Student's t-test confirmed that the two groups were not significantly different. There was also no obvious relationship between the distance between the mitochondrial pairs and the R^2 value or the slope of the regression line. In unstretched axons, however, a larger proportion of the mitochondrial pairs were correlated with each other than in stretched axons where more pairs were uncorrelated (Fig. 6D). Of the mitochondrial pairs which were correlated with each other in unstretched axons, over half were within 25 μm of each other (Fig. 6E). These results suggest that within moderate length scales, there is reduced coherence of the

cytoskeleton in stretched axons compared to unstretched axons. It should be noted, though, that in our system, even within unstretched axons, most regions demonstrate a surprising lack of coherence.

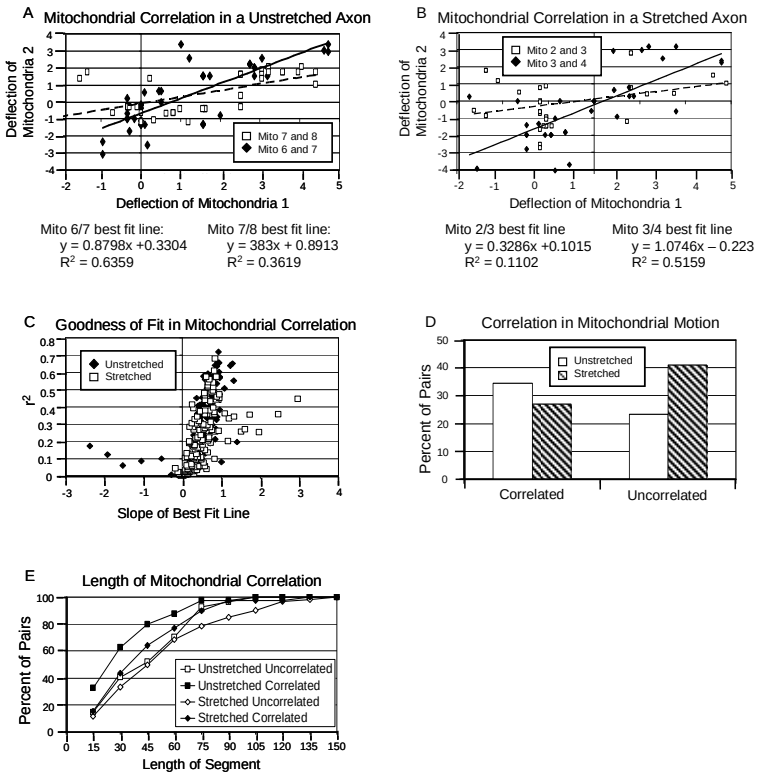

Fig. 6: Stretched axons display reduced cytoskeletal cohesion. (A, B) To assess the possibility of a long range framework coupling mitochondria within the axon, mitochondrial pairs were analyzed for correlation in their movement over time. The deflection of one mitochondrion in an axon was plotted against the deflection of another for each time point, and a linear regression fit to the data. Sample data and lines of best fit are shown for (A*)* mitochondria 6 and 7 (correlated) and 7 and 8 (poorly correlated) in the unstretched axon of Fig. 5 and (B) mitochondria 2 and 3 (poorly correlated) and 3 and 4 (correlated) from the stretched axon in Fig. 4. (C) Correlation analysis of all pairs of mitochondria from all axons reveals that the slope of the best fit lines shows a strong positive relationship with the r^2 values. (D*)* Mitochondria in unstretched axons exhibited more correlated deflections than those in stretched axons, in which many more were uncorrelated. (E) Cumulative histogram of the distance between correlated and uncorrelated mitochondrial pairs for stretched and unstretched axons. Rightward shift in curves corresponding to uncorrelated pairs in stretched axons indicate that fewer mitochondrial pairs showed coordination in their movement in stretched axons than in unstretched axons.

Discussion

In order to investigate the instantaneous response and subsequent remodeling of rat sensory neurons to an applied tensile load, we employed a strategy of deforming a flexible culture substrate. This loading protocol is novel in its application to neuronal lengthening, offering the advantages of unconstrained movement of the growth cone as well as continued adhesion along the axon. We found that strain in the axon in response to loading and during subsequent remodeling was heterogeneously distributed along its length and showed large variability at lengths between 5 and 20 μm compared to unloaded controls. Based on this length dependent heterogeneity, we propose that there is a characteristic length scale over which the mechanical response of an axon to tensile loading is regulated. Coordinated movement of mitochondria tethered to the cytoskeleton further suggests that intracellular structural elements may be responsible for regulating this mechanical response. To the best of our knowledge this is the first study to demonstrate significant regional and temporal heterogeneity in the axon, but this result fits within a growing body of work supporting this unique characteristic of cytomechanics (Heidemann and Wirtz 2004). Overall, our results indicate that the axonal cytoskeleton is a dynamic structure that responds quickly and heterogeneously to an externally applied stretch.

Spatial and temporal heterogeneity in the biomechancial response to tensile loading

While tracking mitochondrial position within the axon, we observed three distinct phases of cytoskeletal response to the stretch protocol (Fig. 5). The first phase, instantaneous response immediately following the initial 10% strain, was characterized by deformation due to the applied load. The second phase, early relaxation, spanned the initial ~14 minute period of sustained strain, and was marked by elevated cytoskeletal mobility. The third phase, late relaxation, was characterized by a dramatic reduction of cytoskeletal mobility, and spanned the period between ~14 and ~22 minutes after the initial strain.

Several results suggest a characteristic length scale within which the cytoskeleton may remodel. Unstretched axons displayed some cytoskeletal mobility, particularly at shorter length scales, but this mobility was small and relatively uniform in magnitude (Fig. 3C; 5C, D). In contrast, measured strain in stretched axons was considerably more heterogeneous during all three phases, with the greatest variability observed in regions of the axon between 5 and 20 μm in initial length (Fig. 3C; 5C, D). Additionally, one to two regions within this length scale in each stretched axon experienced large strains during the early relaxation phase before settling to a new “equilibrium” length (Fig. 4). On the other hand, in regions of the axon longer than about 40 μm, instantaneous strains approached the expected 10%, suggesting that the local variations in strain at small lengths were averaged out over these

greater distances. The average whole axon strain for all stretched axons was slightly less than the expected 10%. This may be due to a number of factors. First, deviations of ±15^{o} in the alignment of axons with the direction of the applied strain were allowed in all experiments (cf. Fig. 4B), resulting in axonal exposure to strains of slightly less than 10%. Additionally, the average could reflect minor extension and retraction of axons in response to stretch. Lastly, this discrepancy may be due to small inefficiencies in the transmission of strain from the substrate to regions within the axon as the result of adhesive slippage or slippage within the layers of the cytoskeleton. Examination of mechanisms underlying this minor but potentially important lack of fidelity in strain transmission, particularly in the context of the small number of local, highly dynamic cytoskeletal regions observed in stretched axons, offers an interesting avenue for future research.

Our analysis of axonal coherence also supports the idea of a characteristic length scale. An intriguing study recently raised the possibility of a coherent microtubule framework, that couples the movement of mitochondria over relatively long distances in the axon (Miller and Sheetz 2006). Though axonal adhesion in our mammalian model (Fig. 1C) is likely to differ from the avian model used previously, we comprehensively examined our data for the possibility of a similar long distance coupling between mitochondria. Even in unstretched axons, only one third of the mitochondrial pairs analyzed showed coordination in their movement over time. While this coordination is not inconsistent with a long distance axonal framework, these

mitochondria tended to be close together and thus support the idea of local regulation of cytoskeletal properties. In stretched axons, mitochondrial movement was less coordinated, suggesting that stretch disrupts any sort of local or global framework that could regulate cell shape or axonal transport.

A sliding filament model of cytoskeletal remodeling

While our results reflect outcomes of biomechanical testing, they have implications for the composition and biological function of the axon. The axonal cytoskeleton is a well-organized polymer scaffold able to bear and produce mechanical loads through a network of filamentous and connecting proteins. Models of axonal biomechanics must be consistent with the material properties of this dynamic cytoskeletal lattice. In developing such a model (Fig. 7, 8), we have considered two characteristics that govern this system. The first is that, given the large persistence lengths and high tensile elastic moduli of cytoskeletal filaments (Gittes et al. 1993; Kojima et al. 1994; Kreplak et al. 2005; Leterrier et al. 1996; Venier et al. 1994; Zeiger and Layton 2008), they most likely retain their structural integrity in response to a tensile load. While some polymerization and de-polymerization may occur, filaments are unlikely to fail following stretch. Consistent with this, then, the second characteristic is that the ancillary proteins that connect or cross-link the filaments are likely to be most affected by an applied load. These connecting proteins may be either static load-bearing cross-links or dynamic force-generating links such as molecular motors. We propose that the

dynamics and mobility of the cytoskeleton will be determined by the changing connectivity and composition of these cross-links. Under load, either from within or without, a filament in the axon will experience some reorganization of its connections to its neighboring filaments. This will expose the filament to new forces and, ultimately, move it to a new equilibrium position. Global axonal dynamics would then reflect the propagation of numerous such events through the rest of the cytoskeleton. Such a “sliding filament” model takes into account the cell biological, biochemical, and biomechanical literature as well as our observations of temporal changes in cytoskeletal mobility, spatial differences in deformation, and the characteristic length scale over which remodeling occurs. We hypothesize that the relative movement of cytoskeletal filaments within the axon mediates the response of an axon to strain, with each of the three phases of remodeling characterized by particular changes in the strength and types of connections between filaments.

The immediate response of the axon to 10% substrate strain constitutes the first phase of remodeling. As the substrate is stretched, networks of filaments in the periphery of the axon deform in the direction of loading, which then necessitates deformation of the coupled filament network deeper within the axon. This pattern of deformation most likely occurs due to the movement of overlapping filaments with respect to each other, rather than to deformation of the filaments themselves and results in a change in the composition and connectivity of the cross-linking and motor proteins associated with the filament network. Local heterogeneity would then be

governed by differences in local material properties (e.g., filament density or connectivity) or boundary conditions (e.g., sites of axonal adhesion). We cannot exclude the possibility that the initial, rapid changes in local material properties or cytoskeletal mobility result from polymerization or depolymerization of individual filaments but these mechanisms are less likely to occur during the relatively short duration of the loading.

Cytoskeletal Mobility During and After Stretch

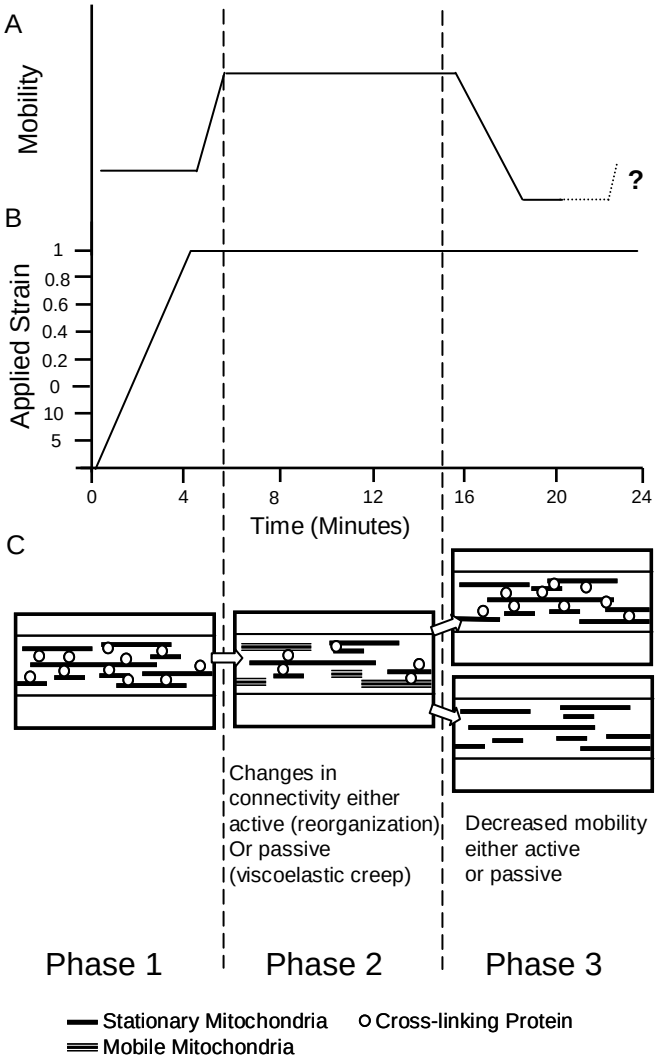

Fig7. Proposed model of cytoskeletal mobility over time. (A) The substrate was stretched to 10% over the course of 4.5 minutes and then held at the stretched length while cytoskeletal position was monitored for 22 minutes. (B) Cytoskeletal mobility showed three distinct phases in response to the applied tensile load. After the initial deformation, cytoskeletal deformation and mobility remained high for approximately 14 minutes, after which it decreased to levels below those seen for unloaded controls. The eventual resolution of this decreased mobility remains to be elucidated. (C) It is unclear what mechanism underlies this behavior but we have suggested that reorganization of the axonal cytoskeleton occurs through sliding of cytoskeletal filaments with respect to one another. In response to an applied load, the connectivity of cross-linking proteins stabilizing the cytoskeleton is changed allowing for increased filament mobility (phase 2). Filament mobility is then dramatically decreased, either through reinforcement or further reduction in crosslinking (phase 3). These changes may occur either through passive or active mechanisms as described in the figure and discussion text.

The second and third phases of the axonal response occur while the substrate strain is maintained at 10%. Increased magnitudes and variability of cytoskeletal mobility during the second phase may reflect passive redistribution of filaments enabled by changes in the density and localization of cross-links (i.e., viscoelastic creep in response to a constant load imposed by the substrate). These changes could result from sheared rigid cross-links or from a sudden reduction in the number of bound motor proteins that had been previously stabilizing the cytoskeletal network. Alternately, enhanced cytoskeletal mobility could reflect active remodeling by means of filament polymerization, targeted redistribution of cross-links, or local regulation of filament transport by molecular motors. In light of the short duration of dramatic remodeling, *de novo* protein synthesis within the axon seems less likely but cannot be entirely discounted.

The third phase of axonal remodeling revealed a surprising decrease in cytoskeletal mobility to levels below that of unstretched controls. This refractory period could be due to depleted metabolic or force-production

capabilities required for reorganization. Under the first scenario, ATP-dependent processes such as transport or polymerization may be temporarily blocked (Sakama et al. 2003; Takeuchi et al. 2005); for the latter, the reduced number of bound (or activated) motor proteins may lack the ability to translocate filaments through a viscous axoplasm (Hill et al. 2004; Holzwarth et al. 2002; Mallik et al. 2004), serving to effectively decouple filaments from the global structural network(Shah et al. 2002). Conversely, it is conceivable that the cell could have reinforced its cytoskeleton through an augmentation of cross-link density in order to limit further plasticity or possible injury (Barash et al. 2002; Shah et al. 2002).

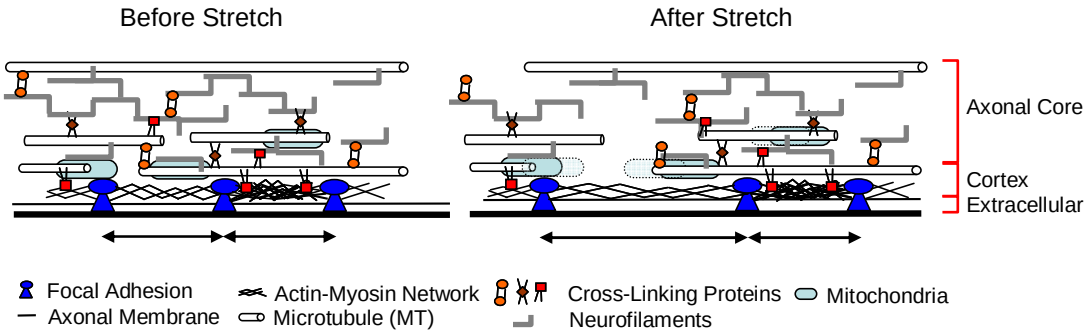

Fig. 8: Biological components and organization of the axonal cytoskeleton. The axonal cytoskeleton is composed of a cortical region containing a contractile actin-myosin network to which adhesion sites are anchored. Initial deformation in the substrate is likely transmitted through these adhesion sites into the actin cortex and then propagated into the axonal core. The core is composed of microtubules and neurofilaments connected by “rigid” and “dynamic” cross-linking proteins.

Potential cytoskeletal contributors to remodeling

Considerable biological and biochemical literature suggests that filaments and crosslinks within our generalized siding filament model may be mapped to specific proteins (Fig. 8). Mitochondria are transported along

axonal microtubules by kinesin and dynein motors, and transition to short-range movement upon actin filaments via myosin motors prior to docking (Morris and Hollenbeck 1995; Ruthel and Hollenbeck 2003). A sub-population of mitochondria is also anchored to neurofilaments (Hollenbeck 1996; Leterrier et al. 1996; Wagner et al. 2003), which are the most abundant cytoskeletal components in the neuron (Lee and Cleveland 1996). Additionally, microtubules, microfilaments, and intermediate filaments have each been reported to interact with each other through a variety of intermediaries detailed below. Consequently, mitochondrial deflection is likely to represent the deformation of any or all of these cytoskeletal components. Despite this complexity, our observations in combination with previous studies allow us to raise testable hypotheses regarding the transmission of strain from a substrate into the axon.

The initial propagation of strain from the substrate into the cell may be attributed to focal adhesions that we observe along the length of the axon. Actin filaments in the axonal cortex, cross-linked by myosin motors, are anchored to these sites of adhesion. (Burridge and Fath 1989; Burridge et al. 1987) Heterogeneity of strain at this interface may be due either to an uneven distribution of adhesion sites along the axon or to local variability in the density, and thus contractility, of the actin-myosin network. Attachment of focal adhesions to the extracellular matrix also induces actin recruitment and polymerization, and increases myosin activity (Hildebrand et al. 1996; Ridley and Hall 1992). Consequently, adhesion and contractility may be coupled,

with regions of enhanced contractility more likely to resist an applied tensile load.

From actin-myosin networks, strain would then be transmitted to microtubules and neurofilaments within the axonal core. Actin has been reported to associate with neuronal microtubules through dynein motors (Ahmad et al. 2000; Baas et al. 2006; Hasaka et al. 2004; Pfister 1999) and through a variety of cross-linking proteins such as doublecortin, MACF, MAP1A/B, shortstop, or pod-1 (the latter two in *Drosophila*) (Applewhite et al.; Fujii et al. 1993; Leung et al. 1999; Rothenberg et al. 2003; Sanchez-Soriano et al. 2009; Tint et al. 2009; Tsukada et al. 2005). Additionally, the actin cytoskeletal network interacts with neurofilaments, directly or through spectrin and myosin (Frappier et al. 1991; Hao et al. 1997; Jung et al. 2004; Macioce et al. 1999; Rao et al. 2002). Within the core of the axon, microtubules associate with other microtubules and with neurofilaments through dynein and kinesin motors (Ahmad et al. 1998; He et al. 2005; Hirokawa 1982; Motil et al. 2006; Myers and Baas 2007; Nadar et al. 2008; Pfister 1999; Shea 2000), while neurofilaments form cross-bridges with each other through extended sidearm domains (Garcia et al. 2003; Hirokawa 1982; Rao et al. 2002).

Our observed length scales of axonal remodeling suggest that there are small dynamic regions of heterogeneous material properties in the axon. In the context of the proposed sliding filament model, the length of a given filament is of critical importance. Filament length not only dictates filament mobility through the viscous axoplasm, but is also likely to influence crosslink

or motor number; shorter filaments are likely to be more mobile, as they will experience less drag, and are less likely to be interconnected into a broader scaffold. This logic is consistent with previously reported observations of microtubule and neurofilament mobility. Microtubules vary in length with some ranging up to hundreds of μm in mature axons *in vivo* (Burton 1987), but primarily shorter microtubules have been reported to be more mobile (Ahmad et al. 1998; Vallee and Bloom 1991; Yu and Baas 1994). These shorter microtubules are also believed to be of central importance to axonal growth and branching (Myers et al. 2006; Yu et al. 1994), and so may be reasonable candidates for influencing remodeling within the axon. Similarly, neurofilaments form a dense, interconnected network in mature regions of the axon (Barry et al. 2007; Garcia et al. 2003; Hirokawa 1982; Lee and Cleveland 1996; Leterrier and Eyer 1987; Leterrier et al. 1996; Rammensee et al. 2007), but filaments observed to translocate along axons appear to be shorter in length (Shea 2000; Wang and Brown 2001; Yabe et al. 1999).

Conclusions

Collectively, our work suggests a conceptual model for the response of the axonal cytoskeleton to mechanical loading. We also provide several testable hypotheses for identifying specific cytoskeletal elements involved in such a model, including the interesting possibility of a role for motor proteins in modulating the local mobility and organization of cytoskeletal filaments within the axon. These hypotheses may be readily dissected through a combination of pharmacological, genetic, and fluorescent labeling methods.

Previous work examining the effect of mechanical forces on neurite development and growth rate suggests that the axon behaves as a viscoelastic material with homogenous material properties. We have, in contrast, demonstrated that at small length scales, the axon exhibits significant localized heterogeneity in its response to a uniform load. If this heterogeneity is coupled to local regulation of axonal processes, then an applied load could cause a dramatic shift in both local and global functioning of the axon. In particular, these variations may serve as mechanical signals that play a role in local regulation of axonal processes such as adhesion, transport, cytoskeletal reorganization or protein recruitment and docking to the cytoskeleton. Identification of mechanisms regulating these processes would be of great benefit for understanding neuronal development as well as designing more effective strategies for neuroregeneration and neuroprotection.

Chapter 5: Conclusions and future work

Chapter Summaries:

Summary: Chapter 2

In this chapter we developed an algorithm that automates the generation of kymographs from time lapse movies of the axons of cultured neurons. Over long capture times, axons can change orientation and geometry within the field of view, and these changes confound traditional methods of building a kymograph. Our algorithm addressed these issues through a combination of robust axon alignment and detection strategies. We demonstrated that this algorithm increased the accuracy of kymographs and reduced the user time and effort in building them. Additionally, we showed that our algorithm is resistant to noise in images as well as to error in user defined parameters. This offers a new and powerful tool for use in the analysis of axonal transport and should serve as a foundation upon which more sophisticated image processing applications can be built towards answering a myriad of other questions related to intracellular trafficking and signaling.

Summary: Chapter 3

The data presented in this chapter provide clear evidence for a novel mode of transport for actin densities in the axon. We showed that short bursts of small but significant movement are mediated by both actin and

microtubules to produce a net anterograde displacement of actin densities at speeds commensurate with slow component transport rates. These actin densities are filamentous in nature, and their emergence appears to be due to bundling and polymerization of filaments, rather than de novo translation. They are moved bidirectionally by myosin motors, presumably walking along the actin cortex, and our results suggest the possibility of a directional bias in the orientation of actin filaments there. A significant fraction of the anterograde movement of these actin densities appears to be as passive cargoes piggy-backing on microtubules being pushed down the axon by dynein. Intriguingly, the actin and microtubule cytoskeletons each seem to serve as a brake on movement mediated by the other. Finally, these densities seem to have a number of biological functions, as they are associated with filopodial protrusion and co-localize with mitochondria and the focal adhesion complex protein talin. This work represents a major step forward in elucidating a novel mechanism for the transport of actin and has broad implications for the movement of other soluble cargoes in the axon. Additionally, our work suggests a more prominent role for the dynamic reorganization of actin in regulating the axon's internal environment.

Summary: Chapter 4

In chapter 4 the effect of an applied tensile load on the axonal cytoskeleton was examined. Previous work investigating the effect of mechanical forces on neurite development and growth rate suggests that the

axon behaves as a viscoelastic material with homogenous material properties. In this chapter, however, we demonstrated that at small length scales, the axon exhibits significant localized heterogeneity in its response to a uniform load. This is true for both the immediate response to an applied stretch as well as to changes in the cytoskeleton over time after stretch. Furthermore, our results suggest a conceptual model for the response of the axonal cytoskeleton to mechanical loading and we provided several testable hypotheses for identifying specific cytoskeletal elements involved in such a model. Finally, if this heterogeneity is coupled to local regulation of axonal processes, then an applied load could cause a dramatic shift in both local and global functioning of the axon. In particular, these variations may serve as mechanical signals that play a role in local regulation of axonal processes such as adhesion, transport, cytoskeletal reorganization or protein recruitment and docking to the cytoskeleton. Identification of mechanisms regulating these processes would be of great benefit for understanding neuronal development as well as designing more effective strategies for neuroregeneration and neuroprotection.

Overall Conclusions:

An aim of this work was to expand on previous studies which have demonstrated numerous effects of mechanical loading on axonal physiology and morphology. In particular, we wanted to understand the role of the cytoskeleton during normal axonal outgrowth as well as in the response of the

axon to an applied tensile load. In this dissertation we have described our discovery of a novel mechanism for the axonal transport of actin that depends on an intimate and dynamic connection between the actin and microtubule cytoskeletons. Additionally, we have shown that the axon behaves as a series of linked independent functional units in response to stretch, rather than as a viscoelastic continuum. Each of these studies contributes significantly to the field of knowledge, but taken together, they represent a major step forward in neuronal cell biology and our understanding of the interactions within and between the actin and microtubule cytoskeletons in the axon. Further, this work provides a framework for future efforts to understand axonal physiology during growth and development and for future therapeutic approaches to regeneration of peripheral nerves.

These studies also represent the fundamental importance of technology development to the future of basic research. Only because of the enormous amount of data analyzed in chapter 3 were we able to make new observations about slow axonal transport. Previously it was not feasible to collect and analyze data with the temporal resolution and breadth as we have done. By automating the processing of time lapse movies using our algorithm and by rigorously quantifying the movement of actin densities, we were able to support a truly novel model of transport in the axon. Additionally, the development of a cell stretching device that allowed the imaging of live fluorescently labeled cells at high magnification allowed us to rigorously quantify changes in the position of fiduciary cytoskeletal markers and produce

the first evidence that the axon does not behave as a viscoelastic continuum in its response to stretch.

Broadly, our results demonstrate that the axon is not simply a passive conduit connecting the cell body to the synapse, but rather is a dynamic cellular antenna that must navigate a complex mechanical world. Our results provide an outline for the continued study of the mechanisms by which the axon exerts mechanical forces on the environment during growth, and how mechanical changes in that extracellular environment are interpreted by the axon. We have established 1) that an applied tensile load is transmitted into the axon through adhesion, 2) that polymerized actin densities vary in their lifetime and mobility, 3) interact dynamically with microtubules, 4) can be co-localized with focal adhesions, and 5) are distributed heterogeneously along the axon. These results suggest that the actin cytoskeleton is dynamic, heterogeneous and integrated with both the intracellular cytoskeleton and the extracellular substrate. For all of these reasons, we suggest it as a primary mechano-sensing apparatus, which transmits substrate strain into the axon. Our hypothesis for future work is that changes in the connectivity within and between the actin and microtubule arrays are likely to signal the dynamic reorganization which we observed in chapter 4. Specifically we think that an extracellular strain will be transmitted through focal adhesions into the actin cortex. This will result in changes to the integrity and contractility of that network, but will also affect changes in the organization of the microtubule array in the core of the axon.

Future efforts should focus on performing an analysis of the connectivity within the actin cortex and the microtubule arrays in the core of the axon, as well as between actin and microtubules during and after loading. The technology to carry out these studies and analyze the results has been developed, as described in this work. Experimentally, individual cytoskeletal components will need to be fluorescently labeled in the axons which will subsequently be stretched. Ideally, multiple components will each be labeled in a different color so that the displacements of each can be monitored over time in the same axon. This will allow the calculation of local displacement for each component, but also will allow the quantification of the transmission of strain from the substrate, to adhesion sites, into the actin cortex and finally into the microtubule core of the axon. What remains is to identify appropriate fluorescent labels, and in fact a number of commercially available dyes exist and a number of researchers have developed fluorescently tagged fusion proteins for cytoskeletal components. These next steps will provide unrivaled insight into axonal physiology, growth, mechanical interaction with the extracellular environment and will complete the foundational work needed to develop truly extraordinary neuroregenerative therapeutic capabilities.

Appendices

Supplementary figures for chapter 3

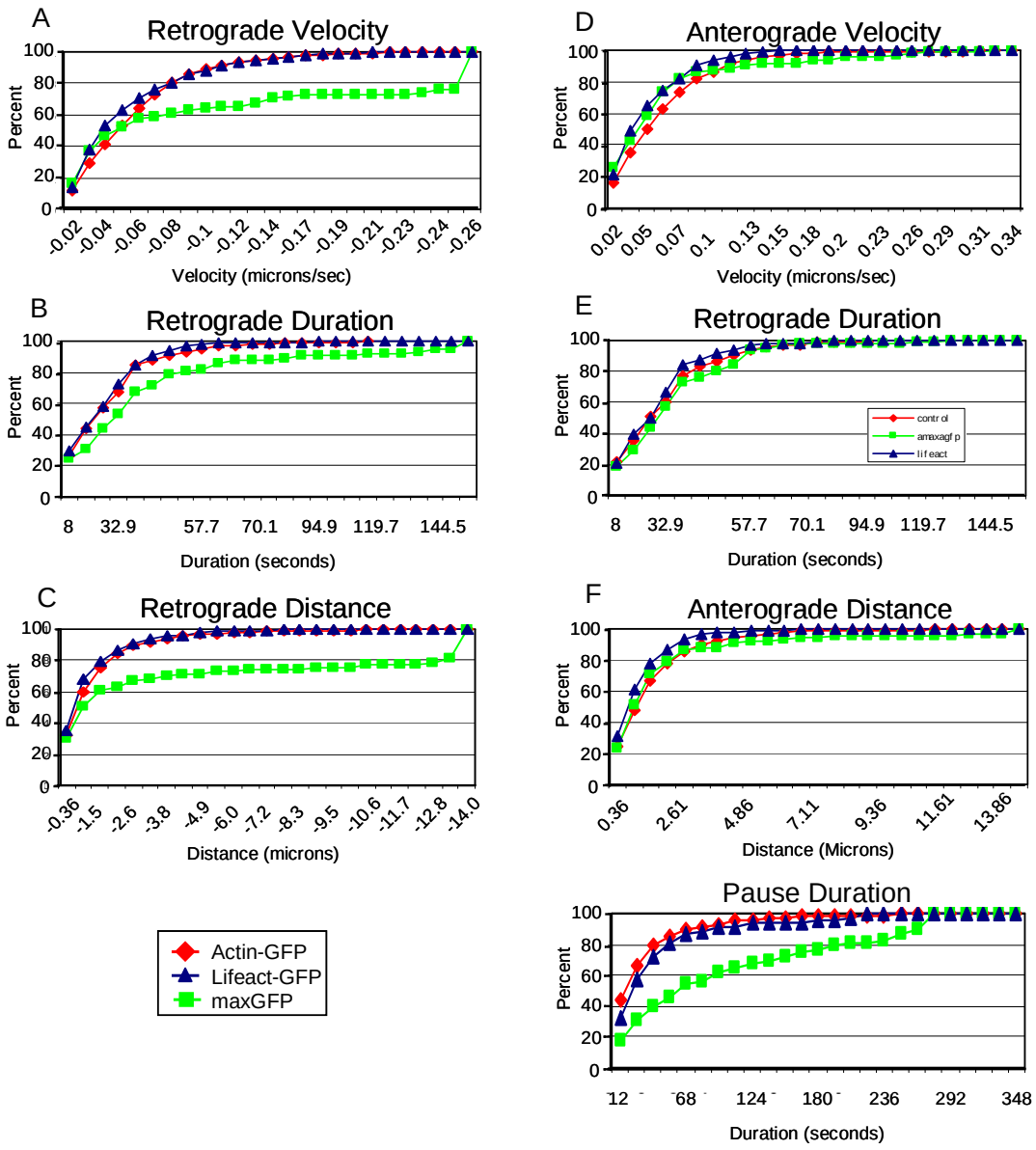

Figure S1: Cumulative histograms showing the distribution of transport parameters for particles in Lifeact, maxGFP and GFP-actin expressing axons. The velocity, duration, and distance traveled by a particle were measured in axons expressing one of the three fluorescent constructs. Because the distributions were broad and non-

normal, a Kolmogorov Smirnov test was used to test for significant differences between groups. The results of this analysis are summarized in the tables of figure 2.

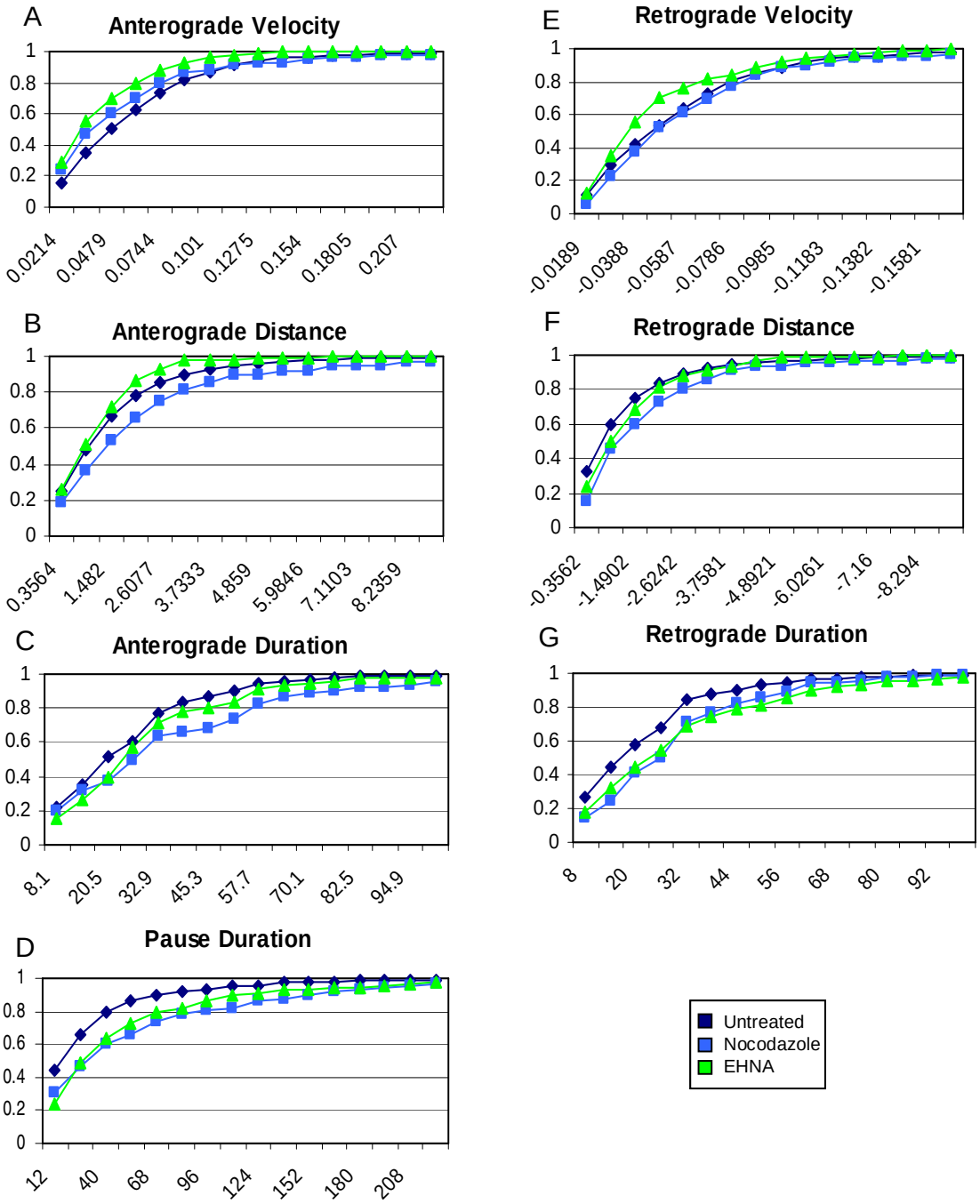

Figure S2: Cumulative histograms showing the distribution of transport parameters for particles in axons treated with either nocodazole or EHNA. The velocity, duration, and distance traveled by a particle were measured in axons expressing GFP-actin. Statistically significant differences are summarized in the table of Figure 4.

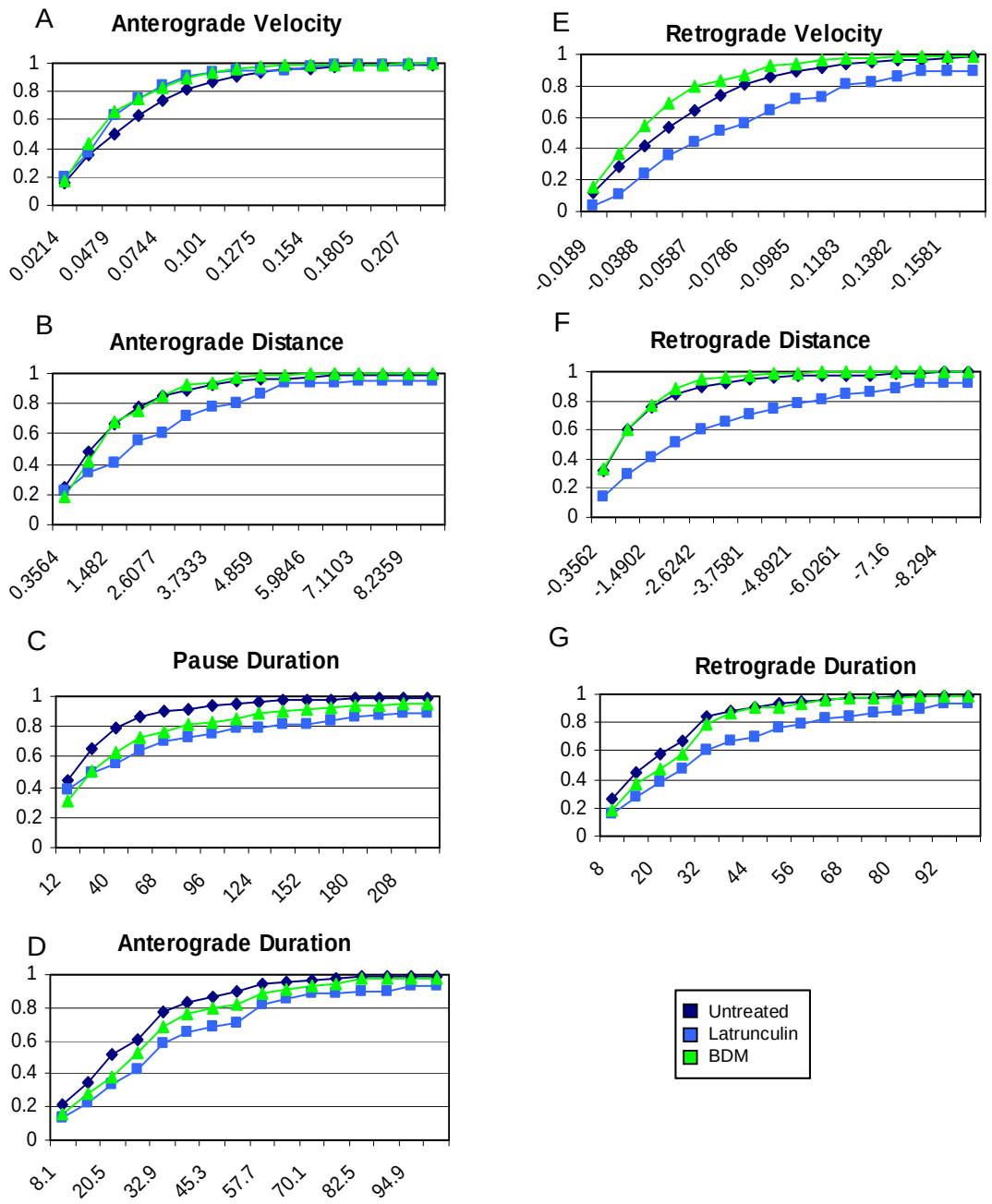

Figure S3: Cumulative histograms showing the distribution of transport parameters for particles in axons treated with either latrunculin or BDM. The velocity, duration, and distance traveled by a particle were measured in axons expressing GFP-actin. Statistically significant differences are summarized in the table of Figure 4.

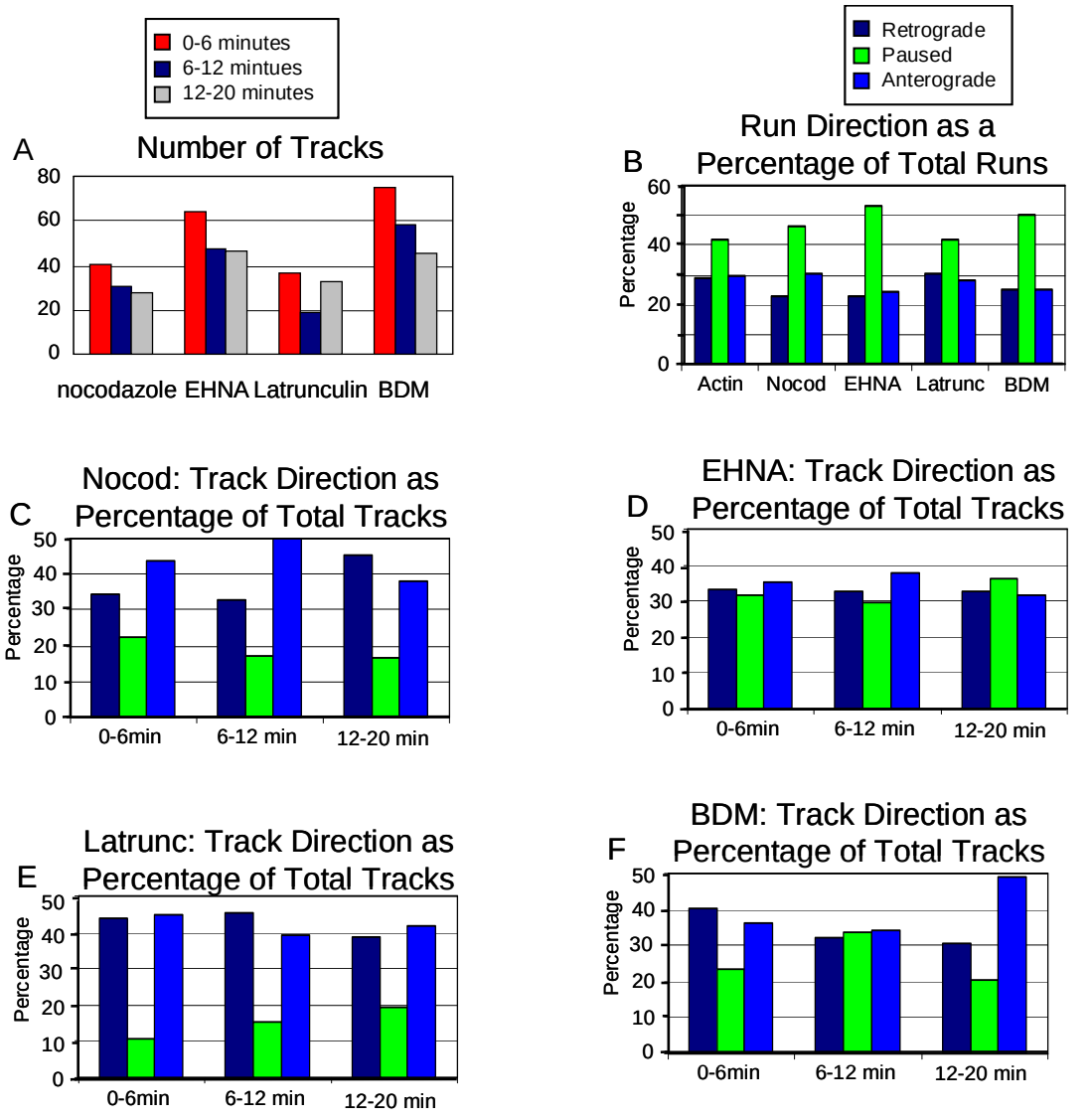

Figure S4: Changes particle direction over time. (A) All of the drugs decreased the total number of tracks over time, although latrunculin showed a slight recovery during the last 12-20 minutes of imaging. (B) Run direction as a percentage of the total number of runs in a given time-lapse calculated for the middle time phase (6-12 minutes of drug exposure). (C-F) Track direction as a percentage of the total number of tracks for each of the three temporal phases of drug exposure.

Supplementary tables for chapter 3:

Table S1: Comparison of number and direction of tracks for all groups.

	Number of Tracks	New Tracks	Retrograde Tracks	Paused Tracks	Anterograde Tracks	Runs per Track
Actin-GFP	60.81±31.26	47.81±27.45	21.06±10.05	15.313±10.812	24.44±15.31	2.33±0.63
Lifeact-GFP	60.08±19.77	46.4±18.29	19.04±8.52	22.08±10.36	18.96±8.39	2±0.34
GFP	24.63±15.02	13.25±10.9	8±4.72	8.44±5.99	8.19±7.19	1.75±0.57
Nocodazole 6 min	40.56±18.05	34.78±15.83	13.89±5.73	9±5.1	17.67±9.67	1.91±0.35
Nocodazole 12 min	30.78±11.8	27.67±11.67	10.11±6.49	5.33±5.07	15.33±5.45	1.98±0.53
Nocodazole 20 min	28.13±17.6	24.63±16.34	12.75±10.25	4.63±3.89	10.75±6.34	2.23±0.51
EHNA 6 min	63.8±19.54	56.6±19.39	21.3±6.55	20.2±10.36	22.3±10.81	1.65±0.24
EHNA 12 min	47±17.31	41.7±15.54	15.3±5.1	13.9±7.64	17.8±7.27	1.66±0.29
EHNA 20 min	46.4±16.37	41.7±15.61	15.1±5.74	16.7±6.82	14.6±7.6	1.79±0.36
Latrunculin 6 min	36.67±9.07	29.67±7.15	16.17±5.12	4±3.41	16.5±3.73	2.21±0.95
Latrunculin 12 min	18.67±14.9	15.83±13.96	8.5±7.06	2.83±3.76	7.33±5.39	2.29±0.48
Latrunculin 20 min	32.67±15.14	26.33±16.17	12.67±4.73	6.33±3.21	13.67±7.37	2.48±0.18
BDM 6 min	75.13±40.13	63.5±31.23	30.38±15.65	17.63±11.46	27.13±15.54	2.28±0.61
BDM 12 min	58.14±30.75	48.57±27.3	18.57±10.74	19.71±14.55	19.86±9.82	2.12±0.45
BDM 20 min	45.5±24.23	47.77±16.15	14±8.83	9.25±7.93	22.25±9.43	2.4±0.79

Table S2: Comparison of number and direction of runs for all groups.

	Number Retrograde Runs	Number Paused Runs	Number Anterograde Runs
Actin-GFP	38.63±17.46	56.31±26.24	39.31±20.72
Lifeact-GFP	24.24±10.79	52.16±16.87	23.6±13.34
GFP	10.5±6.91	26.31±16.28	7.69±8.37
Nocodazole 6 min	19.89±12.24	37.78±17.53	22.56±16.65
Nocodazole 12 min	14±8.15	28.33±11.55	18.56±13.93
Nocodazole 22 min	18.5±12.68	28.25±20.69	16.75±12.61
EHNA 6 min	23.8±9.58	56.1±16.64	24.8±11.31
EHNA 12 min	17.5±6.65	40.9±16.38	18.8±8.57
EHNA 22 min	19.4±7.44	44.7±15.59	18±8.76
Latrunculin 6 min	23±12.79	32.67±6.28	22.67±11.99
Latrunculin 12 min	12.67±11.11	17.33±14.72	11.83±11.25
Latrunculin 22 min	20.33±5.13	34.67±18.72	24.67±7.64
BDM 6 min	51.63±28.03	83.63±60.51	42.13±27.55
BDM 12 min	31.71±19.98	62.57±38.66	31.29±19.35
BDM 22 min	28.25±27.93	54.25±40.19	37.25±26.34

Bibliography

Abe I, Ochiai N, Ichimura H, Tsujino A, Sun J, Hara Y. 2004. Internodes can nearly double in length with gradual elongation of the adult rat sciatic nerve. J Orthop Res 22(3):571-7.

Abe I, Tsujino A, Hara Y, Ichimura H, Ochiai N. 2002. Paranodal demyelination by gradual nerve stretch can be repaired by elongation of internodes. Acta Neuropathol (Berl) 104(5):505-12.

Abe I, Tsujino A, Hara Y, Ochiai N. 2003. Effect of the rate of prestretching a peripheral nerve on regeneration potential after transection and repair. J Orthop Sci 8(5):693-9.

Aeschlimann M, Tettoni L. 2001. Biophysical model of axonal pathfinding. Neurocomputing 38-40:87-92.

Ahmad FJ, Echeverri CJ, Vallee RB, Baas PW. 1998. Cytoplasmic dynein and dynactin are required for the transport of microtubules into the axon. J Cell Biol 140(2):391-401.

Ahmad FJ, He Y, Myers KA, Hasaka TP, Francis F, Black MM, Baas PW. 2006. Effects of dynactin disruption and dynein depletion on axonal microtubules. Traffic 7(5):524-37.

Ahmad FJ, Hughey J, Wittmann T, Hyman A, Greaser M, Baas PW. 2000. Motor proteins regulate force interactions between microtubules and microfilaments in the axon. Nat Cell Biol 2(5):276-80.

Allen RD, Metuzals J, Tasaki I, Brady ST, Gilbert SP. 1982. Fast axonal transport in squid giant axon. Science 218(4577):1127-1129.

Allison DW, Gelfand VI, Spector I, Craig AM. 1998. Role of Actin in Anchoring Postsynaptic Receptors in Cultured Hippocampal Neurons: Differential Attachment of NMDA versus AMPA Receptors. J. Neurosci. 18(7):2423-2436.

Alvarez J, Giuditta A, Koenig E. 2000. Protein synthesis in axons and terminals: significance for maintenance, plasticity and regulation of phenotype: With a critique of slow transport theory. Progress in Neurobiology 62(1):1-62.

Anuta PE. 1970. Spatial Registration of Multispectral and Multitemporal Digital Imagery Using Fast Fourier Transform Techniques. Geoscience Electronics, IEEE Transactions on 8(4):353-368.

Applewhite DA, Grode KD, Keller D, Zadeh AD, Slep KC, Rogers SL. 2010. The Spectraplakin Short Stop Is an Actin-Microtubule Cross-Linker That Contributes to Organization of the Microtubule Network. Mol. Biol. Cell 21(10):1714-1724.

Baas PW, Black MM. 1990. Individual microtubules in the axon consist of domains that differ in both composition and stability. J Cell Biol 111(2):495-509.

Baas PW, Vidya Nadar C, Myers KA. 2006. Axonal transport of microtubules: the long and short of it. Traffic 7(5):490-8.

Ballard DH. 1981. Generalizing the Hough transform to detect arbitrary shapes. Pattern Recognition 13(2):111-122.

Banks P, Mayor D, Mitchell M, Tomlinson D. 1971a. Studies on the translocation of noradrenaline-containing vesicles in post-ganglionic sympathetic neurones in vitro. Inhibition of movement by colchicine and vinblastine and evidence for the involvement of axonal microtubules. The Journal of Physiology 216(3):625-639.

Banks P, Mayor D, Tomlinson DR. 1971b. Further evidence for the involvement of microtubules in the intra-axonal movement of noradrenaline storage granules. The Journal of Physiology 219(3):755-761.

Barash IA, Peters D, FridÃ©n J, Lutz GJ, Lieber RL. 2002. Desmin cytoskeletal modifications after a bout of eccentric exercise in the rat. American Journal of Physiology - Regulatory, Integrative and Comparative Physiology 283(4):R958-R963.

Barnea DI, Silverman HF. 1972. A Class of Algorithms for Fast Digital Image Registration. Computers, IEEE Transactions on C-21(2):179-186.

Barry DM, Millecamps S, Julien JP, Garcia ML. 2007. New movements in neurofilament transport, turnover and disease. Exp Cell Res 313(10):2110-20.

Bernal R, Pullarkat PA, Melo F. 2007. Mechanical properties of axons. Phys Rev Lett 99(1):018301.

Bilsland LG, Sahai E, Kelly G, Golding M, Greensmith L, Schiavo G. 2010. Deficits in axonal transport precede ALS symptoms in vivo. Proceedings of the National Academy of Sciences 107(47):20523-20528.

Black MM, Lasek RJ. 1979. Axonal transport of actin: Slow component b is the principal source of actin for the axon. Brain Research 171(3):401-413.

Black MM, Lasek RJ. 1980. Slow components of axonal transport: two cytoskeletal networks. The Journal of Cell Biology 86(2):616-623.

Bora FW, Jr., Richardson S, Black J. 1980. The biomechanical responses to tension in a peripheral nerve. J Hand Surg [Am] 5(1):21-5.

Brady ST, Lasek RJ, Allen RD. 1982. Fast axonal transport in extruded axoplasm from squid giant axon. Science 218(4577):1129-1131.

Bray D. 1973. BRANCHING PATTERNS OF INDIVIDUAL SYMPATHETIC NEURONS IN CULTURE. The Journal of Cell Biology 56(3):702-712.

Bray D. 1979. Mechanical tension produced by nerve cells in tissue culture. J Cell Sci 37:391-410.

Bray D. 1984. Axonal growth in response to experimentally applied mechanical tension. Dev Biol 102(2):379-89.

Bridgman PC. 2004. Myosin-dependent transport in neurons. J Neurobiol 58(2):164-74.

Bubb MR, Senderowicz AM, Sausville EA, Duncan KL, Korn ED. 1994. Jasplakinolide, a cytotoxic natural product, induces actin polymerization and competitively inhibits the binding of phalloidin to F-actin. Journal of Biological Chemistry 269(21):14869-14871.

Bubb MR, Spector I, Beyer BB, Fosen KM. 2000. Effects of Jasplakinolide on the Kinetics of Actin Polymerization. Journal of Biological Chemistry 275(7):5163-5170.

Bueno FR, Shah SB. 2008. Implications of tensile loading for the tissue engineering of nerves. Tissue Eng Part B Rev 14(3):219-33.

Burridge K, Fath K. 1989. Focal contacts: transmembrane links between the extracellular matrix and the cytoskeleton. Bioessays 10(4):104-8.

Burridge K, Molony L, Kelly T. 1987. Adhesion plaques: sites of transmembrane interaction between the extracellular matrix and the actin cytoskeleton. J Cell Sci Suppl 8:211-29.

Burton PR. 1987. Microtubules of frog olfactory axons: their length and number/axon. Brain Res 409(1):71-8.

Cameron LA, Yang G, Cimini D, Canman JC, Kisurina-Evgenieva O, Khodjakov A, Danuser G, Salmon ED. 2006. Kinesin 5â€“independent poleward flux of kinetochore microtubules in PtK1 cells. The Journal of Cell Biology 173(2):173-179.

Cavalli V, Kujala P, Klumperman J, Goldstein LS. 2005. Sunday Driver links axonal transport to damage signaling. J Cell Biol 168(5):775-87.

Chada S, Lamoureux P, Buxbaum RE, Heidemann SR. 1997. Cytomechanics of neurite outgrowth from chick brain neurons. J Cell Sci 110 (Pt 10):1179-86.

Chada SR, Hollenbeck PJ. 2003. Mitochondrial movement and positioning in axons: the role of growth factor signaling. J Exp Biol 206(Pt 12):1985-92.

Chada SR, Hollenbeck PJ. 2004. Nerve growth factor signaling regulates motility and docking of axonal mitochondria. Curr Biol 14(14):1272-6.

Chang C-M, Goldman RD. 1973. THE LOCALIZATION OF ACTIN-LIKE FIBERS IN CULTURED NEUROBLASTOMA CELLS AS REVEALED BY HEAVY MEROMYOSIN BINDING. The Journal of Cell Biology 57(3):867-874.

Chetta J, Kye C, Shah SB. 2009. Cytoskeletal dynamics in response to tensile loading of mammalian axons. Cytoskeleton 67(10):650-665.

Chetta J, Shah SB. 2011. A novel algorithm to generate kymographs from dynamic axons for the quantitative analysis of axonal transport. Journal of Neuroscience Methods 199(2):230-240.

Chevalier-Larsen E, Holzbaur EL. 2006. Axonal transport and neurodegenerative disease. Biochim Biophys Acta 1762(11-12):1094-108.

Chon K, Hwang HS, Lee JH, Song K. 2001. The myosin ATPase inhibitor 2,3-butanedione-2-monoxime disorganizes microtubules as well as F-actin in <i>Saccharomyces cerevisiae</i&gt. Cell Biology and Toxicology 17(6):383-393.

Cotman CW, Banker G, Churchill L, Taylor D. 1974. ISOLATION OF POSTSYNAPTIC DENSITIES FROM RAT BRAIN. The Journal of Cell Biology 63(2):441-455.

Coué M, Brenner SL, Spector I, Korn ED. 1987. Inhibition of actin polymerization by latrunculin A. FEBS Letters 213(2):316-318.

Cramer LP, Mitchison TJ. 1995. Myosin is involved in postmitotic cell spreading. The Journal of Cell Biology 131(1):179-189.

Cramer LP, Mitchison TJ. 1997. Investigation of the mechanism of retraction of the cell margin and rearward flow of nodules during mitotic cell rounding. Mol. Biol. Cell 8(1):109-119.

Dennerll TJ, Lamoureux P, Buxbaum RE, Heidemann SR. 1989. The cytomechanics of axonal elongation and retraction. J Cell Biol 109(6 Pt 1):3073-83.

Deumens R, Bozkurt A, Meek MF, Marcus MAE, Joosten EAJ, Weis J, Brook GA. 2010. Repairing injured peripheral nerves: Bridging the gap. Progress in Neurobiology 92(3):245-276.

Dove EL, Philip K, Gotteiner NL, Vonesh MJ, Rumberger JA, Reed JE, Stanford W, McPherson DD, Chandran KB. 1994. A Method for Automatic Edge Detection and Volume Computation of the Left Ventricle from Ultrafast Computed Tomographic Images. Investigative Radiology 29(11):945-954.

Droz B LC. 1963. Axonal Migration of Proteins in the central nervous system and peripheral nerves as shown by radioautography. J Comp Neurol Dec(121):325-46.

Duda RO, Hart PE. 1972. Use of the Hough transformation to detect lines and curves in pictures. Commun. ACM 15(1):11-15.

Duncan JE, Goldstein LS. 2006. The genetics of axonal transport and axonal transport disorders. PLoS Genet 2(9):e124.

Eggli S, Hankemayer S, MÃ¼ller ME. 1999. Nerve palsy after leg lengthening in total replacement arthroplasty for developmental dysplasia of the hip. J Bone Joint Surg Br 81(5):843-5.

Ekstrom P, Kanje M. 1984. Inhibition of fast axonal transport by erythro-9-[3-(2-hydroxynonyl)]adenine. J Neurochem 43(5):1342-5.

Flynn KC, Pak CW, Shaw AE, Bradke F, Bamburg JR. 2009. Growth cone-like waves transport actin and promote axonogenesis and neurite branching. Developmental Neurobiology 69(12):761-779.

Forer A, Fabian L. 2005. Does 2,3-butanedione monoxime inhibit nonmuscle myosin? Protoplasma 225(1):1-4.

Forman DS, Brown KJ, Promersberger ME. 1983. Selective inhibition of retrograde axonal transport byerythro-9-[3-(-2-hydroxynonyl)]adenine. Brain Research 272(1):194-197.

Frappier T, Stetzkowski-Marden F, Pradel LA. 1991. Interaction domains of neurofilament light chain and brain spectrin. Biochem J 275 (Pt 2):521-7.

Fujii T, Watanabe M, Ogoma Y, Kondo Y, Arai T. 1993. Microtubule-associated proteins, MAP 1A and MAP 1B, interact with F-actin in vitro. J Biochem 114(6):827-9.

Fung YC. 1993. Biomechanics: Mechanical Properties of Living Tissues. Fung YC, editor. New York: Springer-verlag.

Gallo G, Letourneau PC. 2000. Neurotrophins and the dynamic regulation of the neuronal cytoskeleton. J Neurobiol 44(2):159-73.

Gallo G, Yee HF, Jr., Letourneau PC. 2002. Actin turnover is required to prevent axon retraction driven by endogenous actomyosin contractility. J Cell Biol 158(7):1219-28.

Garcia ML, Lobsiger CS, Shah SB, Deerinck TJ, Crum J, Young D, Ward CM, Crawford TO, Gotow T, Uchiyama Y and others. 2003. NF-M is an essential target for the myelin-directed "outside-in" signaling cascade that mediates radial axonal growth. J Cell Biol 163(5):1011-20.

Gardel ML, Schneider IC, Aratyn-Schaus Y, Waterman CM. 2010. Mechanical Integration of Actin and Adhesion Dynamics in Cell Migration. Annual Review of Cell and Developmental Biology 26(1):315-333.

Gilchrist CL, Witvoet-Braam SW, Guilak F, Setton LA. 2007. Measurement of intracellular strain on deformable substrates with texture correlation. J Biomech 40(4):786-94.

Gittes F, Mickey B, Nettleton J, Howard J. 1993. Flexural rigidity of microtubules and actin filaments measured from thermal fluctuations in shape. The Journal of Cell Biology 120(4):923-934.

Goldstein LS, Yang Z. 2000. Microtubule-based transport systems in neurons: the roles of kinesins and dyneins. Annu Rev Neurosci 23:39-71.

Gunawardena S, Goldstein LSB. 2004. Cargo-carrying motor vehicles on the neuronal highway: Transport pathways and neurodegenerative disease. Journal of Neurobiology 58(2):258-271.

Haghnia M, Cavalli V, Shah SB, Schimmelpfeng K, Brusch R, Yang G, Herrera C, Pilling A, Goldstein LS. 2007. Dynactin is required for coordinated bidirectional motility, but not for dynein membrane attachment. Mol Biol Cell 18(6):2081-9.

Hao R, MacDonald RG, Ebadi M, Schmit JC, Pfeiffer RF. 1997. Stable interaction between G-actin and neurofilament light subunit in dopaminergic neurons. Neurochem Int 31(6):825-34.

Hasaka TP, Myers KA, Baas PW. 2004. Role of actin filaments in the axonal transport of microtubules. J Neurosci 24(50):11291-301.

He Y, Francis F, Myers KA, Yu W, Black MM, Baas PW. 2005. Role of cytoplasmic dynein in the axonal transport of microtubules and neurofilaments. J Cell Biol 168(5):697-703.

Heidemann SR, Joshi HC, Schechter A, Fletcher JR, Bothwell M. 1985. Synergistic effects of cyclic AMP and nerve growth factor on neurite outgrowth and microtubule stability of PC12 cells. J Cell Biol 100(3):916-27.

Heidemann SR, Lamoureux P, Buxbaum RE. 1995. Cytomechanics of axonal development. Cell Biochem Biophys 27(3):135-55.

Heidemann SR, Wirtz D. 2004. Towards a regional approach to cell mechanics. Trends in Cell Biology 14(4):160-166.

Hildebrand JD, Taylor JM, Parsons JT. 1996. An SH3 domain-containing GTPase-activating protein for Rho and Cdc42 associates with focal adhesion kinase. Mol Cell Biol 16(6):3169-78.

Hill DB, Plaza MJ, Bonin K, Holzwarth G. 2004. Fast vesicle transport in PC12 neurites: velocities and forces. Eur Biophys J 33(7):623-32.

Hirokawa N. 1982. Cross-linker system between neurofilaments, microtubules, and membranous organelles in frog axons revealed by the quick-freeze, deep-etching method. J Cell Biol 94(1):129-42.

Hirokawa N, Takemura R. 2004. Molecular motors in neuronal development, intracellular transport and diseases. Curr Opin Neurobiol 14(5):564-73.

Hoffman PN, Lasek RJ. 1975. The slow component of axonal transport. Identification of major structural polypeptides of the axon and their generality among mammalian neurons. J Cell Biol 66(2):351-66.

Hollenbeck. 1996. The pattern and mechanism of mitochondrial transport in axons. Fronteirs in bioscience: a journal and virtual library 1(1):d91-102

Hollenbeck PJ, Saxton WM. 2005. The axonal transport of mitochondria. J Cell Sci 118(Pt 23):5411-9.

Holzwarth G, Bonin K, Hill DB. 2002. Forces Required of Kinesin during Processive Transport through Cytoplasm. Biophysical Journal 82(4):1784-1790.

Ichimura H, Shiga T, Abe I, Hara Y, Terui N, Tsujino A, Ochiai N. 2005. Distribution of sodium channels during nerve elongation in rat peripheral nerve. J Orthop Sci 10(2):214-20.

Ikeda K, Tomita K, Tanaka S. 2000. Experimental study of peripheral nerve injury during gradual limb elongation. Hand Surg 5(1):41-7.

Illingworth J, Kittler J. 1988. A survey of the hough transform. Computer Vision, Graphics, and Image Processing 44(1):87-116.

Iwata A, Browne KD, Pfister BJ, Gruner JA, Smith DH. 2006. Long-term survival and outgrowth of mechanically engineered nervous tissue constructs implanted into spinal cord lesions. Tissue Eng 12(1):101-10.

Jou IM, Lai KA, Shen CL, Yamano Y. 2000. Changes in conduction, blood flow, histology, and neurological status following acute nerve-stretch injury induced by femoral lengthening. J Orthop Res 18(1):149-55.

Jung C, Chylinski TM, Pimenta A, Ortiz D, Shea TB. 2004. Neurofilament transport is dependent on actin and myosin. J Neurosci 24(43):9486-96.

Kang J-S, Tian J-H, Pan P-Y, Zald P, Li C, Deng C, Sheng Z-H. 2008. Docking of Axonal Mitochondria by Syntaphilin Controls Their Mobility and Affects Short-Term Facilitation. 132(1):137-148.

Kass M, Witkin A, Terzopoulos D. 1988. Snakes: Active contour models. International Journal of Computer Vision 1(4):321-331.

Katz MJ. 1985. How straight do axons grow? J. Neurosci. 5(3):589-595.

Ketschek A, Gallo G. 2010. Nerve Growth Factor Induces Axonal Filopodia through Localized Microdomains of Phosphoinositide 3-Kinase Activity That Drive the Formation of Cytoskeletal Precursors to Filopodia. The Journal of Neuroscience 30(36):12185-12197.

Koenig E, Koenig E. 2009. Organized Ribosome-Containing Structural Domains in Axons. Cell Biology of the Axon: Springer Berlin / Heidelberg. p 173-191.

Koenig E, Letourneau P. 2009. Actin in Axons: Stable Scaffolds and Dynamic Filaments. Cell Biology of the Axon: Springer Berlin / Heidelberg. p 65-90.

Koenig E, Martin R. 1996. Cortical plaque-like structures identify ribosome-containing domains in the Mauthner cell axon. The Journal of Neuroscience 16(4):1400-1411.

Koenig E, Martin R, Titmus M, Sotelo-Silveira JR. 2000. Cryptic Peripheral Ribosomal Domains Distributed Intermittently along Mammalian Myelinated Axons. The Journal of Neuroscience 20(22):8390-8400.

Kojima H, Ishijima A, Yanagida T. 1994. Direct measurement of stiffness of single actin filaments with and without tropomyosin by in vitro nanomanipulation. Proceedings of the National Academy of Sciences of the United States of America 91(26):12962-12966.

Kreplak L, Bar H, Leterrier JF, Herrmann H, Aebi U. 2005. Exploring the mechanical behavior of single intermediate filaments. J Mol Biol 354(3):569-77.

Lalli G, Gschmeissner S, Schiavo G. 2003. Myosin Va and microtubule-based motors are required for fast axonal retrograde transport of tetanus toxin in motor neurons. Journal of Cell Science 116(22):4639-4650.

Lambert de Rouvroit C, Goffinet AM. 2001. Neuronal migration. Mech Dev 105(1-2):47-56.

Lamoureux P, Ruthel G, Buxbaum RE, Heidemann SR. 2002. Mechanical tension can specify axonal fate in hippocampal neurons. J Cell Biol 159(3):499-508.

Lee C, Ma J, Deal DN, Smith BP, Koman LA, Smith TL, Shilt JS. 2006. Neuromuscular recovery after distraction osteogenesis at different frequencies in a rabbit model. J Pediatr Orthop 26(5):628-33.

Lee MK, Cleveland DW. 1996. Neuronal intermediate filaments. Annu Rev Neurosci 19:187-217.

Leterrier JF, Eyer J. 1987. Properties of highly viscous gels formed by neurofilaments in vitro. A possible consequence of a specific inter-filament cross-bridging. Biochem J 245(1):93-101.

Leterrier JF, KÃ¤s J, Hartwig J, Vegners R, Janmey PA. 1996. Mechanical Effects of Neurofilament Cross-bridges. Journal of Biological Chemistry 271(26):15687-15694.

Letourneau PC. 1975a. Cell-to-substratum adhesion and guidance of axonal elongation. Developmental Biology 44(1):92-101.

Letourneau PC. 1975b. Possible roles for cell-to-substratum adhesion in neuronal morphogenesis. Developmental Biology 44(1):77-91.

Letourneau PC. 1983. Differences in the organization of actin in the growth cones compared with the neurites of cultured neurons from chick embryos. The Journal of Cell Biology 97(4):963-973.

Leung CL, Sun D, Zheng M, Knowles DR, Liem RK. 1999. Microtubule actin cross-linking factor (MACF): a hybrid of dystonin and dystrophin that can interact with the actin and microtubule cytoskeletons. J Cell Biol 147(6):1275-86.

Li J, Shi R. 2006. A device for the electrophysiological recording of peripheral nerves in response to stretch. J Neurosci Methods 154(1-2):102-8.

Macioce P, Gandolfi N, Leung CL, Chin SS, Malchiodi-Albedi F, Ceccarini M, Petrucci TC, Liem RK. 1999. Characterization of NF-L and betaIISigma1-spectrin interaction in live cells. Exp Cell Res 250(1):142-54.

Mallik R, Carter BC, Lex SA, King SJ, Gross SP. 2004. Cytoplasmic dynein functions as a gear in response to load. Nature 427(6975):649-52.

McGrath JL, Tardy Y, Dewey Jr CF, Meister JJ, Hartwig JH. 1998. Simultaneous Measurements of Actin Filament Turnover, Filament Fraction, and Monomer Diffusion in Endothelial Cells. Biophysical Journal 75(4):2070-2078.

McQuarrie IG, Brady ST, Lasek RJ. 1986. Diversity in the axonal transport of structural proteins: major differences between optic and spinal axons in the rat. The Journal of Neuroscience 6(6):1593-1605.

Miller KE, Sheetz MP. 2004. Axonal mitochondrial transport and potential are correlated. J Cell Sci 117(Pt 13):2791-804.

Miller KE, Sheetz MP. 2006. Direct evidence for coherent low velocity axonal transport of mitochondria. J Cell Biol 173(3):373-81.

Mills RG, Minamide LS, Yuan A, Bamburg JR, Bray JJ. 1996. Slow Axonal Transport of Soluble Actin with Actin Depolymerizing Factor, Cofilin, and Profilin Suggests Actin Moves in an Unassembled Form. Journal of Neurochemistry 67(3):1225-1234.

Mondal S, Ahlawat S, Rau K, Venkataraman V, Koushika SP. 2011. Imaging in vivo neuronal transport in genetic model organisms using microfluidic devices. Traffic Apr;12(4):372-85.

Morris JR, Lasek RJ. 1982. Stable polymers of the axonal cytoskeleton: the axoplasmic ghost. The Journal of Cell Biology 92(1):192-198.

Morris JR, Lasek RJ. 1984. Monomer-polymer equilibria in the axon: direct measurement of tubulin and actin as polymer and monomer in axoplasm. The Journal of Cell Biology 98(6):2064-2076.

Morris RL, Hollenbeck PJ. 1995. Axonal transport of mitochondria along microtubules and F-actin in living vertebrate neurons. J Cell Biol 131(5):1315-26.

Motil J, Chan WK, Dubey M, Chaudhury P, Pimenta A, Chylinski TM, Ortiz DT, Shea TB. 2006. Dynein mediates retrograde neurofilament transport within axons and anterograde delivery of NFs from perikarya into axons: regulation by multiple phosphorylation events. Cell Motil Cytoskeleton 63(5):266-86.

Mukherjee A, Brian J, Cheng F, Richard JR, Gary B, Badrinath R. 2011. Automated Kymograph Analysis for Profiling Axonal Transport of Secretory Granules. Medical image analysis Jun;15(3):354-67.

Murray DW, Kambouroglou G, Kenwright J. 1993. One-stage lengthening for femoral shortening with associated deformity. J Bone Joint Surg Br 75(4):566-71.

Myers KA, Baas PW. 2007. Kinesin-5 regulates the growth of the axon by acting as a brake on its microtubule array. The Journal of Cell Biology 178(6):1081-1091.

Myers KA, Tint I, Nadar CV, He Y, Black MM, Baas PW. 2006. Antagonistic forces generated by cytoplasmic dynein and myosin-II during growth cone turning and axonal retraction. Traffic 7(10):1333-51.

Nadar VC, Ketschek A, Myers KA, Gallo G, Baas PW. 2008. Kinesin-5 Is Essential for Growth-Cone Turning. Current biology : CB 18(24):1972-1977.

Nagele RG, Kosciuk MC, Hunter ET, Bush KT, Lee H-y. 1988. Immunoelectron microscopic localization of actin in neurites of cultured embryonic chick dorsal root ganglia: actin is a component of granular, microtubule-associated crossbridges. Brain Research 474(2):279-286.

O'Brien RG. 1981. A simple test for variance effects in experimental designs. Psychological Bulletin 89(3):570-574.

O'Toole M, Lamoureux P, Miller KE. 2008. A physical model of axonal elongation: force, viscosity, and adhesions govern the mode of outgrowth. Biophys J 94(7):2610-20.

Okabe S, Hirokawa N. 1992. Differential behavior of photoactivated microtubules in growing axons of mouse and frog neurons. J Cell Biol 117(1):105-20.

Ostap E. 2002. 2,3-Butanedione monoxime (BDM) as a myosin inhibitor. Journal of Muscle Research and Cell Motility 23(4):305-308.

Penningroth SM, Cheung A, Bouchard P, Gagnon C, Bardin CW. 1982. Dynein ATPase is inhibited selectively in vitro by erythro-9-[3-2-(hydroxynonyl)]adenine. Biochemical and Biophysical Research Communications 104(1):234-240.

Peters A, Vaughn JE. 1967. Microtubules and filaments in the axons and astrocytes of early postnatal rat optic nerves. J Cell Biol 32(1):113-9.

Pfister BJ, Bonislawski DP, Smith DH, Cohen AS. 2006a. Stretch-grown axons retain the ability to transmit active electrical signals. FEBS Lett 580(14):3525-31.

Pfister BJ, Iwata A, Meaney DF, Smith DH. 2004. Extreme stretch growth of integrated axons. J Neurosci 24(36):7978-83.

Pfister BJ, Iwata A, Taylor AG, Wolf JA, Meaney DF, Smith DH. 2006b. Development of transplantable nervous tissue constructs comprised of stretch-grown axons. J Neurosci Methods 153(1):95-103.

Pfister KK. 1999. Cytoplasmic dynein and microtubule transport in the axon: the action connection. Molecular Neurobiology 20(2-3):81-91.

Philip KP, Dove EL, McPherson DD, Gotteiner NL, Stanford W, Chandran KB. 1994. The fuzzy Hough transform-feature extraction in medical images. Medical Imaging, IEEE Transactions on 13(2):235-240.

Qu L, Peng H. 2010. A principal skeleton algorithm for standardizing confocal images of fruit fly nervous systems. Bioinformatics 26(8):1091-1097.

Rammensee S, Janmey PA, Bausch AR. 2007. Mechanical and structural properties of in vitro neurofilament hydrogels. Eur Biophys J 36(6):661-8.

Rao MV, Engle LJ, Mohan PS, Yuan A, Qiu D, Cataldo A, Hassinger L, Jacobsen S, Lee VM, Andreadis A and others. 2002. Myosin Va binding to neurofilaments is essential for correct myosin Va distribution and transport and neurofilament density. J Cell Biol 159(2):279-90.

Ridley AJ, Hall A. 1992. The small GTP-binding protein rho regulates the assembly of focal adhesions and actin stress fibers in response to growth factors. Cell 70(3):389-99.

Riedl J, Crevenna AH, Kessenbrock K, Yu JH, Neukirchen D, Bista M, Bradke F, Jenne D, Holak TA, Werb Z and others. 2008. Lifeact: a versatile marker to visualize F-actin. Nat Meth 5(7):605-607.

Rodionov VI, Hope AJ, Svitkina TM, Borisy GG. 1998. Functional coordination of microtubule-based and actin-based motility in melanophores. Current biology : CB 8(3):165-169.

Roger B, Al-Bassam J, Dehmelt L, Milligan RA, Halpain S. 2004. MAP2c, but Not Tau, Binds and Bundles F-Actin via Its Microtubule Binding Domain. Current biology : CB 14(5):363-371.

Rothenberg ME, Rogers SL, Vale RD, Jan LY, Jan Y-N. 2003. Drosophila Pod-1 Crosslinks Both Actin and Microtubules and Controls the Targeting of Axons. Neuron 39(5):779-791.

Roy S, Coffee P, Smith G, Liem RKH, Brady ST, Black MM. 2000. Neurofilaments Are Transported Rapidly But Intermittently in Axons: Implications for Slow Axonal Transport. J. Neurosci. 20(18):6849-6861.

Roy S, Winton MJ, Black MM, Trojanowski JQ, Lee VMY. 2007. Rapid and Intermittent Cotransport of Slow Component-b Proteins. J. Neurosci. 27(12):3131-3138.

Roy S, Winton MJ, Black MM, Trojanowski JQ, Lee VMY. 2008. Cytoskeletal Requirements in Axonal Transport of Slow Component-b. J. Neurosci. 28(20):5248-5256.

Ruthel G, Banker G. 1998. Actin-dependent anterograde movement of growth-cone-like structures along growing hippocampal axons: A novel form of axonal transport? Cell Motility and the Cytoskeleton 40(2):160-173.

Ruthel G, Banker G. 1999. Role of moving growth cone–like “wave” structures in the outgrowth of cultured hippocampal axons and dendrites. Journal of Neurobiology 39(1):97-106.

Ruthel G, Hollenbeck PJ. 2003. Response of mitochondrial traffic to axon determination and differential branch growth. J Neurosci 23(24):8618-24.

Sakama R, Hiruma H, Kawakami T. 2003. Effects of extracellular atp on axonal transport in cultured mouse dorsal root ganglion neurons. Neuroscience 121(3):531-535.

Sanchez-Soriano N, Travis M, Dajas-Bailador F, GonÃ§alves-Pimentel C, Whitmarsh AJ, Prokop A. 2009. Mouse ACF7 and Drosophila Short stop modulate filopodia formation and microtubule organisation during neuronal growth. Journal of Cell Science 122(14):2534-2542.

Sankaranarayanan S, Atluri PP, Ryan TA. 2003. Actin has a molecular scaffolding, not propulsive, role in presynaptic function. Nat Neurosci 6(2):127-135.

Schliwa M, Ezzell RM, Euteneuer U. 1984. erythro-9-[3-(2-Hydroxynonyl)]adenine is an effective inhibitor of cell motility and actin assembly. Proceedings of the National Academy of Sciences 81(19):6044-6048.

Schmidt CE, Leach JB. 2003. NEURAL TISSUE ENGINEERING: Strategies for Repair and Regeneration. Annual Review of Biomedical Engineering 5(1):293-347.

Schnapp BJ, Reese TS. 1989. Dynein is the motor for retrograde axonal transport of organelles. Proc Natl Acad Sci U S A 86(5):1548-52.

Scott David A, Das U, Tang Y, Roy S. 2011. Mechanistic Logic Underlying the Axonal Transport of Cytosolic Proteins. Neuron 70(3):441-454.

Semenova I, Burakov A, Berardone N, Zaliapin I, Slepchenko B, Svitkina T, Kashina A, Rodionov V. 2008. Actin Dynamics Is Essential for Myosin-Based Transport of Membrane Organelles. Current biology : CB 18(20):1581-1586.

Shah SB, Nolan R, Davis E, Stokin GB, Niesman I, Canto I, Glabe C, Goldstein LS. 2009. Examination of potential mechanisms of amyloid-induced defects in neuronal transport. Neurobiol Dis. *(in press doi:10.1016/j.nbd.2009.05.016)*.

Shah SB, Su F-C, Jordan K, Milner DJ, FridÃ©n J, Capetanaki Y, Lieber RL. 2002. Evidence for increased myofibrillar mobility in desmin-null mouse skeletal muscle. Journal of Experimental Biology 205(3):321-325.

Shapiro SD. 1978. Properties of transforms for the detection of curves in noisy pictures. Computer Graphics and Image Processing 8(2):219-236.

Shea TB. 2000. Microtubule motors, phosphorylation and axonal transport of neurofilaments. J Neurocytol 29(11-12):873-87.

Shi R, Pryor JD. 2002. Pathological changes of isolated spinal cord axons in response to mechanical stretch. Neuroscience 110(4):765-77.

Shi R, Whitebone J. 2006. Conduction deficits and membrane disruption of spinal cord axons as a function of magnitude and rate of strain. J Neurophysiol 95(6):3384-90.

Shibukawa M, Shirai Y. 2001. Experimental study on slow-speed elongation injury of the peripheral nerve: electrophysiological and histological changes. J Orthop Sci 6(3):262-8.

Smith DH, Wolf JA, Meaney DF. 2001. A new strategy to produce sustained growth of central nervous system axons: continuous mechanical tension. Tissue Eng 7(2):131-9.

Smith EL, Gilligan C. 1996. Dose-response relationship between physical loading and mechanical competence of bone. Bone 18(1 Suppl):455-505.

Spiegel DA, Seaber AV, Chen LE, Urbaniak JR. 1993. Recovery following stretch injury to the sciatic nerve of the rat: an in vivo study. J Reconstr Microsurg 9(1):69-74.

Spillane M, Ketschek A, Jones SL, Korobova F, Marsick B, Lanier L, Svitkina T, Gallo G. 2011. The actin nucleating Arp2/3 complex contributes to the formation of axonal filopodia and branches through the regulation of actin patch precursors to filopodia. Developmental Neurobiology:n/a-n/a.

Takeda S, Okabe S, Funakoshi T, Hirokawa N. 1994. Differential dynamics of neurofilament-H protein and neurofilament-L protein in neurons. The Journal of Cell Biology 127(1):173-185.

Takeuchi H, Mizuno T, Zhang G, Wang J, Kawanokuchi J, Kuno R, Suzumura A. 2005. Neuritic beading induced by activated microglia is an early feature of neuronal dysfunction toward neuronal death by inhibition of mitochondrial respiration and axonal transport. J Biol Chem 280(11):10444-54.

Tashiro T, Komiya Y. 1989. Stable and dynamic forms of cytoskeletal proteins in slow axonal transport. J. Neurosci. 9(3):760-768.

Tint I, Jean D, Baas PW, Black MM. 2009. Doublecortin Associates with Microtubules Preferentially in Regions of the Axon Displaying Actin-Rich Protrusive Structures. The Journal of Neuroscience 29(35):10995-11010.

Topp KS, Boyd BS. 2006. Structure and biomechanics of peripheral nerves: nerve responses to physical stresses and implications for physical therapist practice. Phys Ther 86(1):92-109.

Tsukada M, Prokscha A, Ungewickell E, Eichele G. 2005. Doublecortin Association with Actin Filaments Is Regulated by Neurabin II. Journal of Biological Chemistry 280(12):11361-11368.

Unsicker K DD, Gröschel-Stewart U, Schumacher U, Griesser GH. 1978. Immunohistochemical evidence of myosin in peripheral nerves and spinal cord of the rat. Neuroscience 3(3):301-6.

Vale RD, Reese TS, Sheetz MP. 1985a. Identification of a novel force-generating protein, kinesin, involved in microtubule-based motility. Cell 42(1):39-50.

Vale RD, Schnapp BJ, Mitchison T, Steuer E, Reese TS, Sheetz MP. 1985b. Different axoplasmic proteins generate movement in opposite directions along microtubules in vitro. Cell 43(3, Part 2):623-632.

Vallee RB, Bloom GS. 1991. Mechanisms of fast and slow axonal transport. Annu Rev Neurosci 14:59-92.

Vandenburgh HH, Hatfaludy S, Karlisch P, Shansky J. 1991. Mechanically induced alterations in cultured skeletal muscle growth. J Biomech 24 Suppl 1:91-9.

Venier P, Maggs AC, Carlier MF, Pantaloni D. 1994. Analysis of microtubule rigidity using hydrodynamic flow and thermal fluctuations. Journal of Biological Chemistry 269(18):13353-13360.

Wagner OI, Lifshitz J, Janmey PA, Linden M, McIntosh TK, Leterrier JF. 2003. Mechanisms of Mitochondria-Neurofilament Interactions. J. Neurosci. 23(27):9046-9058.

Wall EJ, Kwan MK, Rydevik BL, Woo SL, Garfin SR. 1991. Stress relaxation of a peripheral nerve. J Hand Surg [Am] 16(5):859-63.

Wall EJ, Massie JB, Kwan MK, Rydevik BL, Myers RR, Garfin SR. 1992. Experimental stretch neuropathy. Changes in nerve conduction under tension. J Bone Joint Surg Br 74(1):126-9.

Walsh TP, Tellam RL. 1986. Erythro-9-[3-(2-hydroxynonyl)]adenine accelerates actin polymerization and nucleotide exchange. Biochemical and Biophysical Research Communications 137(3):1181-1186.

Wang L, Brown A. 2001. Rapid intermittent movement of axonal neurofilaments observed by fluorescence photobleaching. Mol Biol Cell 12(10):3257-67.

Wang L, Brown A. 2002. Rapid movement of microtubules in axons. Curr Biol 12(17):1496-1501.

Wang L, Ho C-l, Sun D, Liem RKH, Brown A. 2000. Rapid movement of axonal neurofilaments interrupted by prolonged pauses. Nat Cell Biol 2(3):137-141.

Waterman-Storer CM, Karki SB, Kuznetsov SA, Tabb JS, Weiss DG, Langford GM, Holzbaur ELF. 1997. The interaction between cytoplasmic dynein and dynactin is required for fast axonalâ€‰transport. Proceedings of the National Academy of Sciences of the United States of America 94(22):12180-12185.

Weiss P, Hiscoe HB. 1948. Experiments on the Mechanism of Nerve Growth. The Journal of Experimental Zoology 107(3):315-395.

Welzel O, Boening D, Stroebel A, Reulbach U, Klingauf J, Kornhuber J, Groemer T. 2009. Determination of axonal transport velocities via image cross- and autocorrelation. European Biophysics Journal 38(7):883-889.

Willard M, Cowan WM, Vagelos PR. 1974. The Polypeptide Composition of Intra-axonally Transported Proteins: Evidence for Four Transport Velocities. Proceedings of the National Academy of Sciences 71(6):2183-2187.

Xin L, Imielinska C, Laine AF, D'Ambrosio A. Symmetry Based Multi-modality Registration of the Brain Imagery; 2007 15-18 Dec. 2007. p 807-812.

Yabe JT, Pimenta A, Shea TB. 1999. Kinesin-mediated transport of neurofilament protein oligomers in growing axons. Journal of Cell Science 112(21):3799-3814.

Yamada KM, Spooner BS, Wessells NK. 1971. Ultrastructure and function of growth cones and axons of cultured nerve cells. J Cell Biol 49(3):614-35.

Yarrow J, Lechler T, Li R, Mitchison T. 2003. Rapid de-localization of actin leading edge components with BDM treatment. BMC Cell Biology 4(1):5.

Ying-Lun F, Chan JCK, Chin RT. 1996. Automated analysis of nerve-cell images using active contour models. Medical Imaging, IEEE Transactions on 15(3):353-368.

Yokota A, Doi M, Ohtsuka H, Abe M. 2003. Nerve conduction and microanatomy in the rabbit sciatic nerve after gradual limb lengthening-distraction neurogenesis. J Orthop Res 21(1):36-43.

Yu W, Ahmad FJ, Baas PW. 1994. Microtubule fragmentation and partitioning in the axon during collateral branch formation. J Neurosci 14(10):5872-84.

Yu W, Baas PW. 1994. Changes in microtubule number and length during axon differentiation. J Neurosci 14(5 Pt 1):2818-29.

Zeiger AS, Layton BE. 2008. Molecular Modeling of the Axial and Circumferential Elastic Moduli of Tubulin. 95(8):3606-3618.

Zhang K, Osakada Y, Xie W, Cui B. 2010. Automated image analysis for tracking cargo transport in axons. Microscopy Research and Technique Article first published online: 13 OCT 2010

DOI: 10.1002/jemt.20934:n/a-n/a.

Zheng J, Lamoureux P, Santiago V, Dennerll T, Buxbaum RE, Heidemann SR. 1991. Tensile regulation of axonal elongation and initiation. J Neurosci 11(4):1117-25.

Zhou HM, Brust-Mascher I, Scholey JM. 2001. Direct Visualization of the Movement of the Monomeric Axonal Transport Motor UNC-104 along Neuronal Processes in Living Caenorhabditis elegans. J. Neurosci. 21(11):3749-3755.

Zitová B, Flusser J. 2003. Image registration methods: a survey. Image and Vision Computing 21(11):977-1000.